REPORT DOCUMENTATION PAGE

| 1. AGENCY USE ONLY (Leave blank)	2. REPORT DATE	3. REPORT TYPE AND DATES COVERED
		FINAL/01 NOV 92 TO 31 JAN 95

4. TITLE AND SUBTITLE

APPLIED NUMERICAL METHODS WITH COIFMAN-MEYER BASES

5. FUNDING NUMBERS

2304/BS
F49620-92-J-0029

6. AUTHOR(S)

EYTAN BAROUCH

AFOSR-TR-95

C488

7. PERFORMING ORGANIZATION NAME(S) AND ADDRESS(ES)

CLARKSON UNIVERSITY
145A CLARKSON HALL
POTSDAM NY 13676

9. SPONSORING/MONITORING AGENCY NAME(S) AND ADDRESS(ES)

AFOSR/NM
110 DUNCAN AVE, SUTE B115
BOLLING AFB DC 20332-0001

DTIC
ELECTE
JUL 28 1995
B

10. SPONSORING/MONITORING AGENCY REPORT NUMBER

F49620-92-J-0029
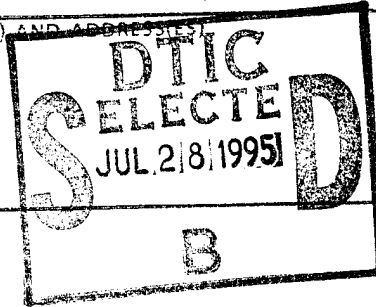
11. SUPPLEMENTARY NOTES

12a. DISTRIBUTION/AVAILABILITY STATEMENT

APPROVED FOR PUBLIC RELEASE: DISTRIBUTION IS UNLIMITED

12b. DISTRIBUTION CODE

13. ABSTRACT (Maximum 200 words)

The main mathematical ideas behind this project was to implement Ciofman-Meyer type bases in various numerical algorithms. In Particular, when large grid FFT are concerned, the refining of grids near discontinuity is impractical and lead to very expensive CPU overhead. The CF bases allow the imposition of the "bells" such that the discontinuous domains can be "stitched" together.
In microprocess simulations it is critical and discontinuities appear naturally. The finite numerical apperture of the optical systems presents a discontinuity in k-space, and the implementation of the bells with the CF bases provided the necessary mathematical mechanism for the algorithms construction.

DTIC QUALITY INSPECTED 5

19950727 025

15. NUMBER OF PAGES

16. PRICE CODE

17. SECURITY CLASSIFICATION	18. SECURITY CLASSIFICATION	19. SECURITY CLASSIFICATION	20. LIMITATION OF ABSTRACT
UNCLASSIFIED	UNCLASSIFIED	UNCLASSIFIED	SAR(SAME AS REPORT)

Final Report on Air Force Contract "Coifman-Meyer Bases....."

PM: Dr. Arje Nachman, AFOSR
PI: Eytan Barouch, Clarkson University

O. GENERAL
       The main mathematical idea behind this project was to implement Ciofman-Meyer type bases in various numerical algorithms. In particular, when large grid FFT are concerned, the refining of grids near discontinuity is impractical and leads to very expensive CPU overhead. The CF bases allow the imposition of the "bells" such that the discontinuous domains can be "stitched" together.
In microprocess simulations it is critical and discontinuities appear naturally. The finite numerical apperture of the optical systems presents a discontinuity in k-space, and the implementation of the bells with the CF bases provided the necessary mathematical mechanism for the algorithms construction.

I. INTRODUCTION

       This is a summary of our research and development effort in the simulation of microprocesses, based on precise numerical algorithms and their implementation, employment of state of the art numerical methods, physical and material-science principles for the underlying models and their corresponding partial differential equations, and driven by strong interaction with concerns of key companies and the need for simulation and technology transfer.
       The general theme of our effort finds its genesis in specific problems encountered by the IC industry. In particular, we refer to HP, IBM, AMD and SEMATECH. Once a specific problem is identified, its scientific origin is investigated, its mechanism determined and formulated, and it is treated in as much generality as possible. The numerical algortihms and coding of the generic problems are developed and applied to the specific problems at hand, transfered to the R&D groups that generated the problems for testing and evaluation, then refined, optimized and improved as needed.
       The ultimate goal is always driven towards experimental verification by industrial and government labs, as applied, in particular, to the manufacturing processes. A robust simulation package is built, and modified as requested by industry.

II. EXAMPLES OF ACHIEVMENTS

In this section, we illustrate some of our ongoing efforts with several industrial research groups, who are using our work in solving their problems and helping in narrowing their process windows.

A. IBM

In the developing technologies of 64 and 256 Mb memory chips, the limiting factor is the resolution at the gate level. Since IBM's process involves their own deep UV resist (APEX-E), the SRAM feature sizes of 0.25 micron, 0.3 micron and 0.35 micron need to be optimized using the projection optics on the resist, the complicated and unique post-exposure bake process and its dissolution. A multitude of conditions need to be optimized, like exposure latitude, focus latitude, bake temperature and duration, dissolution and solvent properties, concentraions, etc. IBM (D. Cole), using our fast aerial image model (FAIM) requested adaptation of FAIM to their threshold model. It was expected to serve as a guide to evatuate SRAM structures at the gate level, at best focus. Due to the very low acid production and extremely high sensitivity of the resist at hand, the agreement between optimized simulation and actual SRAM measurements was very good, to +/- 1 micron defocus. We received and transmitted to AFOSR a letter of recongnition of of our effort from IBM.

B. AMD

In i-line technology of flash EPROM manufacturing, the thickness of the Nitride layer varies between 0.1 micron and 0.25 micron. Previous g-line technology has established, through a proglonged trial and error process, optimal Nitride thickness layers, for 0.75 micron to 1 micron feature sizes. However, the dependece of the final feature size on the Nitride thickness varies drasticaly with i-line, and a new optimiztion process needed to be launched. At AMD's (W. Arnold and B. Singh's) request we have developed the software to address this issue, and transfered this technology to AMD. These results are now being used in strategic planning of the flash EPROM process development by AMD. The "swing curve" of the Nitride process for 0.5 microm lines and spaces is given in fi. 2 with a letter of support from was obtained from AMD and transmitted to AFOSR.

C. HP

In the process of inkject printer manufacturing, one wishes to project circular images (or as close to circularity as possible) on the inkjet pen. The projected laser beam interacts with the organic material, boring a hole in the projected shape.

The image is generated from a square grid of a phase shifted mask (or a checkerboard chrome mask) in order to create 25-40 micron projected circular images.

A set of crucial issues arise: (i) What polygonal shape on the mask will best project a circular image through 200 micron defocus range? (ii) Where, on the grid, should the said polygon be placed? (iii) Which external parameters are most important to control to achieve uniformity?

At HP's request, we have modified FAIM to accomodate this problem in part.

D. SEMATECH

Until recently, comparison of simulation and experiments was very difficult. The main reason for that lies in the complexity of the sequential processes that lead to the printed micrographs. In other words, intermediate states were impossible to measure, and one did not know for certain which process needs refinement. That has been changed with the invention of the IBM AIMS tool. It is designed to measure the projected light intensity on the wafers. It was a very natural project to pursue, and to evrybody's delight, our software FAIM and the AIMS tool were within 1-3% (ratio of 0.97) agreement. A few weeks later, a second set of measurements showed sharp disagreements (ratio of 0.35). The users' confidence in FAIM led to the unusual suggestion that the AIMS tool was malfunctioning. A detailed analysis, outlined in the official letter from SEMATECH (J. Nistler) explains the details involved in the repair of the tool. The agreement of measurement and simulation (of 0.97-0.98 ratio) has been restored! We consider it a great triumph of our simulation efforts.
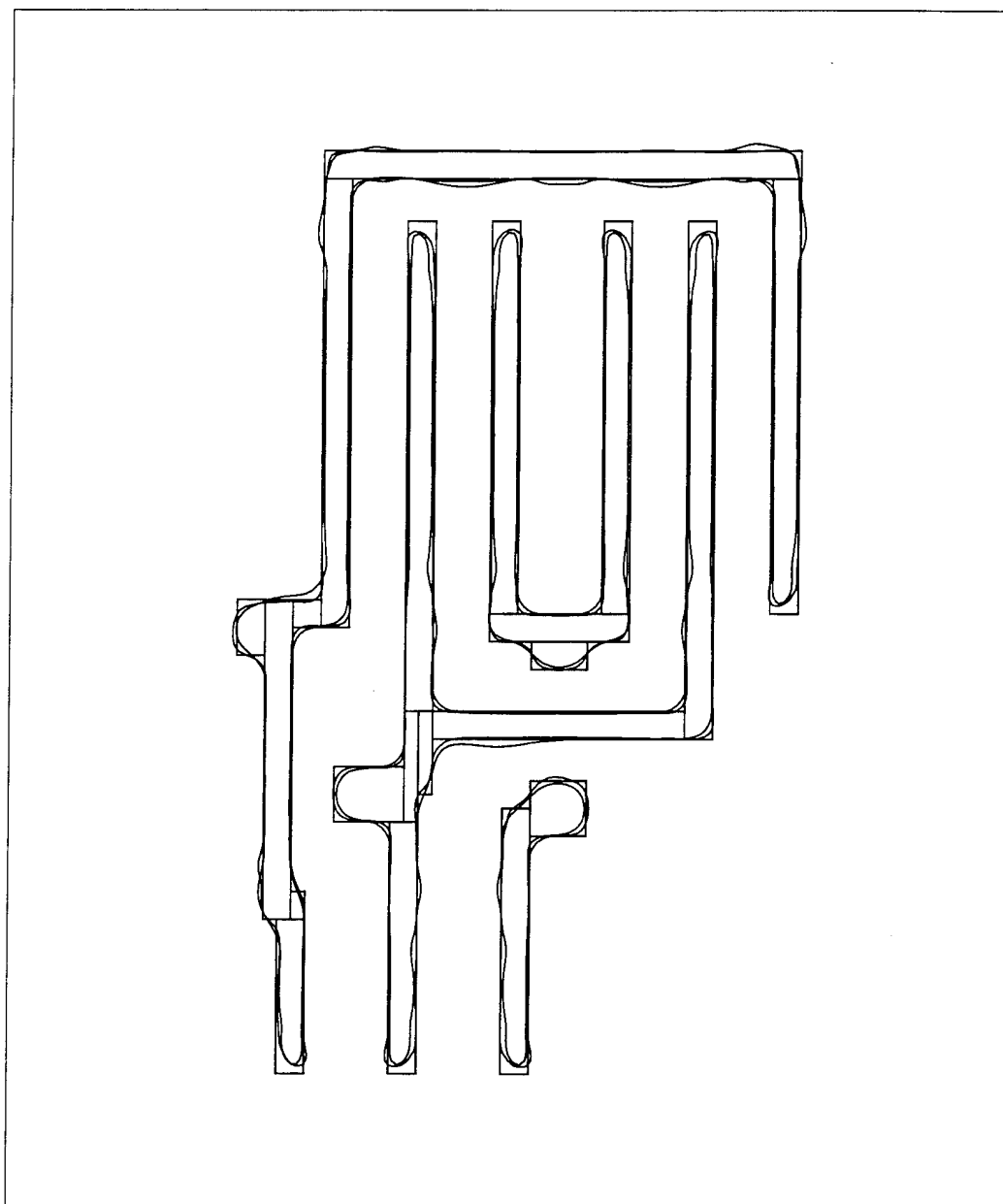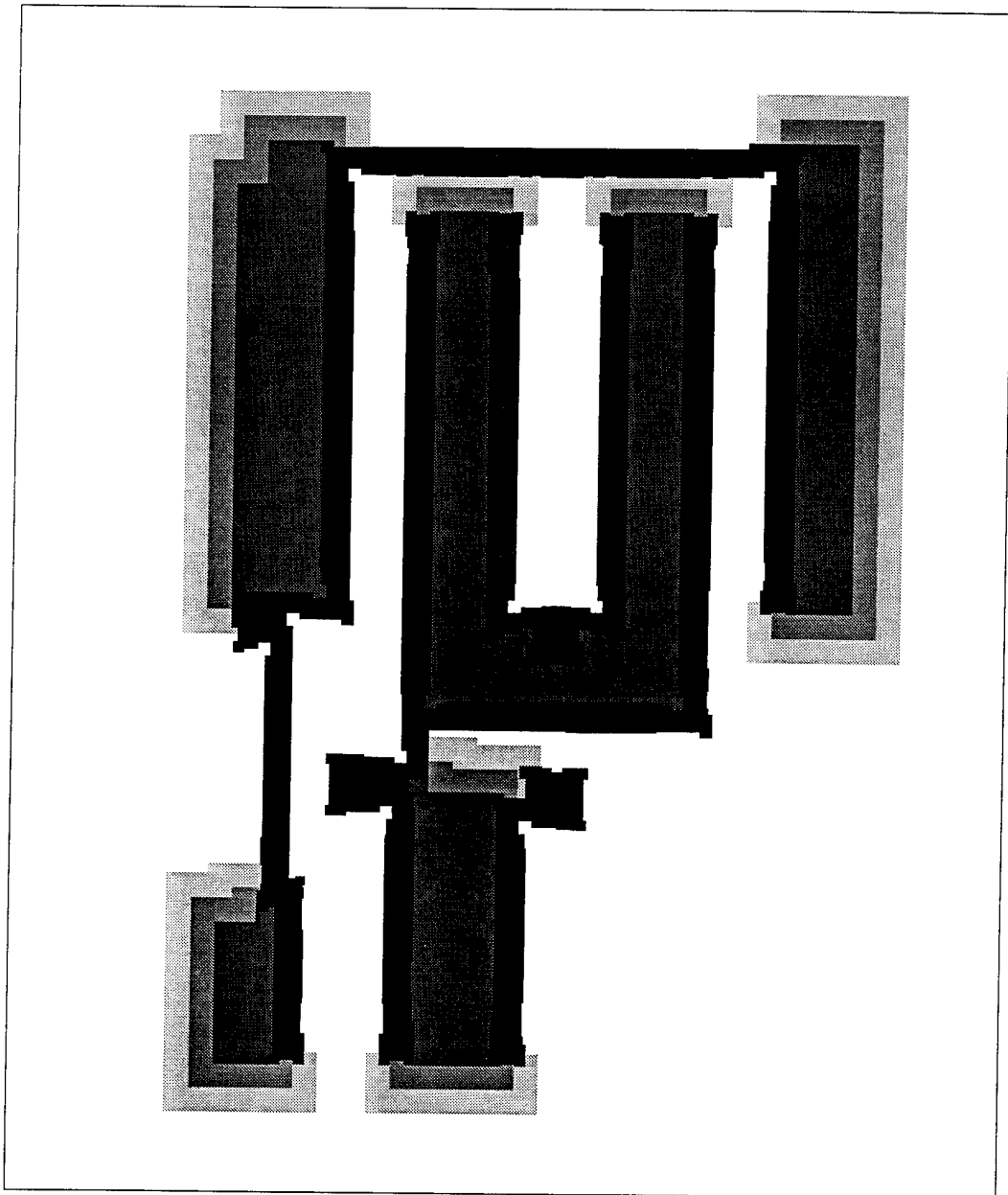
III Papers

Several papers are attached.
Most of the papers in this project have been sent to AFOSR previously
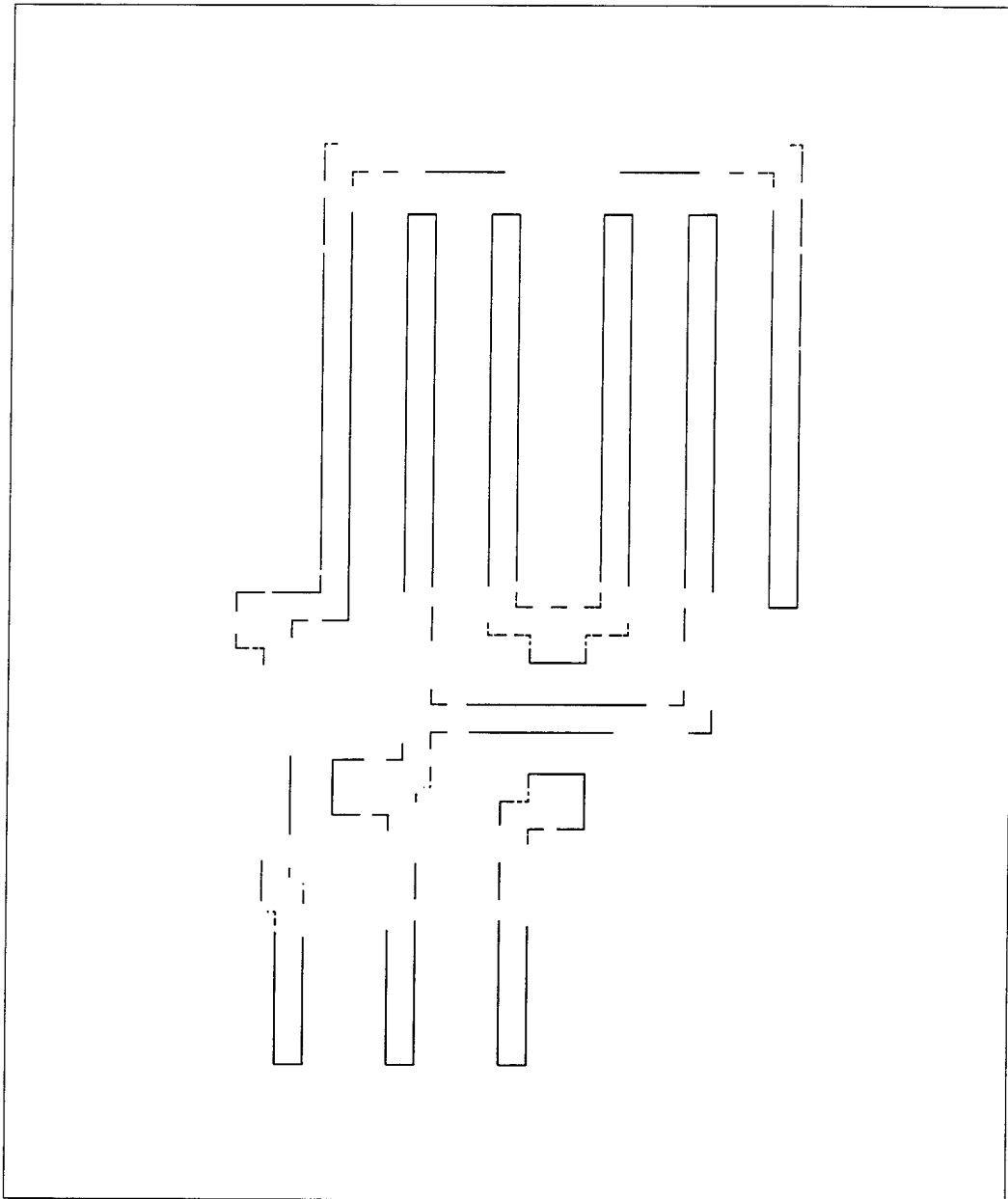
alt. phase shift 0.4 fea. 0.8 def. mod. image and orig. image in orig. mask

alt. phase shift 0.4 fea. mod. mask
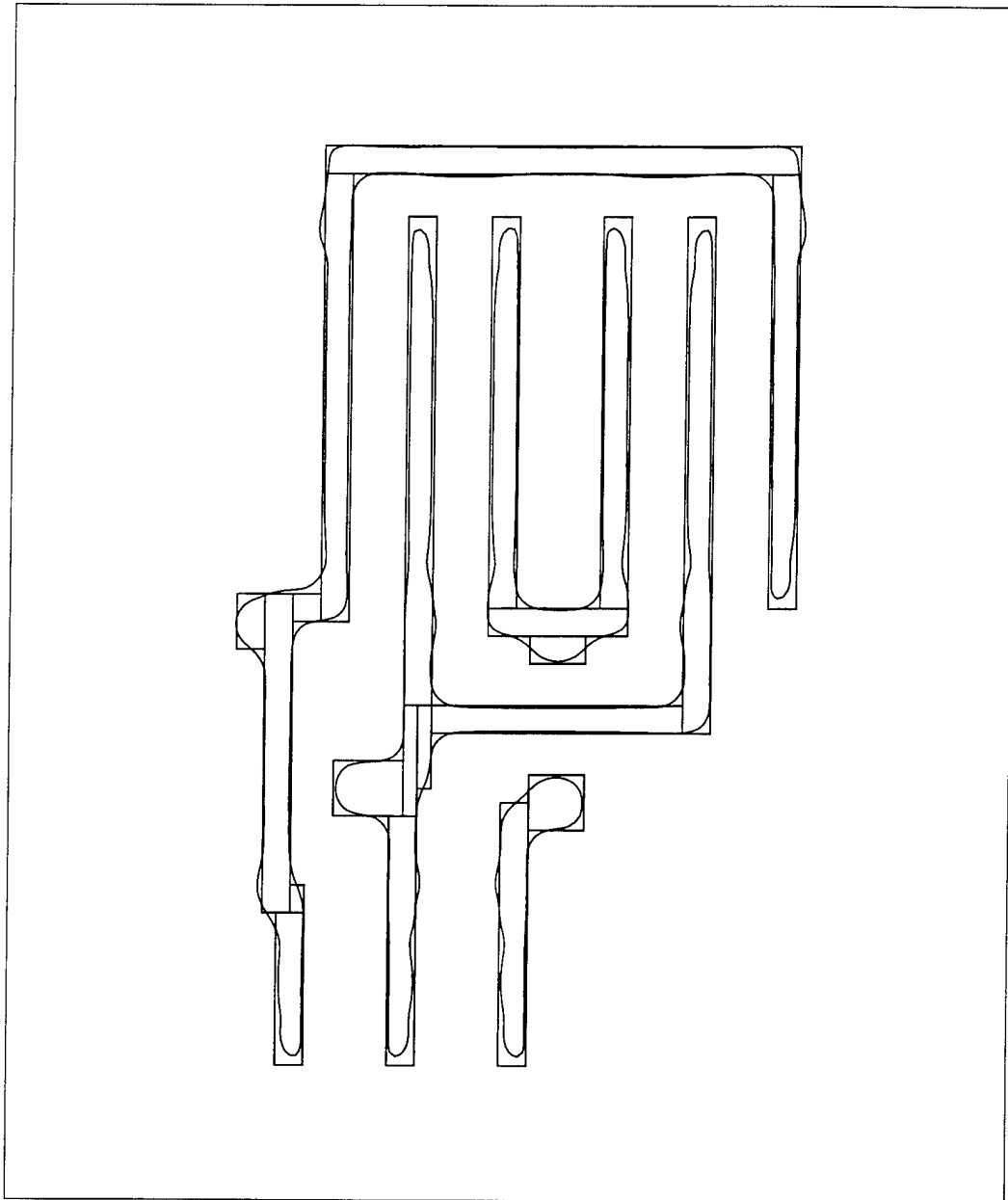
Failures alt. phase shift 0.4 fea. 0.8 def.

alt. phase shift 0.4 fea. 0.8 def. orig. image in orig. mask

alt. phase shift 0.4 fea. 0.8 def. mod. image in orig. mask
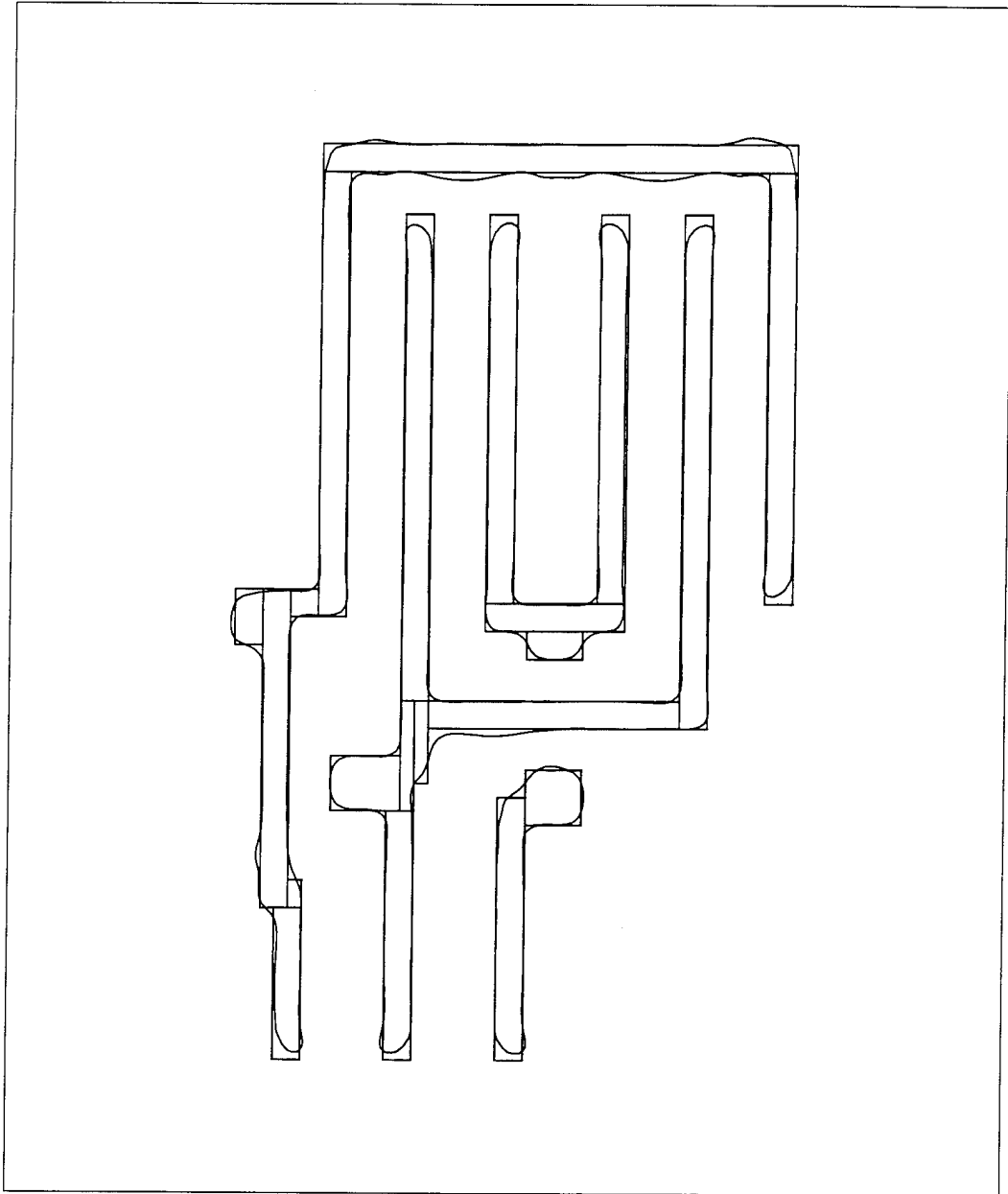
nikon 0.35 fea. 0.4 def. mod. & orig. images in orig. mask
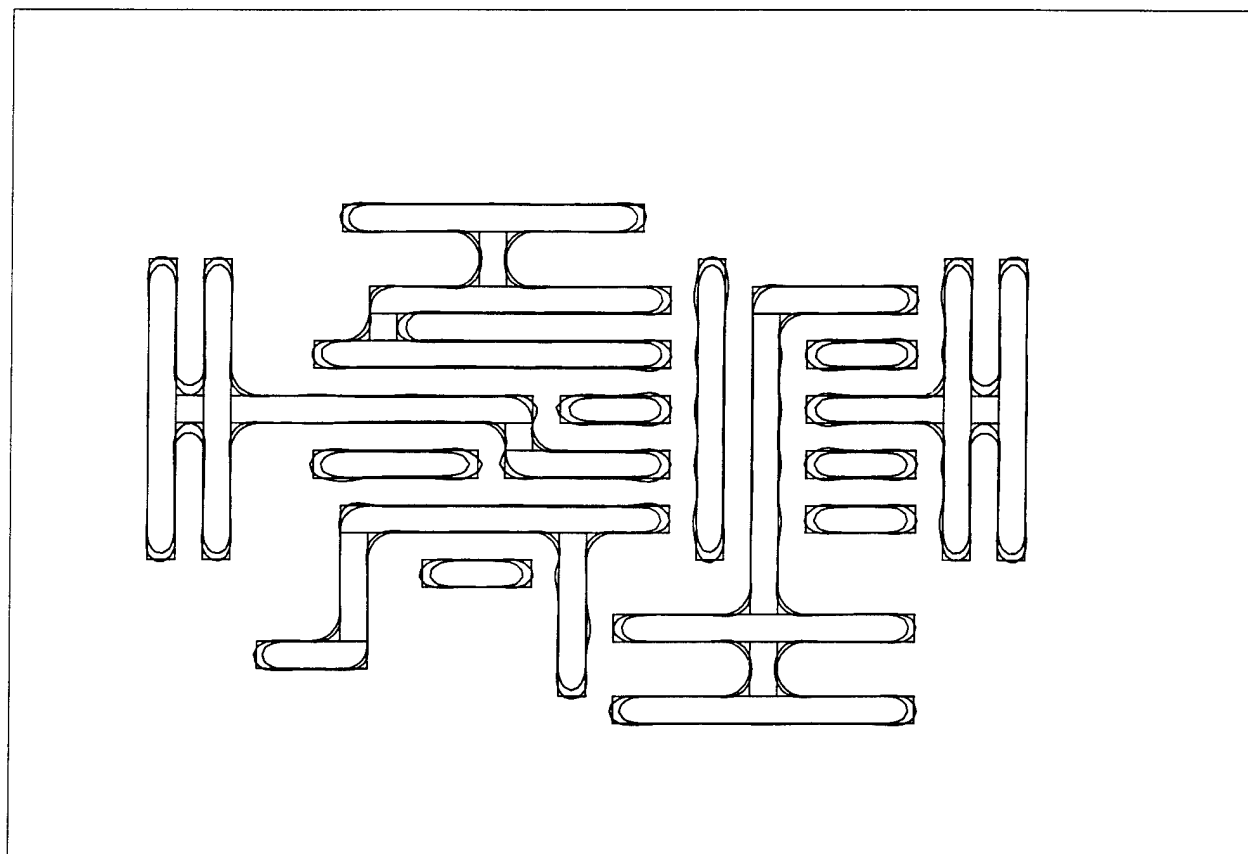
nikon 0.35 fea. 0.4 def. mod. image in orig. mask

nikon 0.35 fea. mod. mask

nikon 0.35 fea. 0.4 def. orig. image in orig. mask

Failures nikon 0.35 fea. 0.4 def.

Reprinted from

Advances in Resist Technology and Processing X

1–2 March 1993
San Jose, California

SPIE
P
PROCEEDINGS
SERIES

Volume 1925

Characterization and simulation of acid catalyzed DUV positive photoresist

Nicholas K. Eib
IBM Semiconductor Research & Development Center
East Fishkill Facility
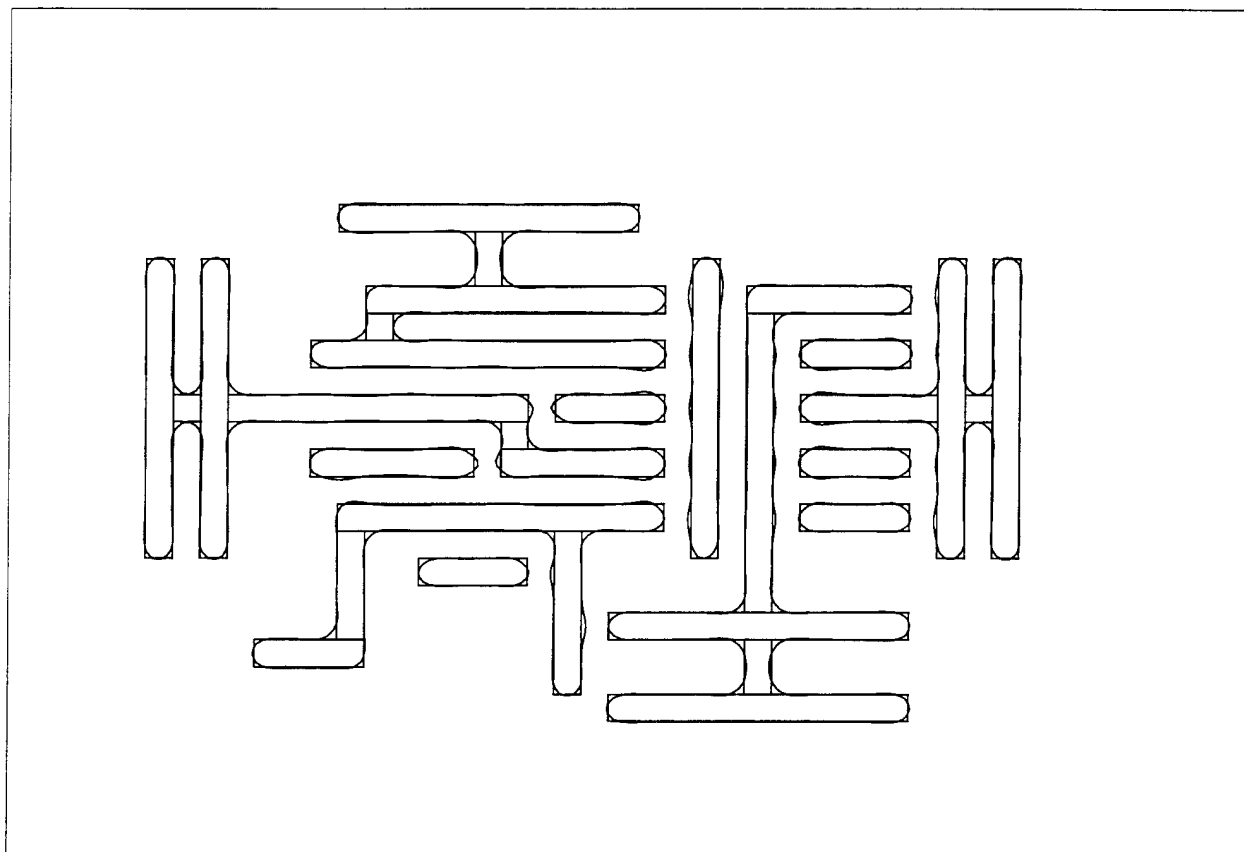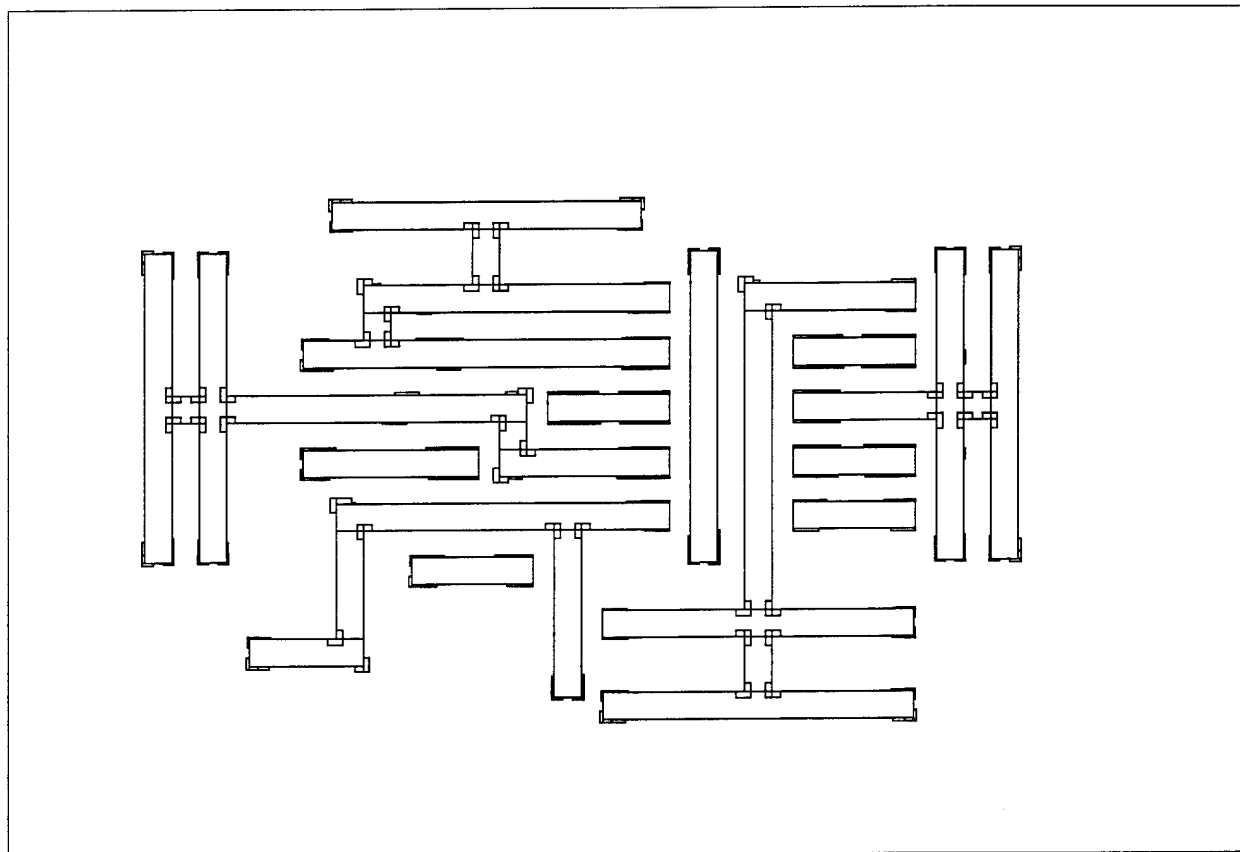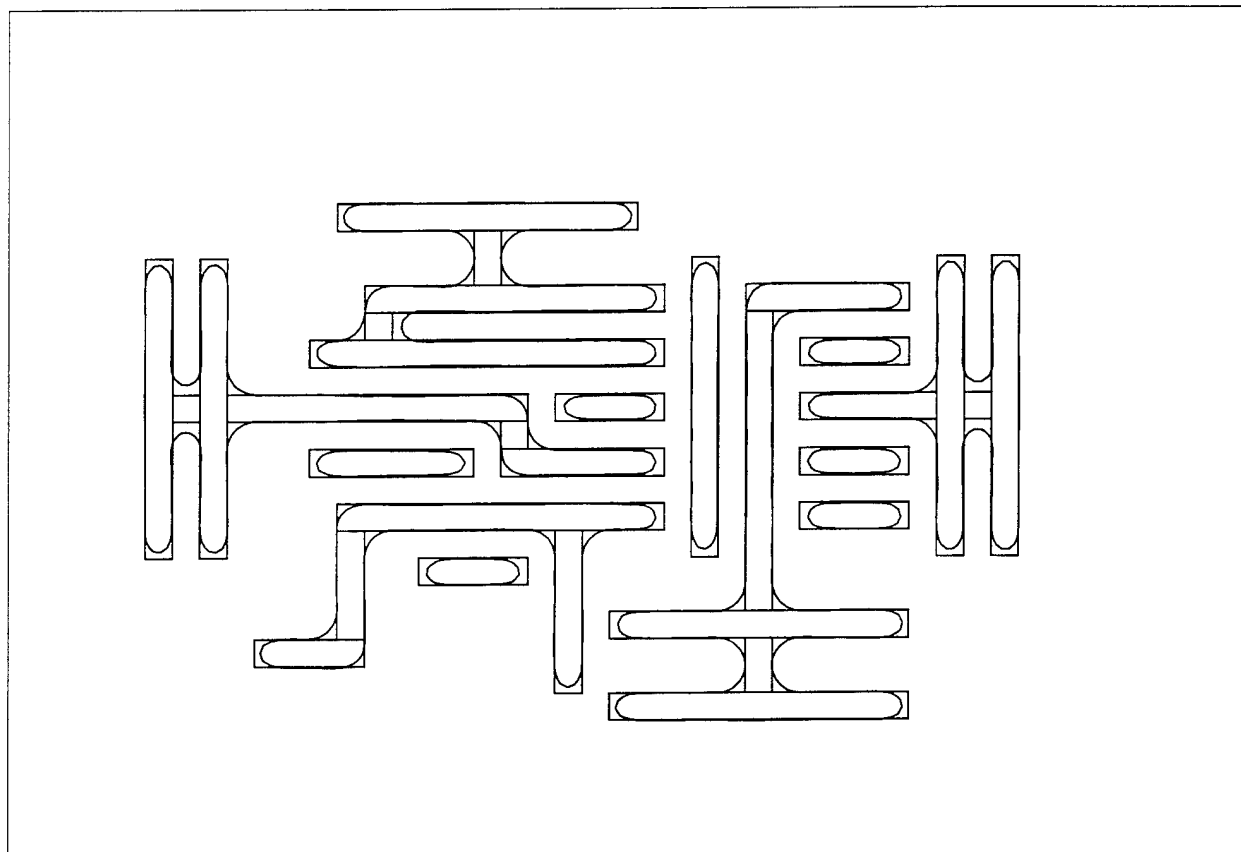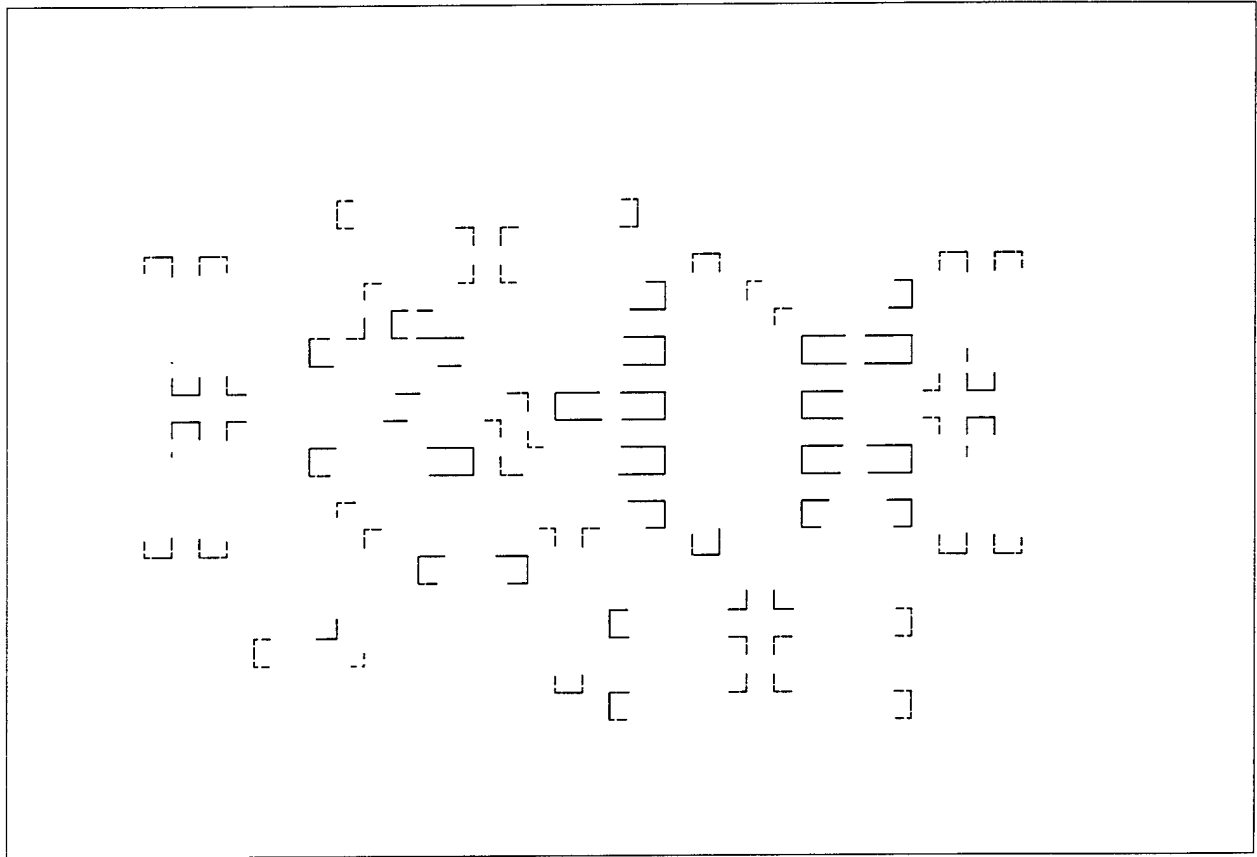Hopewell Junction, NY 12533

Eytan Barouch, Uwe Hollerbach, Steven A. Orszag
Program in Applied and Computational Mathematics
Princeton University, Princeton, NJ 08544-1000
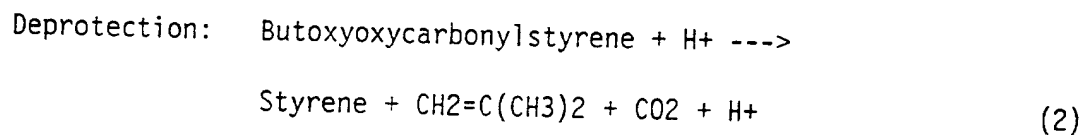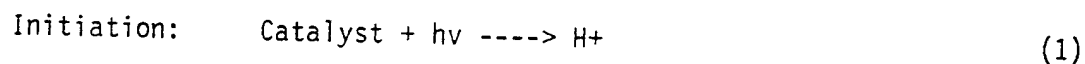
ABSTRACT

An investigation of the dissolution behavior of an acid catalyzed deep ultraviolet (DUV) positive resist has been completed. The immersion develop dissolution rate as a function of dose and post exposure bake temperature was measured by Perkin Elmer Dissolution Rate Monitor (DRM) for single layer resist on a silicon substrate. A reaction-diffusion model has been built to describe the dependence of development rate on exposure dose and post exposure bake (PEB) time/temperature. A mixed diffusion model has been built to account for catalyst diffusion and quenching. Developed images have been compared with simulated image quality, line width, and process window.

1. INTRODUCTION

A detailed experimental and theoretical study of IBM APEX-E resist, an acid catalyzed Deep Ultraviolet (DUV) positive resist, has been performed. A series of wafers have been exposed at energies ranging up to 100 mJ/cm². Nominal dose for 0.35 to 0.45μm lines is $\simeq$ 15mJ/cm². Exposures were performed on a Micrascan 92 as well as Nikon EX-2 and Canon FPA 4500 excimer laser stepper. Thus both broad band as well as 248nm single wavelength have been studied.

A variety of post exposure bake (PEB) temperatures was examined ranging from 70°C to 100°C, all with 90 seconds baking time. It was found that for equal lines and spaces and using 60 second puddle development in MF-321 developer, the relationship between mask dimension and developed image is linear. The Dill parameters were measured to be A = -0.01μm^{-1}, B = 0.16μm^{-1}, and C$'$ = 0.0042cm²/mJ, where C$'$ is the acid production rate. The real part of the refractive index at 248nm is n = 1.76, and at 632.8nm is n = 1.56.

The exposure was modeled via a semi coupled set of Maxwell and kinetic Dill equations. Exposure and PEB are the critical steps incorporating explicitly the deprotection of the polymer as exhibited in the following diagram.

Initiation: Catalyst + hv ----> H+   (1)

Deprotection: Butoxyoxycarbonylstyrene + H+ --->

                 Styrene + CH2=C(CH3)2 + CO2 + H+   (2)

Quenching: R + H+ ---> RH
                                                                             (3)

The degree of deprotection as a function of experimental conditions was followed by Fourier transform infrared (FTIR) spectroscopy and correlated with dissolution rate. For a second method of analysis, the normalized acid concentration as a function of experimental conditions was calculated from C' and correlated with dissolution rate.

The dissolution was simulated with a Hamilton-Jacobi based algorithm. The reaction-diffusion module can easily be applied as well. A detailed set of critical dimensions (CD) and line width control experiments has taken place both for broad band exposure on Micrascan 92 and NIKON EX-2 excimer laser.
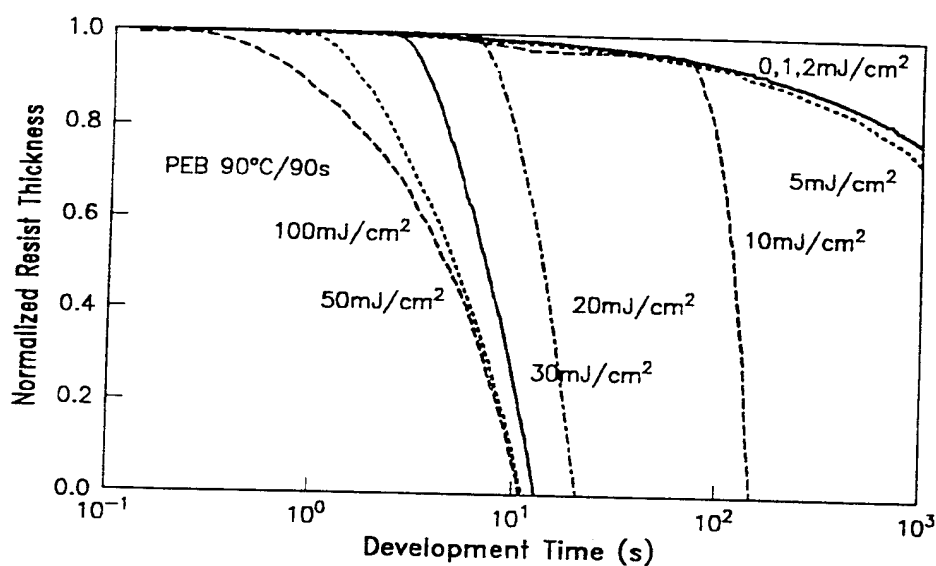
Figure 1. DRM Thickness Curve of APEX-E. Normalized APEX-E resist thickness as a function of development time and dose for a 90°C/90s PEB. Initial thickness was $0.99\mu m$ on Si exposed on a Canon FPA 4500.

2. EXPERIMENTAL

2.1 Materials

APEX-E resist is a deep ultraviolet 248nm positive chemically amplified resist[1]. Please refer to reference 1 for a detailed study. Its main ingredients are a photo acid generator (PAG), and a modified resin. The PAG is a nonionic, nonmetallic sulfonate ester of an N-hydroxy compound. The resin is approximately a 3:1 modification of para-hydroxystyrene (pHOST) to tert-

butoxyoxycarbonylstyrene (tBOC). The casting solvent is propylene glycol monomethyl ether acetate (PGMEA). If used, a resist top coat (RTC) is applied to a thickness of 150nm to provide protection from airborne chemical contamination[2]. The refractive index of RTC at 248nm is n = 1.59 and at 632.8nm = 1.51.

2.2 Processing

All silicon wafers were adhesion promoted with Hexamethyldisilazane (HMDS), coated on an SVG coater at approximately 3500 RPM for 60 seconds, and post apply baked (PAB) at 90°C for 90 seconds. Exposure was performed with overcoat using a NIKON stepper as well as without RTC using a Micrascan 92 stepper. The wafers exposed were 0.94 and 0.99μm thick, respectively, as maxima on the swing curve, determined experimentally on each tool separately.

A variety of baking temperatures and durations have been examined, and 90°C for 90 seconds has been determined as optimal. Therefor, all consequent line width measurements took place using 90°C baking temperature for 90 seconds duration.
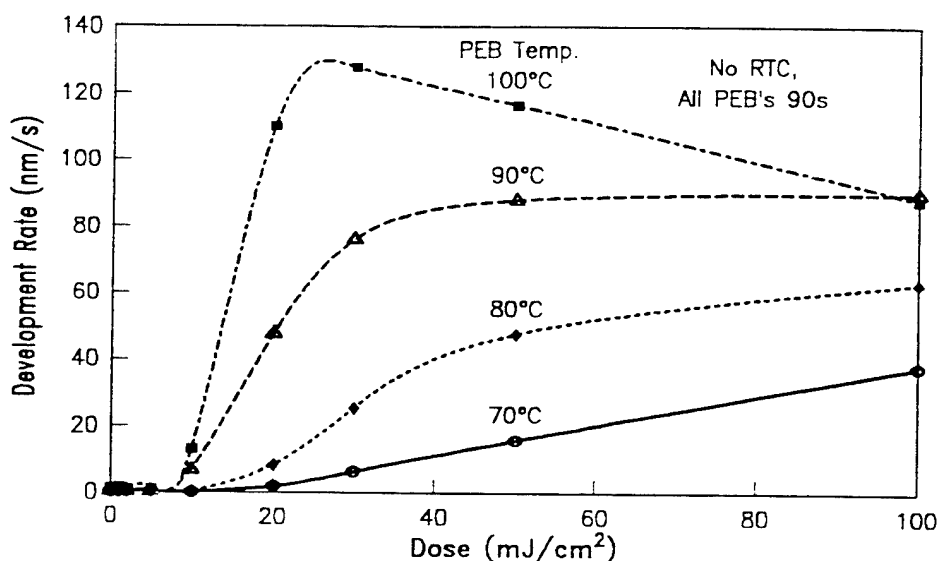
Figure 2. DRM Development Rate vs Dose of APEX-E. DRM development rate as a function of dose for 70°C to 100°C and 90 second PEB.

2.3 DRM Measurements

Dissolution results were obtained for bake temperatures of 70°C, 80°C, 90°C, and 100°C. Each baking temperature corresponds to nine different exposure doses given by 0, 1, 2, 5, 10, 20, 30, 50, and 100mJ/cm^{2} performed on a 5X Canon FPA 4500 stepper with 0.37NA and a Cymer 200Hz KrF laser. Optimal development time was determined to be 60 seconds in MF321 developer. Dissolution rate measurements were done with a Perkin-Elmer Dissolution Rate Monitor (DRM). Dissolution was followed up to 1800 seconds, so that low dose dissolution rates could be measured. The unexposed resist dissolution rate was measured to be less than 1nm/s for all bake conditions.

3. CHARACTERIZATION

3.1 Method I

Dill's coupled partial differential equations[3] describe intensity distribution $I(z,t)$ in the resist and rate of change of the normalized PAG concentration $M(z,t)$

$$\frac{\partial I(z,t)}{\partial z} = -(AM(z,t) + B)I(z,t)$$

(4)

$$\frac{\partial M(z,t)}{\partial t} = -CM(z,t)I(z,t)$$

(5)

where z = depth into the resist and t = time. These equations have been solved in closed form and reported earlier[4]. The Dill A parameter for APEX-E is $\simeq 0$ (A = $-0.01 \mu m^{-1}$), thereby decoupling equations (4) and (5). One may solve equation (4) and then integrate equation (5).

$$I(z) \simeq I_0 e^{-Bz}$$

(6)

$$M(z,t) \simeq e^{-CI(z)t}$$

(7)

Note that $I(z)t$ is dose and defining a normalized acid concentration $P \equiv 1 - M$:
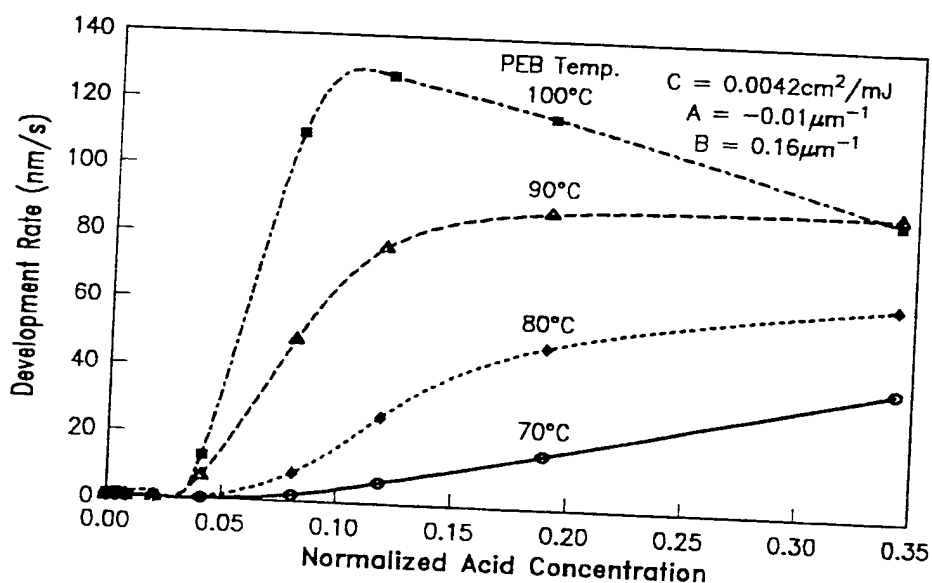
$$P(z,t) \simeq 1 - e^{-CI(z)t}$$

(8)

Figure 3. DRM Development Rate vs Acid of APEX-E. DRM development rate as a function of normalized acid as determined by equation (8).

3.2 Method II

The APEX-E pHOST backbone has an IR characteristic carbon - carbon ring stretch mode[5] at 1514cm^{-1}. The dissolution inhibiting pendant tBOC group has an IR carbon - oxygen carbonyl stretch mode[5] at 1736cm^{-1} and 1757cm^{-1} for hydrogen and non-hydrogen bonded groups respectively. At each bake temperature and exposure dose, the FTIR peak areas were ratioed to obtain the relative number of protecting tBOC groups to the total number of backbone groups[6]. These ratios were normalized for each PEB temperature to the unexposed resist *tBOC/pHOST* ratio and subtracted from 1 to calculate the normalized degree of deprotection:

$$R_i \equiv \frac{Peak \ Area \ (C = O)_i}{Peak \ Area \ (C - H)_i} \tag{9}$$

$$Deprotection_i = 1 - \frac{R_i}{R_0} \tag{10}$$

where i refers to each exposure dose.
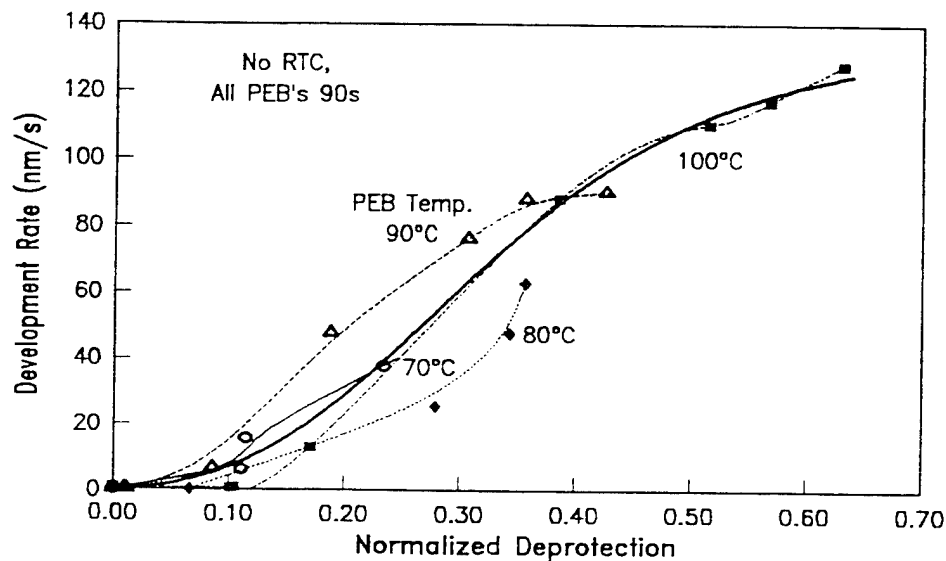
Figure 4. DRM Development Rate vs Deprotection of APEX-E. DRM development rate as a function of normalized deprotection as calculated by equation (10).

4. SIMULATIONS

The simulation was performed by the use of the MCP simulator properly modified. The aerial image was computed using the module FAIM in the following manner. A series of 2 dimensional parallel rectangles were laid on a mask and a cut line in the center of the features was extracted. Both scaler and vector (TE polarization) aerial images were computed. There was little distinction between the resultant intensities, largely due to the absence of phase shifts and relatively low NA of 0.50.

The resist thickness was taken at 0.99μm, a swing curve maximum. The exposure was modeled and numerically executed by the Maxwell-Dill material kinetic equation[7]. The solution of the oscillatory equations was obtained using spectral element methods with back substitution for the material nonlinear term. The order of the polynomials used was (2D) 25 by 45.

Figure 5. APEX-E Refractive Index and MS 92 Spectrum. The real and imaginary refractive index of APEX-E as a function of wave length superimposed on the MS 92 output spectrum.

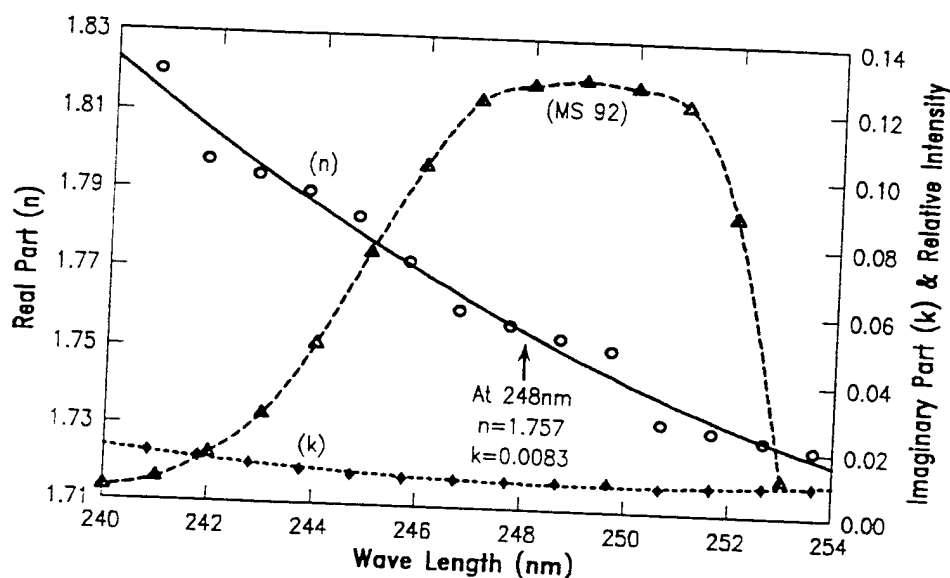The PEB was modeled by a coupled set of reaction-diffusion equations including acid quenching. Since the acid molecule quenches after 300 deprotection reactions, we have taken the quenching coefficient to 1/300. The reaction coefficient was back estimated from the dissolution data. The diffusion coefficient was taken as approximately a quarter wavelength. This diffusion coefficient was not measured but estimated by mean free path calculations. We believe that our diffusion coefficient is quite accurate since APEX-E has such a high contrast and exhibits vertical profiles.

The deprotection is obtained by the assumption that it takes place catalytically. The acid concentration served as the initial conditions. The dissolution is modeled by the Hamilton-Jacobi moving front system.

The diffusion coefficient of the moving front corresponds to the dissolution rate. The dissolution rate has been determined experimentally both as a function of deprotection concentration as well as corresponding acid concentration. This correspondence is used to verify the reliability of the PEB module.

The dissolution time is taken at 60 seconds for 90 seconds bake and the matrix performed for equal lines and spaces ranging from 0.30μm to 0.50μm in 0.05μm increments. The defocus values ranged from 0 to 1.6μm in 0.2μm increments. It should be noted that we have assumed a perfect lens, i.e. no lens aberrations. Accordingly, the plus or minus focus are symmetric.

The simulation reveals the high contrast character of the APEX-E resist as well as some of the reentrant profiles exhibited in the micrographs. The simulation matrix allows us to obtain process latitude vs defocus.
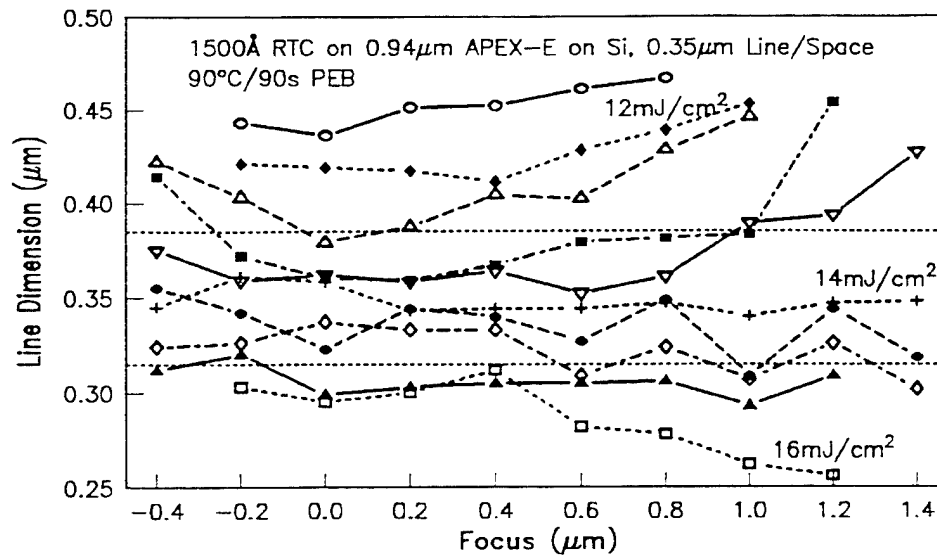

Figure 6. **Experimentally determined Focus Latitude of APEX-E on Si.** Line width as a function of focus and dose of APEX-E on Si: Nikon EX-2 with 90°C/90s PEB.
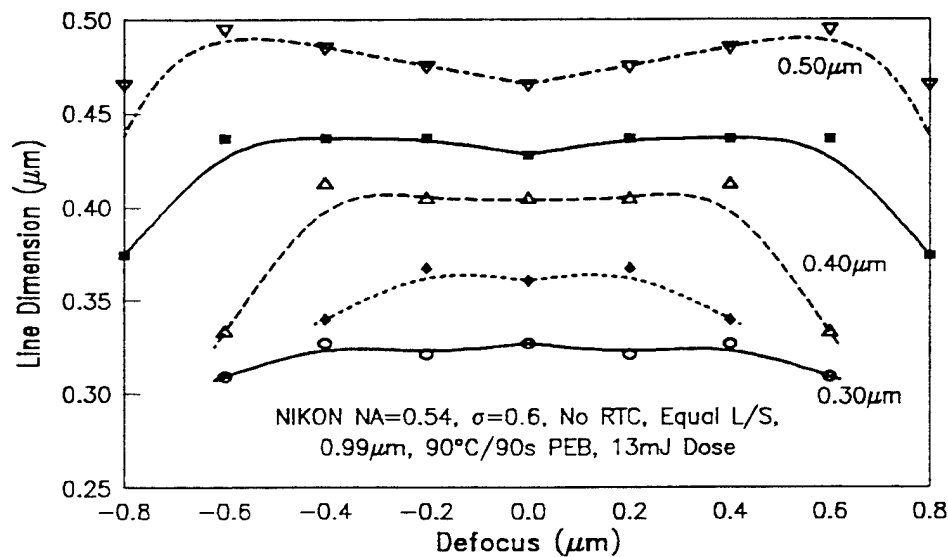

Figure 7. **MCP Simulated Focus Latitude of APEX-E on Si.** Line width as a function of focus at 13mJ/cm² of APEX-E on Si.
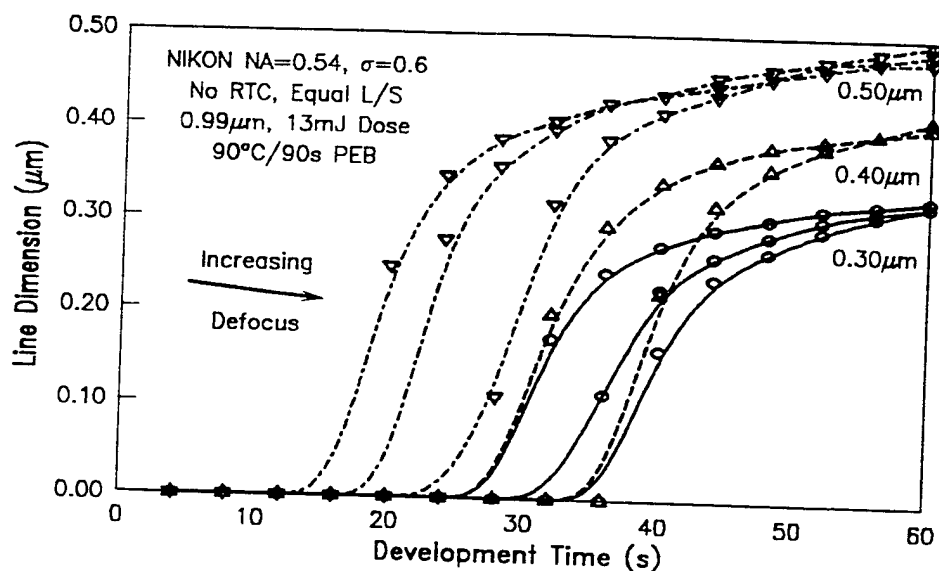
Figure 8. MCP Simulated Line Width Time Evolution of APEX-E on Si. Line width as a function of time and focus at 13mJ/cm² for APEX-E on Si.

5. DISCUSSION and SUMMARY

Of the two methods of resist characterization, normalized acid concentration is easier to determine experimentally than the normalized deprotection. Unfortunately, the IR carbon - oxygen carbonyl stretch modes of tBOC are not unique. Both residual PGMEA solvent (estimated at 2 to 5 percent) and the photo acid generator contain carbonyl groups. The presence of RTC or an Antireflective under layer would further mask the determinations.

The simple model of initiation, deprotection, and quenching is sufficient for characterizing the dissolution response of APEX-E to normal conditions. However, at high dose $\geq$ 30mJ/cm² and at a high bake temperature of 100°C, the dissolution rate decreases as a function of increasing normalized acid concentration (figure 3). The normalized degree of deprotection also increases in this regime (figure 4). A possible explanation is that APEX-E begins to cross link.

Figures 9 and 10 illustrate MCP simulated output for an array of 0.35µm and 0.50µm equal lines and spaces in single layer APEX-E on Si. Defocus was 0µm and 0.8µm respectively. Resist thickness was 0.99µm, dose was 13mJ/cm², the simulated exposure was Nikon single wavelength 248nm with NA=0.54, σ = 0.60, and no RTC. Illustrated are acid concentration immediately after exposure (please note the standing waves), diffusion after 90°C/100 PEB, and dissolution profiles at 20 and 60 seconds. There was little difference in 90 or 100 second PEB.

In conclusion, we have systematically studied the properties and characteristics of the APEX-E resist system. It reveals sharp contrast displayed explicitly in the micrographs as well as the simulations. The development rate curve vs the normalized acid concentration displays the sharp cut-off at about 0.04 normalized concentration. The dissolution rate for the optimal 90°C PEB temperature changes from nearly 0nm/s at 0.04 normalized acid concentration to 30nm/s at 0.06 normalized acid concentration, rising to a saturated value of 90nm/s at 0.13 normalized acid concentration.

We believe that the high contrast of this resist could serve as a test vehicle for lens aberrations, particularly coma and astigmatism. Furthermore, dose uniformity in the entire exposure field can be monitored.

6. ACKNOWLEDGEMENTS

7. REFERENCES

1. J. Sturtevant, S. Holmes, P. Rabidoux, Proc. SPIE 1642, 114 (1992).

2. S. MacDonald, N. Clecak, H. Wendt, G. Wilson, C. Snyder, C. Knors, N. Deyoe, J. Maltabes, J. Morrow, A. McGuire, S. Holmes, Proc. Proc. SPIE 1466, 1 (1991).

3. F. Dill, W. Hornberger, P. Hauge, J. Shaw, IEEE Transactions on Electron Devices, ED-22, No. 7, 445 (1975).

4. S. V. Babu and E. Barouch, IEEE Electron Device Letters, vol. EDL-7, 252 (1986).

5. R. Silverstein, G. Bassler, T. Morrill, *Spectrometric Identification of Organic Compounds*, 4th ed., John Wiley and Sons, New York, 1981.

6. R. Ferguson, J Hutchinson, C. Spence, A. Neureuther, J. Vac. Sci. Technol. B, vol. 8, no. 6, 1423 (1990).

7. E. Barouch, J. Cahn, U. Hollerbach, S. Orszag, J. Sci. Comput., Vol. 6, No. 3, 229 (1991).

Figure 9. MCP Simulated 0.35μm Equal Lines and Spaces in APEX-E on Si. Acid concentration, 90°C/100s PEB, and developed images at 20 and 60 seconds. APEX-E thickness 0.99μm, 13mJ/cm², 0μm defocus, simulated Nikon exposure NA = 0.54, σ = 0.60, no RTC.
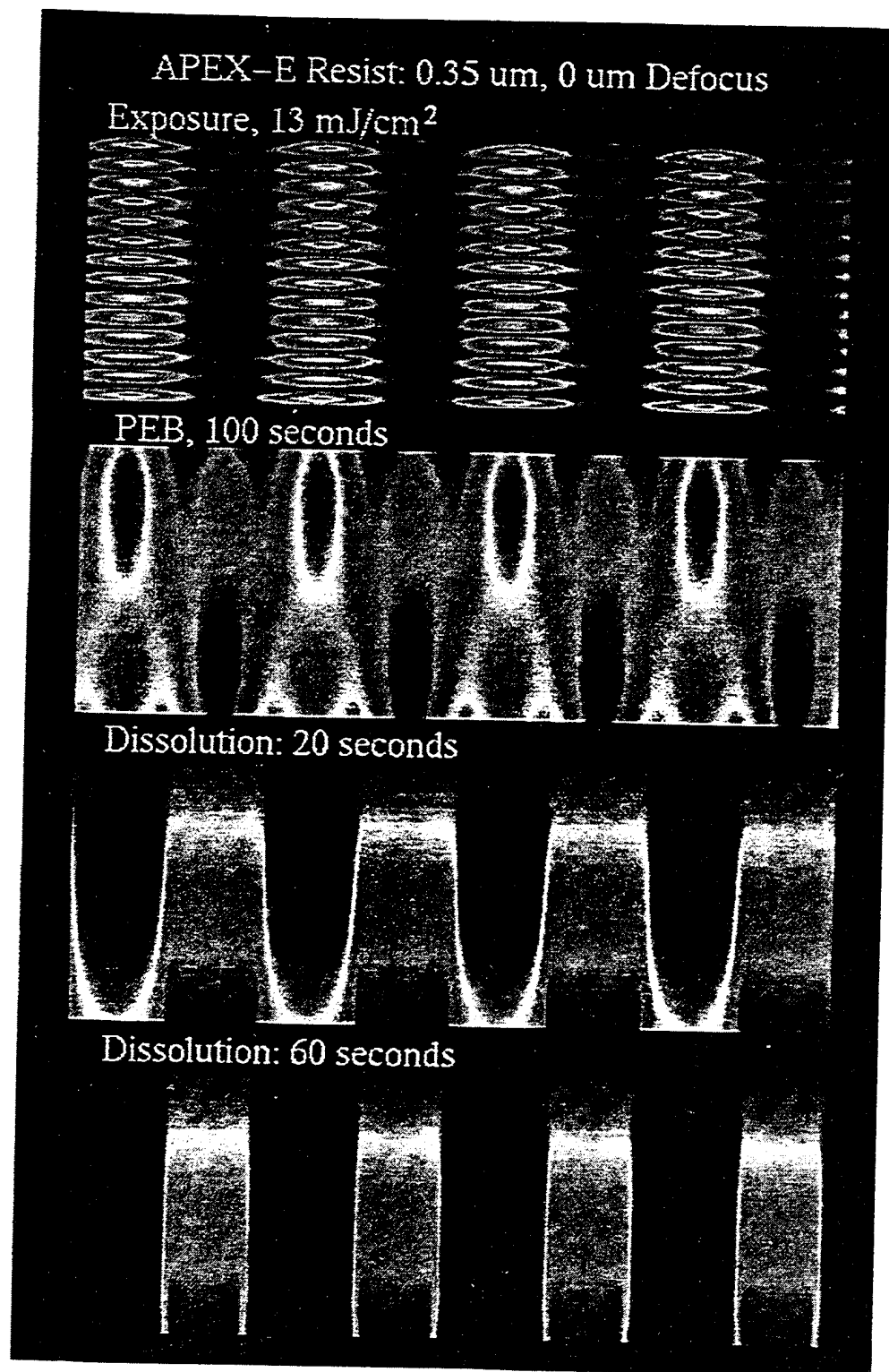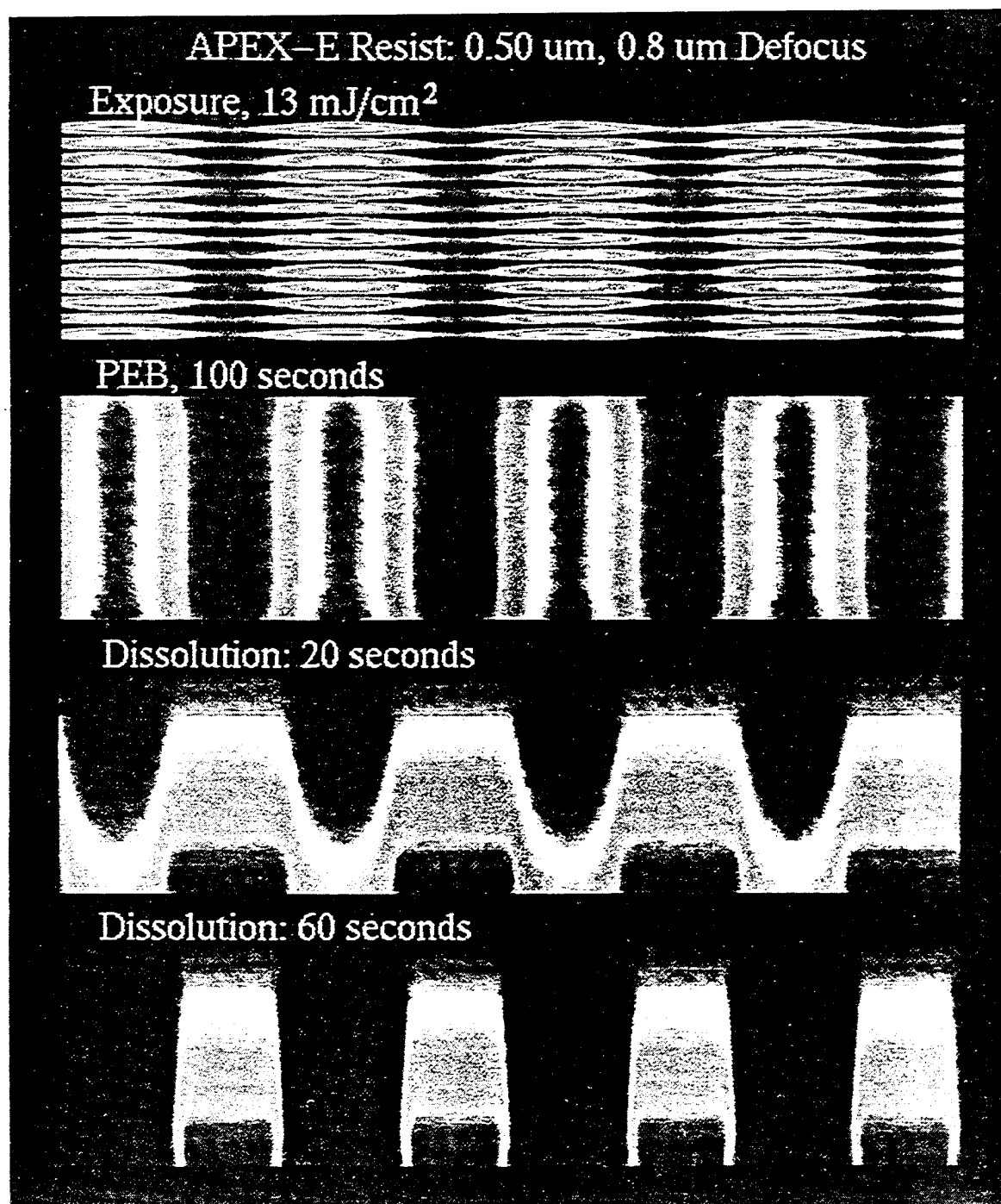
Figure 10. MCP Simulated 0.50μm Equal Lines and Spaces in APEX-E on Si. Acid concentration, 90°C/100s PEB, and developed images at 20 and 60 seconds. APEX-E thickness 0.99μm, 13mJ/cm², 0.8μm defocus, simulated Nikon exposure NA = 0.54, σ = 0.60, no RTC.

PHASE SHIFT MASK DEFECT PRINTABILITY ANALYSIS

by

John Nistler, Rajeev Singh, Eric Aplegren and Alvina Williams
SEMATECH
Austin, TX

Eytan Barouch and Uwe Hollerbach
Princeton University
Princeton, NJ

Abstract

Defect printability for 0.35 μm Phase Shift Mask (PSM) lithography was evaluated using a programmed defect test design on standard and attenuated masks of 10% and 15% transmission. The criteria used for defect printability was a +/- 10% linewidth variation through an effective focus and exposure window. Sensitivity of critical dimension (C.D.) linewidth on a positive I-line resist process to phase, size and proximity of defects on the mask was studied. Comparisons of defective areas and non-defective areas were performed to verify defect printability.

Methods of analysis were direct Ariel Image Microscopy System (AIMS), SEM analysis of reticle defects with corresponding wafer sites exposed on 4 distinct N.A. and partial coherence steppers, and large area modeling of C.D. performance using FAIM.

Statistical validation between Ariel Image Simulation, resist wafer image C.D. data, and AIMS data was done using a multi-variable nonlinear neural network analysis. Defects of different types and sizes were examined through variable focus and exposure conditions. Effective and non-effective repairs of intrusion and extrusion edge type defects were evaluated through focus and exposure conditions.

Introduction

Phase shift mask technology has been explored intensively to enhance the lithographic performance of optical and Xray projection systems. Starting with the early work by Marc Levenson[1], Hank Smith[2] and Makato Shibuya[3], PSM technology is now being explored worldwide. Technical feasibility of enhancing lithographic performance has been demonstrated experimentally by various authors for both I-line and DUV lithography.[4,5] The two main areas of concern to implement PSM technology on integrated circuits are design and the ability to produce defect free printing reticles. Useable IC capabilities has been obtained by using the voting method[6] and multiple reticle exposure[7]; but defect printability, inspection and repair are still major areas that need to be addressed.

The impact of defect size, method of defect repair, and the impact of N.A. and sigma are studied in this paper. Preliminary results and confirmation of the approach being used to predict defect printability will be presented. Ariel image simulation and ariel image measurements were done at N.A. = 0.5, sigma = 0.6. Resist image and critical dimension results were obtained at N.A.=0.40, 0.48, 0.5, 0.54 and sigma= 0.6, 0.54, 0.6, 0.48 respectively. All C.D. measurements were obtained for resist on silicon images using either KTI 895i or Shipley 3813 resists.

Programmed and non-programmed defects were studied. Direct reticle verification was correlated to printed focus/exposure wafer results whereas repaired and programmed defects were studied by ariel image microscopy (AIMS) and resist printability studies.

PHASE SHIFT MASK DEFECT PRINTABILITY ANALYSIS

by

John Nistler, Rajeev Singh, Eric Aplegren and Alvina Williams
SEMATECH
Austin, TX

Eytan Barouch and Uwe Hollerbach
Princeton University
Princeton, NJ

Abstract

Defect printability for 0.35 μm Phase Shift Mask (PSM) lithography was evaluated using a programmed defect test design on standard and attenuated masks of 10% and 15% transmission. The criteria used for defect printability was a +/- 10% linewidth variation through an effective focus and exposure window. Sensitivity of critical dimension (C.D.) linewidth on a positive I-line resist process to phase, size and proximity of defects on the mask was studied. Comparisons of defective areas and non-defective areas were performed to verify defect printability.

Methods of analysis were direct Ariel Image Microscopy System (AIMS), SEM analysis of reticle defects with corresponding wafer sites exposed on 4 distinct N.A. and partial coherence steppers, and large area modeling of C.D. performance using FAIM.

Statistical validation between Ariel Image Simulation, resist wafer image C.D. data, and AIMS data was done using a multi-variable nonlinear neural network analysis. Defects of different types and sizes were examined through variable focus and exposure conditions. Effective and non-effective repairs of intrusion and extrusion edge type defects were evaluated through focus and exposure conditions.

Introduction

Phase shift mask technology has been explored extensively to enhance the lithographic performance of optical and Xray projection systems. Starting with the early work by Marc Levenson[1], Hank Smith[2] and Makato Shibuya[3], PSM technology is now being explored worldwide. Technical feasibility of enhancing lithographic performance has been demonstrated experimentally by various authors for both I-line and DUV lithography.[4,5] The two main areas of concern to implement PSM technology on integrated circuits are design and the ability to produce defect free printing reticles. Useable IC capabilities has been obtained by using the voting method[6] and multiple reticle exposure[7]; but defect printability, inspection and repair are still major areas that need to be addressed.

The impact of defect size, method of defect repair, and the impact of N.A. and sigma are studied in this paper. Preliminary results and confirmation of the approach being used to predict defect printability will be presented. Ariel image simulation and ariel image measurements were done at N.A. = 0.5, sigma = 0.6. Resist image and critical dimension results were obtained at N.A.=0.40, 0.48, 0.5, 0.54 and sigma= 0.6, 0.54, 0.6, 0.48 respectively. All C.D. measurements were obtained for resist on silicon images using either KTI 895i or Shipley 3813 resists.

Programmed and non-programmed defects were studied. Direct reticle verification was correlated to printed focus/exposure wafer results whereas repaired and programmed defects were studied by ariel image microscopy (AIMS) and resist printability studies.

11

Test Conditions

Eight reticles were studied for this work, 5 programmed and 3 non-programmed reticles: an alternating product reticle, a SRS test reticle and a outrigger test reticle. (Table 1) Only SEM analysis will be presented on the non-programmed reticles. The programmed defect test pattern is illustrated in figure 1. The pattern consisted of varying line/space widths with a 0.7 μm pitch. Due to resolution limitations, certain smaller defects did not resolve. The quartz was etched on the attenuated plates to achieve the 180 degree phase difference. It was found later that the phase of the chrome was incorrect. The data in the neural network program therefore uses the bulk phase associated with each mask. The non-programmed defect test reticles were contact test patterns that varied in size, pitch, rim size or center spacing. The product reticle tested was a multiphase alternating approach on an 8 Meg EPRom. Critical dimensions on reticle and corresponding wafers at 1X were measured and input into the NNAPER Neural network analysis. The measured data size for the defects are entered in X and Y dimensions.

Table 1: I-line

Reticle	Reticle Type	Defect types	# of Masks
1	Binary	Programmed	1
2	PSM (Attenuated, 10%)	Programmed	2
3	PSM (Attenuated, 15%)	Programmed	2
4	PSM (Alt. Aperture)	Real	1
5	PSM (Rim)	Real	1
6	PSM (Outrigger)	Real	1

Programmed defects were designed to be of sizes ranging from 0.05 μm X 0.05 μm to 0.20 μm X 0.40 μm at increments of 0.05 μm. The chrome defects were either intrusions or extrusions. The phase defects were extrusions on a chrome line designed with a 150 degree phase error. The binary control mask was fabricated on normal medium reflective chrome and the attenuated PSM masks were fabricated on thin chrome.

The printability of the defects were studied under different wafer exposure conditions. The processing conditions used are given in Table 2.

Table 2: I-line

	Stepper	N.A.	Sigma	Track system	Resist
1)	Nikon Body 8	0.5	0.6	MTI	Shipley 3813
2)	ASML 5500/60	0.54	0.48	TEL Mark VK	TI895
3)	ASML 5000/40	0.40	0.60	SVG88	Shipley 3813
4)	ASML 5000/50	0.48	0.54	SVG88	Shipley 3813

The critical dimension variations on the wafer were studied at three sites for each programmed defect as illustrated in figure 2. CD3 is used as the control and was measured significantly far enough away from the defect to not be influenced by the defect. Linewidth edge roughness on the 10% attenuated reticles was severe enough to cause impact on the CD1 and CD2 data.

The C.D. measurements on the wafers were done using the AMRAY 1830 and the KLA SEMSPEC. The 3 sigma measurement variance specification for the AMRAY is +/- 0.02 μm while the SEMSPEC is +/- 0.005 μm. The C.D.'s were measured on the line at the location of the defect (CD1), on the line across from the defect (CD2) and at a non-defective portion of the line (CD3). Five measurements were made at each location for CD2 and CD3. The measurements were than averaged. Only a single measurement could be made on CD1 and CD2 due to the "curved" nature of the defects when printed. An example of the SEM micrographs taken on the wafer is shown in figure 3.

The AIMS analysis was done at IBM Eastview research center on a prototype research tool which utilizes mercury arc lamp illumination on a UV/DUV optical microscope system. The I-line (365 nm) ariel image is captured directly by the UV/DUV CCD camera. Since the system is a magnification system and not a reduction system, numerical aperture and sigma of a stepper system can be replicated through the correct selection of apertures. A 0.1 N.A. on the AIMS tool is used to represent a 5X 0.5 N.A. stepper. Higher N.A. stepper approximation may be question- able on the system, but it is believed that stepper N.A.'s of 0.5 or less can be emulated effectively. Critical dimension determination and repeatability will be shown under the test results section.

The large area ariel image simulation was done using FAIM on a Silicon Graphics Indigo workstation. The software uses Hopkin's diffraction formula. All simulations were done in TE vector analysis. The simulations were done for defect sizes and defect types as illustrated in Figure 4 for line space ratios of 0.30/0.40 and 0.35/0.35 μm at 1X.

Correlation of C.D. results between simulation, AIMS and resist work was done using the NNAPER Neural Network software developed by DuPont Research. Simulated C.D. results were used to train the Neural Network and then a linear regression fit of the predicted results from the model was compared to the AIMS data. The actual linewidths on the mask are slightly different than simulation due to mask processing. The Neural Network software uses back-propagation methods and conjugate gradient algorithms to fit the data and a linear regression analysis package to compare predicted results to real test data.

Test Results

Some basic issues in analyzing the data was discerned after the reticles were manufactured. The actual critical dimensions on the reticles at 1X were typically higher than design by 0.03 +/- 0.01 μm. Severe edge roughness was noted on the 10% attenuated reticles. Improvements in reticle processing helped on this problem. (figure 5) The edge roughness on the plates affected the C.D. variance at 0.35 μm on wafer by as much as 0.04 μm, three sigma. The averaging routine used on the SEM wafer measurements eliminate most of the linewidth variation at local sites, but the CD1 data is impacted. The actual dimensions used in simulations and the real measurements off of the reticle are incorporated in the neural network data analysis package, NNAPER. We also found that the specified phase of the thin chrome from the blank manufacturer was incorrect, as an example, the manufacturer's specified phase was 31 degrees on one plate but was actually measured at 9 degrees. The reason for the phase delta is due to the manufacturer using n(i) and k to determine phase, but for thin chrome the attenuation affects are highly dependent on thickness. (figure 6) Therefore the phase error on the thin chrome attenuated plates could be as high as 25

degrees. Reflectivity was also found to vary with the thin chrome on different plates with reflectivities as high as 41% recorded.

Comparison of resist images obtained using a stepper with an N.A. of 0.5 and a sigma of 0.6 to the ariel image microscopy (AIM) image indicated fairly good correlation to the extrusion programmed defects but not as good a correlation to intrusion programmed defects (Figure 7). Examination of the optical components on the AIMS tool showed that the band pass filter at I-line had degraded with use. The band pass filter has been replaced and significant improvements have been noted. Critical dimension correlation to simulated C.D. at zero focus is well within 0.02 μm and may be better. The reticle used was found to have a 0.38 +/- 0.02 μm linewidth dimension whereas the simulation was ran at 0.35 μm. The difference determined was about 0.04 μm (Figure 8). Repeatiblity through focus on the AIMS tool is still being studied. Correlation between resist and AIM's metrology is shown in Table 3. In general, as a prototype tool we see good qualitative performance, such as determining defect printability, but work is still necessary to obtain good quantitative correlation.

As expected it was found that defect printability was related to linewidth size and defect size (Figures 9). The numerical aperture, N.A., and the partial coherence interact, sigma, interact on the defect printability, but we found that generally defect areas for attenuated chrome of 0.30 μm^2 or greater on the edge of the chrome caused C.D. variance greater than 10%.

The reticles and wafers were examined before and after repair of the programmed defects. The most effective repairs achieved were on the intrusion type of defects. The critical dimension control of the different types of repairs using a Nikon Body 8 stepper with an N.A. of 0.5 and a sigma of 0.6 are illustrated in figures 10 and 11. The most interesting results of the repairs was that etching though to 360 degrees and backfilling with opaque material was fairly successful. The repair of opaque material and the quartz bumps were not as successful due to "riverbedding" effects . The main difficulties with the repair were imaging the defect and positional accuracy control of the ion beam during repair.

13

In evaluating the non-programmed defect reticles, it was typically found that defect printabilities were caused by large 180 degree phase defects (Figures 12 and 13). The alternating multiphase reticle was the exception because no phase defect greater than 60 degrees was on the reticle by design. The alternating multiphase product reticle was found to have no printable phase defects on the wafer when examined using the KLA SEMSPEC. The other two reticles had in excess of 100 printable phase defects. Defect resolution on this tool is better than 0.25 μm^2. The design approach used on the alternating reticle was not used on the other two reticles.

Summary

Defect printability was analyzed using two new prototype tools the IBM Ariel Image Microscopy System (AIMS) and the KLA SEMSPEC wafer inspection and C.D. tool. The results were compared between FAIM ariel image simulation, AIMS direct ariel image measurements and resist images. It was found that defects greater than 0.30 μm^2 (1X) on attenuated 10% and 15% transmissive reticles printed under the stepper conditions studied. Apparently under the stepper conditions studied, there was not a significant dependence on Numerical aperture and sigma as far as defect printability. Smaller sigmas need to be explored to determine defect printability dependence on sigma. This data can be added directly to the neural network analysis already started.

As expected there was a definite defect printability impact on smaller versus larger linewidths. In the case studied, defect size in X had more impact than defect size in Y, but defect areas tended to have similar results as long as the dimensions in x or y was less than two-thirds of the linewidth.

The AIMS tool was found to be a good qualitative predictor of printability results, but problems with the bandpass filter limited the quantitative usefulness. Agreement to simulation was not found to be consistent. Work will have to be continued now that the bandpass filter has been corrected.

All phase shift approaches showed improvements over the binary mask in resolution capabilities using the Shipley 3813 and KTI 895i resists, but it is felt that some work will have to be repeated using a more advanced resist to increase the effective depth of focus at 0.35 μm.

Acknowledgement

References:

1.) M. D. Levenson, N. S. Viswanathan and R. A. Simpson: *IEEE Trans. Electron Devices ED-29* (1982) 1828.

2.) D. Flanders and H. Smith. U.S. Patent # 4,360,586. Nov. 23, 1982.

3.) M. Shibuya. Japanese Patent # 62-50811, 62nd yr of Emperor Showa. pg. 15811, September 30, 1980.

4.) T. Terasawa, N. Hasegawa, T. Kurosaki, and T. Tanaka: *Proc. SPIE*, 1088 (1989) p. 25.

5) J. L. Nistler, M. Preil and B. Singh. *KTI Microlithography Conference* (1991) p. 295.

6) J.Nistler, G. Hughes, A. Muray and J. Wiley. *SPIE* 1604 (1991) p. 236.

7.) H. Sewell. *SPIE*. March, 1993.

8.) Franklin Kalk. DuPont Research. Wilmington, Conn.

9.) James N. Wiley. "Process Effects in 5X Reticle Defect Printability". *9th Annual Symposium of BACUS*. 1989.

Defocus Asymmetry in Projection Printing

Eytan Barouch, Uwe Hollerbach*, and Steven A. Orszag
Applied and Computational Mathematics
Princeton University, Princeton, NJ 08544-1000
*Dept. of Mathematics and Computer Science
Clarkson University, Potsdam, NY 13699

Abstract

The effect of defocus asymmetry in photolithography has been modeled by modifying FAIM to incorporate the phases of all partial fields emanating from the illuminator. Each partial field exposes the resist independently, and the integration over the illuminator takes place inside the resist, thus accounting for the correct physics of partially coherent light projection. Linewidth versus defocus is obtained as an asymmetric function around zero defocus, as found experimentally.

1. Introduction

Modeling of lithographic projection printing employs the physical interaction of the projected light with the photoresist film, allowing the printing of the circuit image on the wafer. The natural function to consider is the incident light intensity, since most early systems employed rather low numerical aperture (NA). The low numerical aperture also implies that the dominant direction of the light propagation is vertical.

With the development of projection tools of NA = 0.62 and the need for at least $1.2\mu m$ defocus budget, the basic issue has become much more complex. In particular the partially coherent light employed in IC manufacturing is projected from an illuminator which is divided into many sub-illuminators, all of which are independent of each other, thus creating many mutually incoherent subfields. The projected aerial image is formed by adding the intensities of to these subfields with the appropriate weights.

The exposure of the photoresist is modeled by the Maxwell-Material equations, which require the phases as well as the absolute value of the fields as boundary conditions, implying that each sub-field must expose the resist independently, and the resulting partial intensities inside the resist be added (integrated) as before.

The physics behind this elaborate analysis is actually very simple. When the Gaussian focus plane of the projected IC design is on top of the resist surface, the needed process latitude is about $1.2 - 1.6\mu m$. Since the resist thickness is typically $1\mu m$, the projected intensity could be focused $1\mu m$ above the resist surface ($+1\mu m$ defocus), as well as below.

These two cases are fundamentally different from each other: in the $+1\mu m$ defocus case the resist is irradiated with light rays which are diverging at the top resist surface, while in the $-1\mu m$ defocus case the incident rays are converging at the top resist surface. This difference immediately implies that the entire process will be **asymmetric** for $\pm$ defocus and that the critical dimension (CD) control of linewidth vs. defocus will not be symmetric around zero defocus.

It is the purpose of this paper to introduce our solution to this problem and to illustrate its application and utility.

2. Formulation

The exposure of the resist has been formulated in detail earlier[1--3]. Here, for completeness, we briefly present the basic equations:

$$\nabla^2 \mathbf{E} + \left(\frac{2\pi}{\lambda}N\right)^2 \mathbf{E} + \nabla(\mathbf{E} \cdot \nabla log(N^2)) = 0$$

$$\frac{\partial M}{\partial t} = -CM\mathbf{E} \cdot \mathbf{E}^*$$

$$N = n - i\frac{\lambda}{4\pi}[AM + B]$$

$$\frac{\partial \mathbf{E}}{\partial \nu} + ikN_{\text{ext}}\mathbf{E} = 2ikN_{\text{ext}}\mathbf{E}_{\text{in}}$$

Note that the actual kinetics inside the resist is dependent on the *intensity* in the resist while the boundary conditions as well as the Maxwell-material equation depend on the fields.

The formulation of the projected intensity for partially coherent light is classically given by HH Hopkins' expression[4]:

$$I = \int_{\text{illuminator}} |\mathbf{E}_{\xi\eta}|^2 \, d\xi d\eta$$

with $\mathbf{E}_{\xi\eta}$ being the projected field due to the (ξ, η) illuminator subdomain. The field $\mathbf{E}_{\xi\eta}$ is a convolution of the mask function (the characteristic function of the mask $\times$ the plane wave emanating from the illuminator) with the "coherent transfer function" of the imaging optical system. Its most desired way of computation is the fast Fourier transform (FFT). However, the CAD layout of the mask does not reside on a uniform grid which is needed by the FFT algorithm. Recently we reported that we found a map that transforms the

information from the non-uniform grid to the one imposed by the physics of the problem, and also evaluated the FT of the coherent transfer function analytically, thus allowing the computation of all sub-fields for any domain. For the purpose of the current investigation we compute all the partial fields, each of which is a different boundary condition for the Maxwell solver, meaning that we need to solve the Maxwell eqn several hundred times for each kinetic time step.

Once the exposure is completed, our standard post-exposure bake (PEB) and dissolution models are applied to complete the simulation for each defocus value. The assembly of these codes has resulted in a robust code called PROCPHASE that calculates linewidth versus defocus, exposure energy, etc.

3. Examples

A. Linewidth CD over a nitride layer in micro devices:

In many devices, the nitride layer is produced by CVD (chemical vapor deposition). As technology changes from G-line to I-line to deep UV, the CD control of linewidth is strongly dependent on the nitride layer thickness, so the problem of the "swing" curve observed experimentally must be simulated in order for optimal nitride layer thickness to be achieved. We have modified our basic algorithms (PROCPHASE) to address this issue. In fig. 1–a to 1–d we display the "swing" curves of $0.5\mu m$ and $0.7\mu m$ feature size for both $0\mu m$ and $-0.8\mu m$ defocus. The linewidth versus nitride layer thickness is highly oscillatory. Note also the proximity effect, since both central and edge linewidths are displayed. The dependence on defocus is not nearly as strong as the dependence on the nitride layer thickness. In fig. 2 we display the line shape for three different nitride layer thicknesses. The foot imprints of the lines at $0.145\mu m$ nitride layer thickness are very clear and distinct.

B. Asymmetry between positive and negative defocus:

We have taken a cut across the "Nikon mask" and in fig. 3 we compare results for exposure, PEB, and dissolution at positive and negative defocus. The resist employed for this illustration was the IBM Spectralith resist, and, as can be seen from the PEB line, the threshold for resolution can be obtained for $-1\mu m$ defocus with I-line and $0.35\mu m$ feature size, while the image at $+1\mu m$ defocus is completely dissolved. Using the same resist, a detailed study of 0.5, 0.45, 0.4, and $0.35\mu m$ feature sizes was performed and is shown in fig. 4. The asymmetry between positive and negative defocus is very distinct at high defocus values, while at very low defocus values the linewidths and lineshapes are nearly identical. Both fig. 3 and fig. 4 demonstrate unequivocally the necessity of using the correct physics in defocus end range simulations.

C. Focus latitude of the APEX-E photoresist:

To illustrate the power of PROCPHASE, we display in fig. 5 a linewidth versus defocus of $0.35\mu m$ feature size using Apex-E resist and 3D-FAIM over silicon oxide and silicon. The iso-focal line is very distinct, and the asymmetry for this system is very clear.

The Apex-E resist has very different properties than any other existing resist, since the chemistry of its PEB is unconventional. Thus characterization of its focus latitude for $0.35\mu m$, $0.3\mu m$, and $0.25\mu m$ is impossible to simulate using conventional methods. In particular, its high sensitivity requires very precise exposure. We have combined our modified exposure methodology with new PEB algorithms which specifically model the kinetics of the PEB reaction-diffusion system, to provide a timely solution to this simulation problem.

In fig. 6 we present an exposure-defocus set of curves for the nominal linewidth of $0.35\mu m$ feature sizes, where the exposure energy varies from 12 to $16mJ/cm^2$. The resist thickness is $1\mu m$ over a silicon oxide gate and a silicon substrate. It is clear that there is a drastic change in linewidth both at 0 and at $-1\mu m$ defocus, i.e., the system distinguishes whether the light is focused inside or outside the resist.

In fig. 7 we display a design of an SRAM where linewidth versus defocus has been modeled across two transistors. The sublayer is α-poly-silicon over oxide over a silicon substrate. In other words, we are actually looking at a poly-layer CD versus defocus. In fig. 8 we show the linewidth versus defocus for this model gate system for three exposure energies: 14–$16mJ/cm^2$. As before, when the Gaussian focus plane lies outside the resist we observe a distinct deterioration in linewidth control. From these studies we conclude that the Apex-E resist is highly suitable for quarter-micron feature size printing at about 1 micron focus budget for about 1 micron thick resist. These findings are in agreement with the measurements performed by N. Eib and reported earlier.

4. Conclusion

We have obtained an algorithmic solution to the complicated problem of high defocus electromagnetic exposure of photoresist with partially coherent light. The newly developed algorithm has been implemented and tested against existing data obtained from experimental defocus studies. The implementation of the algorithm has applications to various parts of microdevice fabrications, and as such is expected to be technologically transferred to both universities and industry.

5. Acknowledgments

6. References

1) E. Barouch, J. H. Cahn, U. Hollerbach, and S. A. Orszag, "Numerical Simulation of Sub-Micron Photolithographic Processing", J. Sci. Comp. **6**, 3, 229 (1991).

2) E. Barouch, D. Cole, U. Hollerbach, and S. A. Orszag, "Vector Aerial Image with Off Axis Illumination (FAIM)", Proceedings of SPIE **1927** 686 (1993).

3) Dill, F. H. 1975 *IEEE Trans. Electron Devices*, **ED-22** 440–444.

4) Hopkins, H. H. 1953 "On the Diffraction Theory of Optical Images", *Proc. Roy. Soc. London*, Ser. A 217, 408–432.

7. Figure Captions

Fig. 1. Linewidth versus nitride layer thickness for 0.5 and $0.7\mu m$ linewidth at 0 and $-0.8\mu m$ defocus with silicon dioxide gate and silicon substrate: (A) $0.7\mu m$ linewidth and $0.0\mu m$ defocus; (B) $0.7\mu m$ linewidth and $-0.8\mu m$ defocus; (C) $0.5\mu m$ linewidth and $0.0\mu m$ defocus; (D) $0.5\mu m$ linewidth and $-0.8\mu m$ defocus.

Fig. 2. Actual dissolved profiles for three different nitride layer thicknesses: 0.18, 0.145, $0.115\mu m$. Note distinct footprint of $0.145\mu m$ layer.

Fig. 3. Defocus asymmetry of a cut across the "Nikon" mask for $\pm 1\mu m$ defocus using AZ-Spectralith resist.
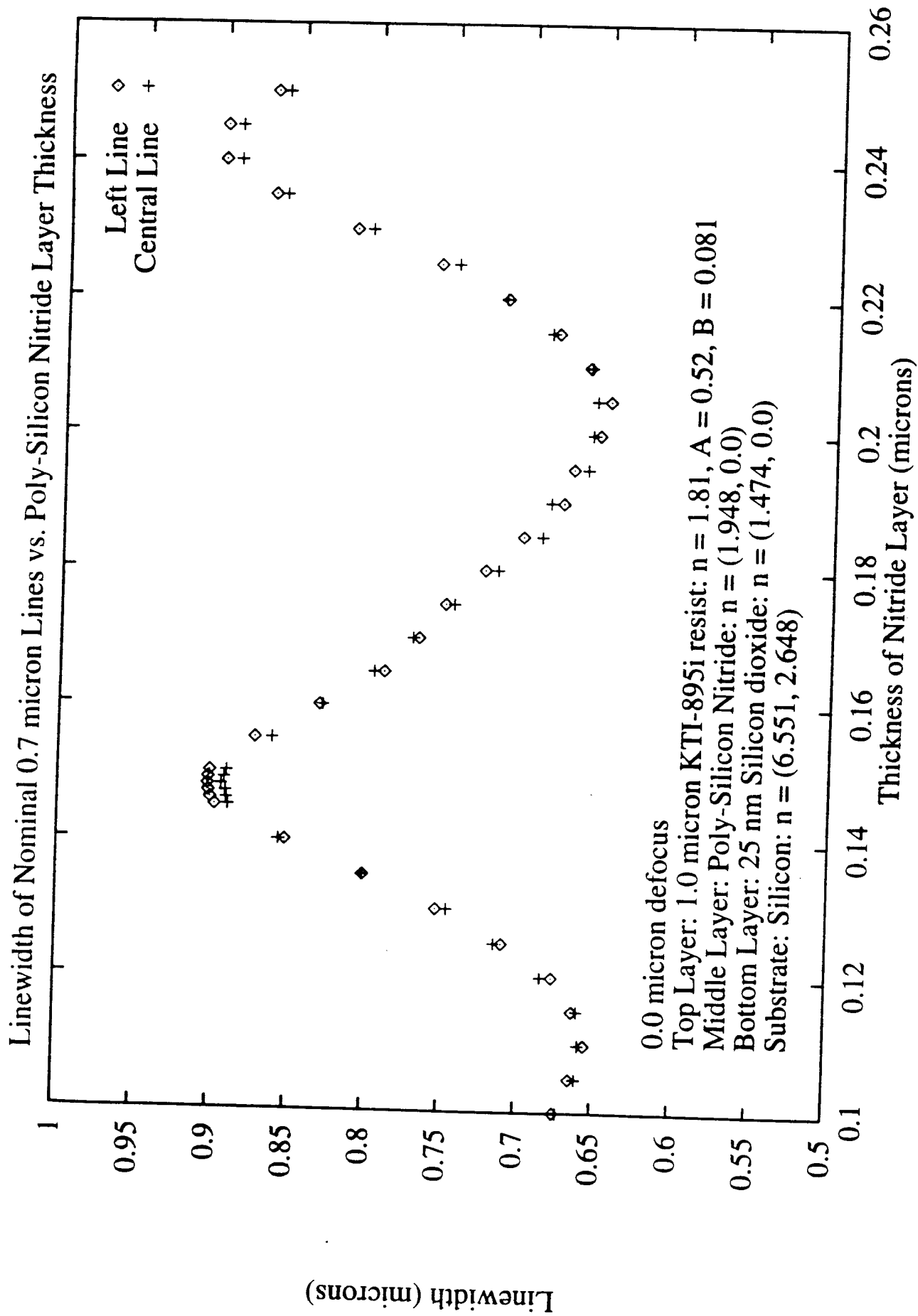
Fig. 4. Defocus asymmetry study for 0.5, 0.45, 0.4, $0.35\mu m$ lines using AZ-Spectralith resist. The asymmetry in line shapes is very distinct.
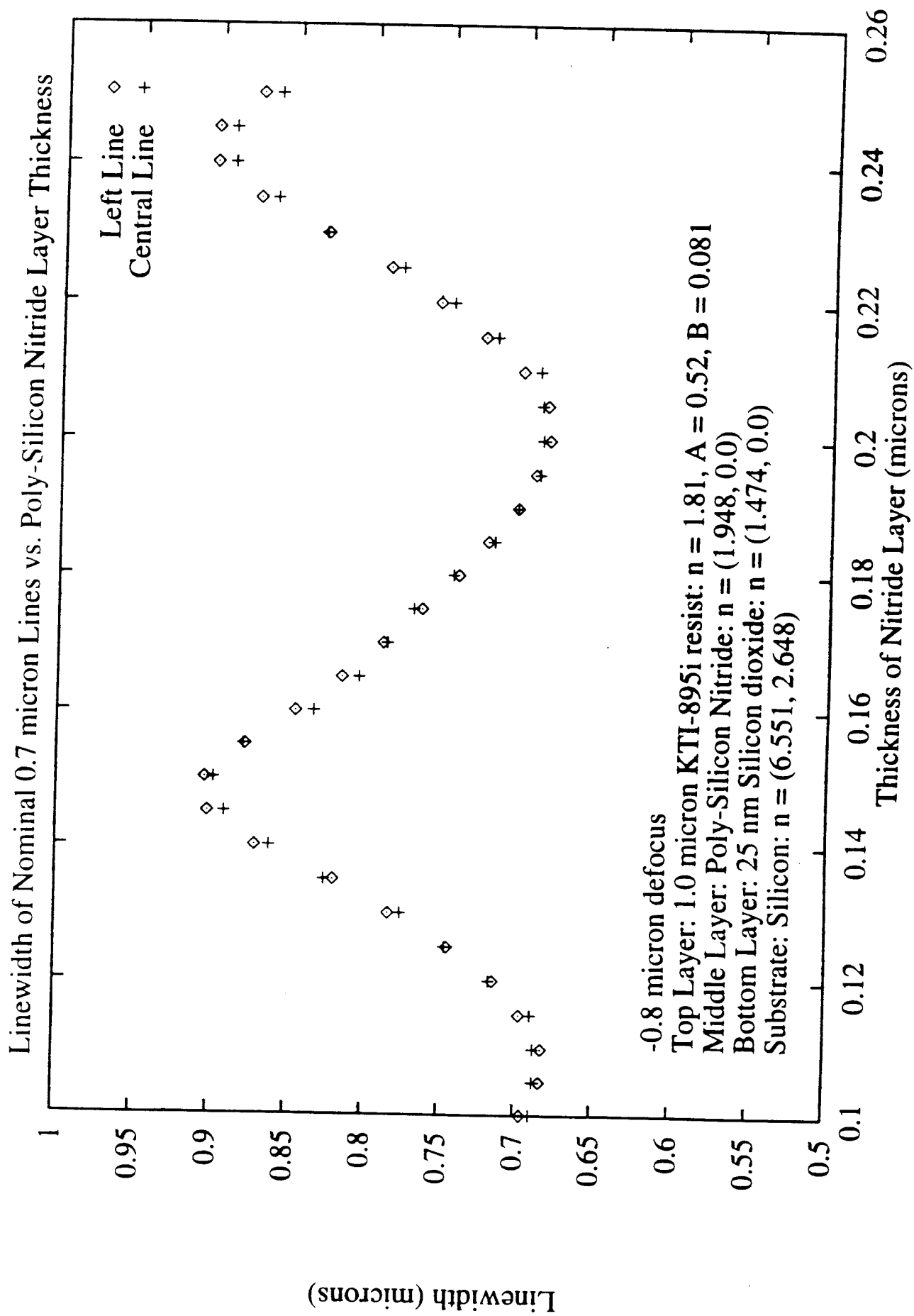
Fig. 5. Linewidth versus defocus of $0.35\mu m$ feature size using Apex-E resist and 3D-FAIM over silicon oxide and silicon.

Fig. 6. Exposure-defocus set of plots with nominal linewidth of $0.35\mu m$, exposure energy of 12–16 mJ/cm^2.
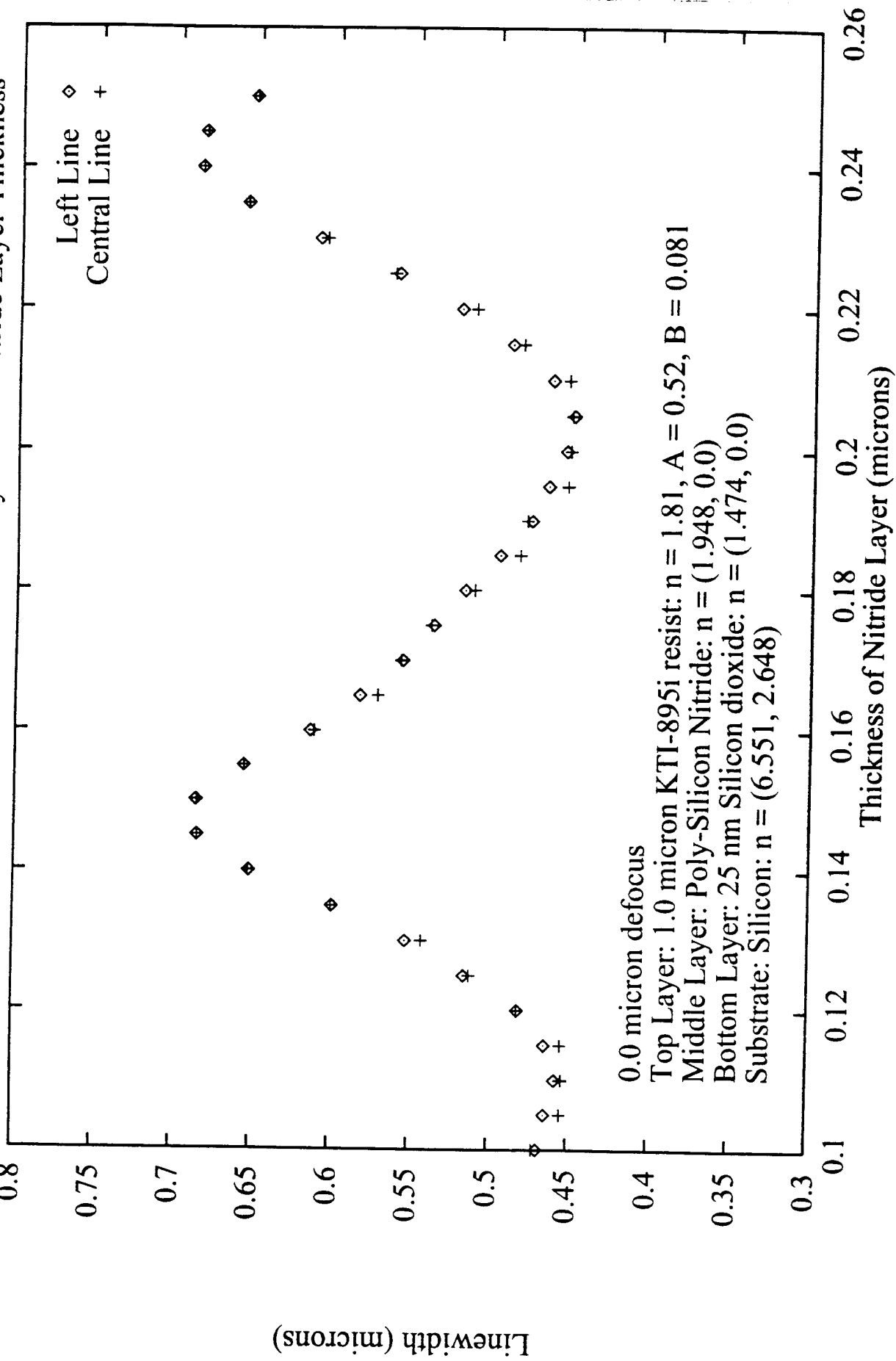
Fig. 7. SRAM design with a cut across two transistors.

Fig. 8. Linewidth of the transistors versus defocus using Apex-E resist over α-polysilicon over oxide over silicon.
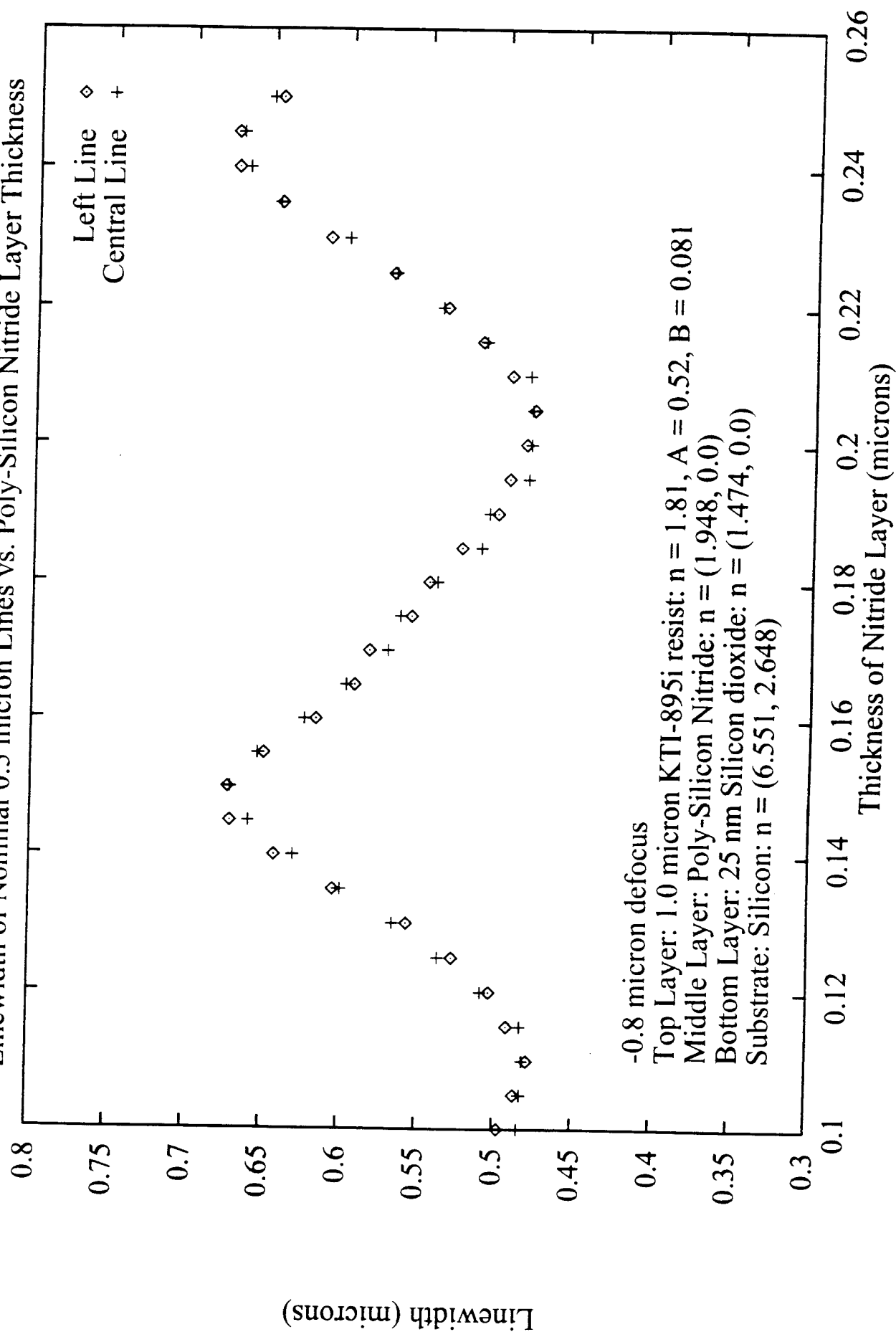
Linewidth of Nominal 0.7 micron Lines vs. Poly-Silicon Nitride Layer Thickness

Left Line ◇
Central Line +

Linewidth (microns)

Thickness of Nitride Layer (microns)

0.0 micron defocus
Top Layer: 1.0 micron KTI-895i resist: n = 1.81, A = 0.52, B = 0.081
Middle Layer: Poly-Silicon Nitride: n = (1.948, 0.0)
Bottom Layer: 25 nm Silicon dioxide: n = (1.474, 0.0)
Substrate: Silicon: n = (6.551, 2.648)

Linewidth of Nominal 0.7 micron Lines vs. Poly-Silicon Nitride Layer Thickness

Left Line $\diamond$

Central Line $+$

-0.8 micron defocus
Top Layer: 1.0 micron KTI-895i resist: n = 1.81, A = 0.52, B = 0.081
Middle Layer: Poly-Silicon Nitride: n = (1.948, 0.0)
Bottom Layer: 25 nm Silicon dioxide: n = (1.474, 0.0)
Substrate: Silicon: n = (6.551, 2.648)

Thickness of Nitride Layer (microns)

Linewidth (microns)

Linewidth of Nominal 0.5 micron Lines vs. Poly-Silicon Nitride Layer Thickness

Left Line ◇
Central Line +

0.0 micron defocus
Top Layer: 1.0 micron KTI-895i resist: n = 1.81, A = 0.52, B = 0.081
Middle Layer: Poly-Silicon Nitride: n = (1.948, 0.0)
Bottom Layer: 25 nm Silicon dioxide: n = (1.474, 0.0)
Substrate: Silicon: n = (6.551, 2.648)

Thickness of Nitride Layer (microns)

Linewidth (microns)

Linewidth of Nominal 0.5 micron Lines vs. Poly-Silicon Nitride Layer Thickness

Left Line ◇
Central Line +

-0.8 micron defocus
Top Layer: 1.0 micron KTI-895i resist: n = 1.81, A = 0.52, B = 0.081
Middle Layer: Poly-Silicon Nitride: n = (1.948, 0.0)
Bottom Layer: 25 nm Silicon dioxide: n = (1.474, 0.0)
Substrate: Silicon: n = (6.551, 2.648)

Thickness of Nitride Layer (microns)

Linewidth (microns)

.180 nitride .7 mic lines

.145 mic nitride .7 lines
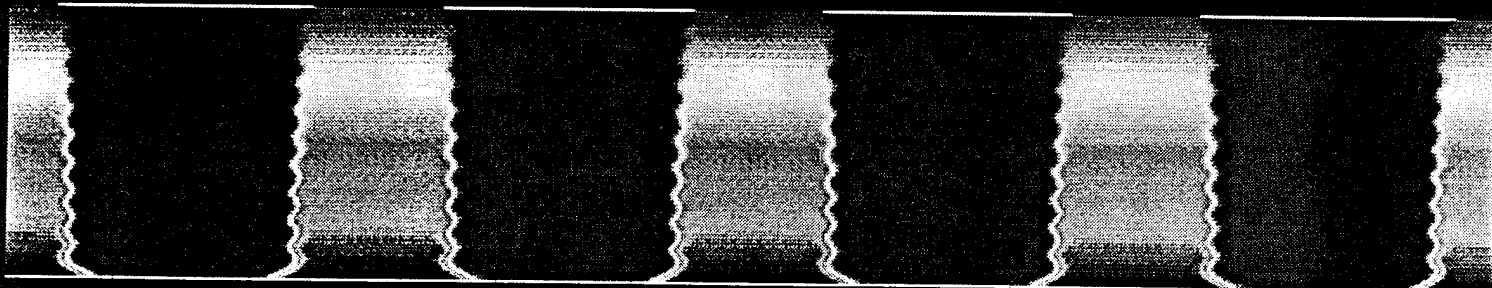
.115 mic nitride .7mic lines
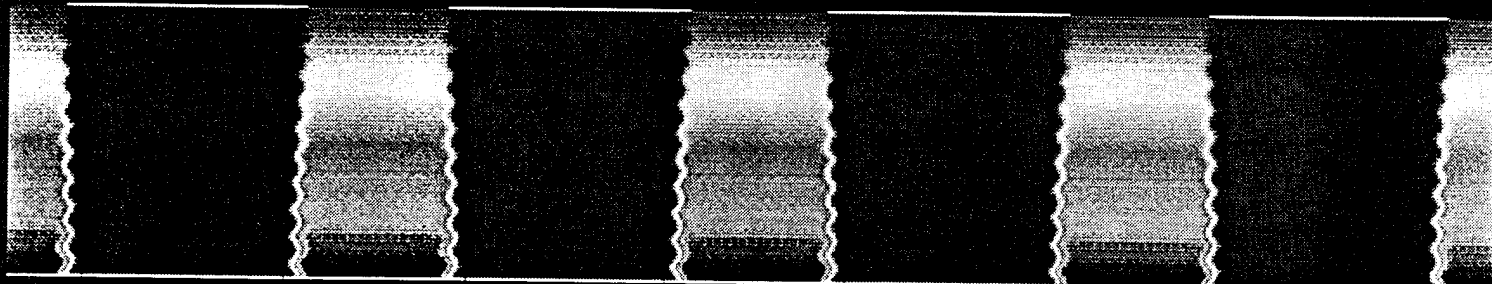
Defocus Asymmetry

+1 micron defocus: exposure

post-exposure bake
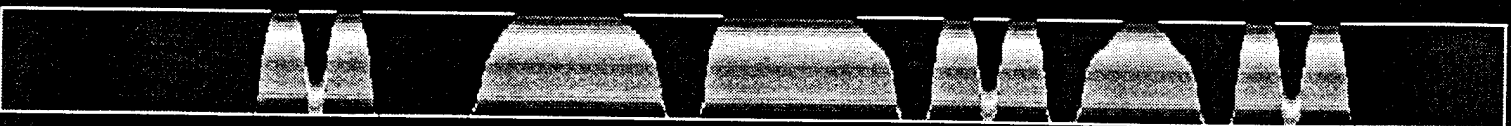

dissolution

−1 micron defocus: exposure

post-exposure bake
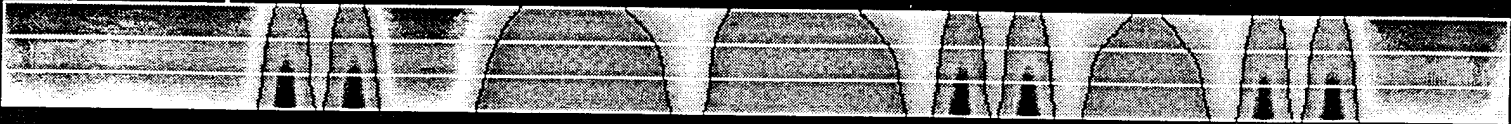
dissolution

Defocus Asymmetry Study: Dissolution
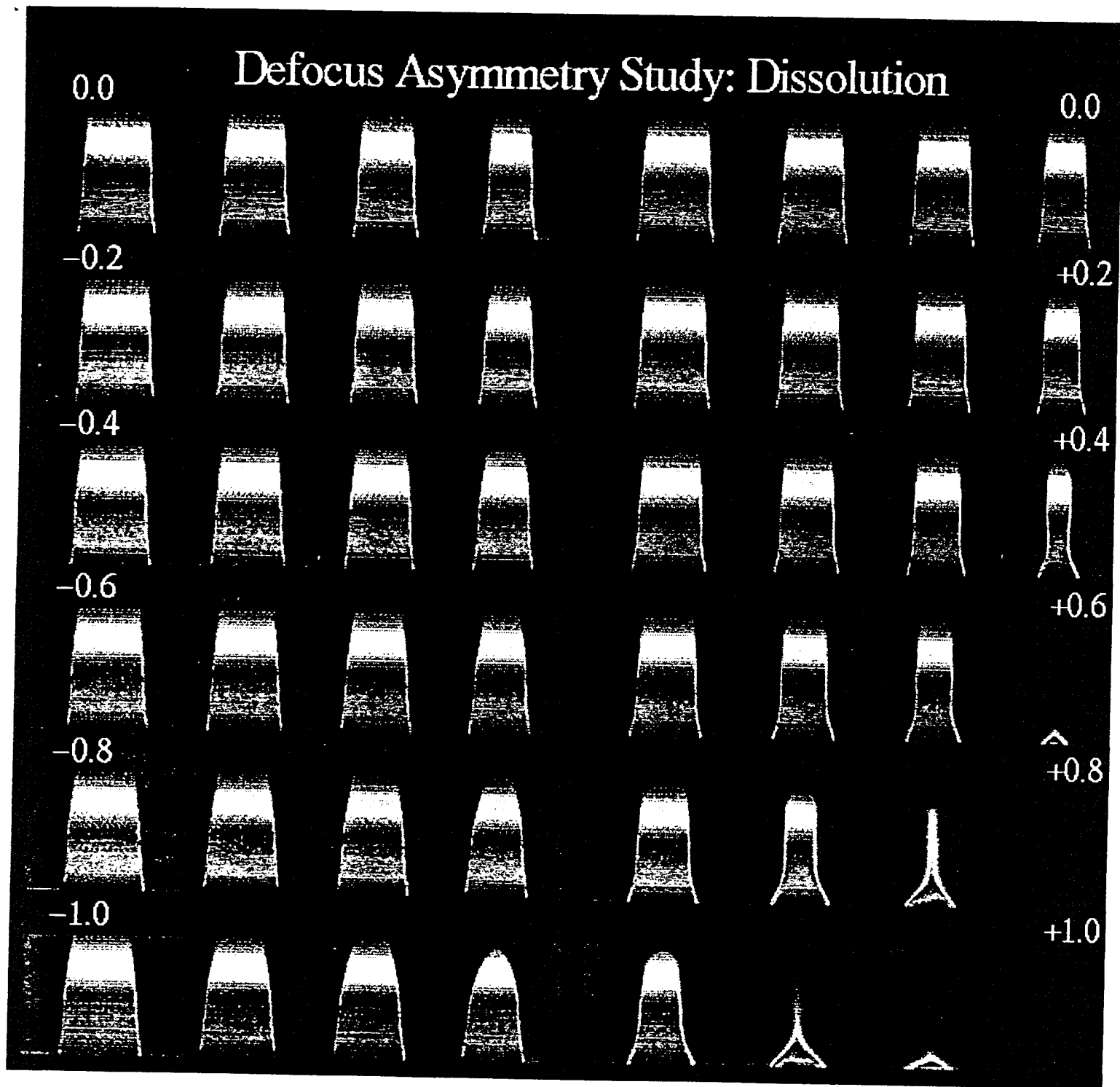
Isolated 0.35-micron Line in Apex-E Resist, Using 3D-FAIM
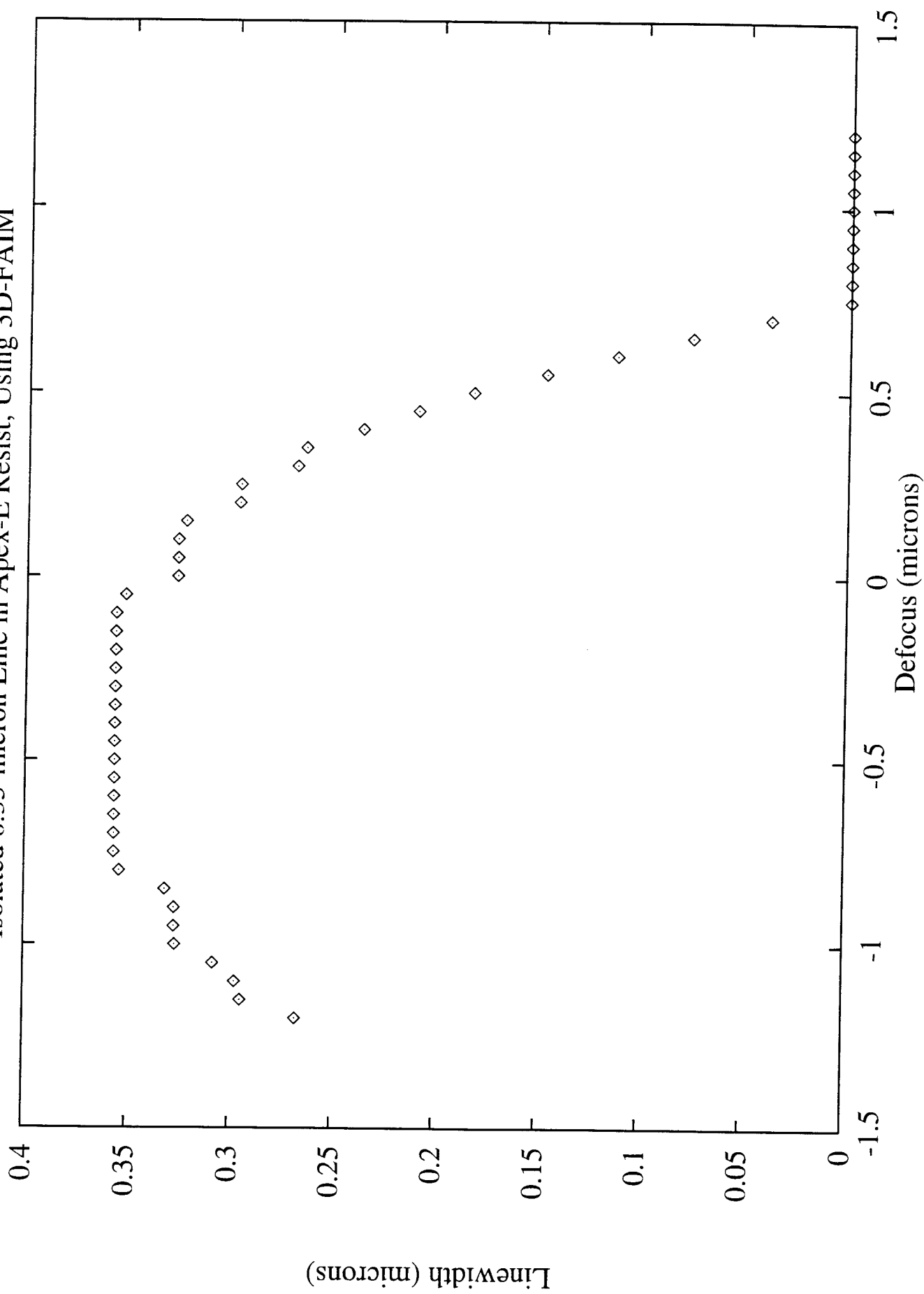
Focus Latitude for Apex-E Resist

Nominal Linewidth 0.35 micron
Exposure 12-16 mJ/cm^2

Defocus (microns)

Linewidth (microns)
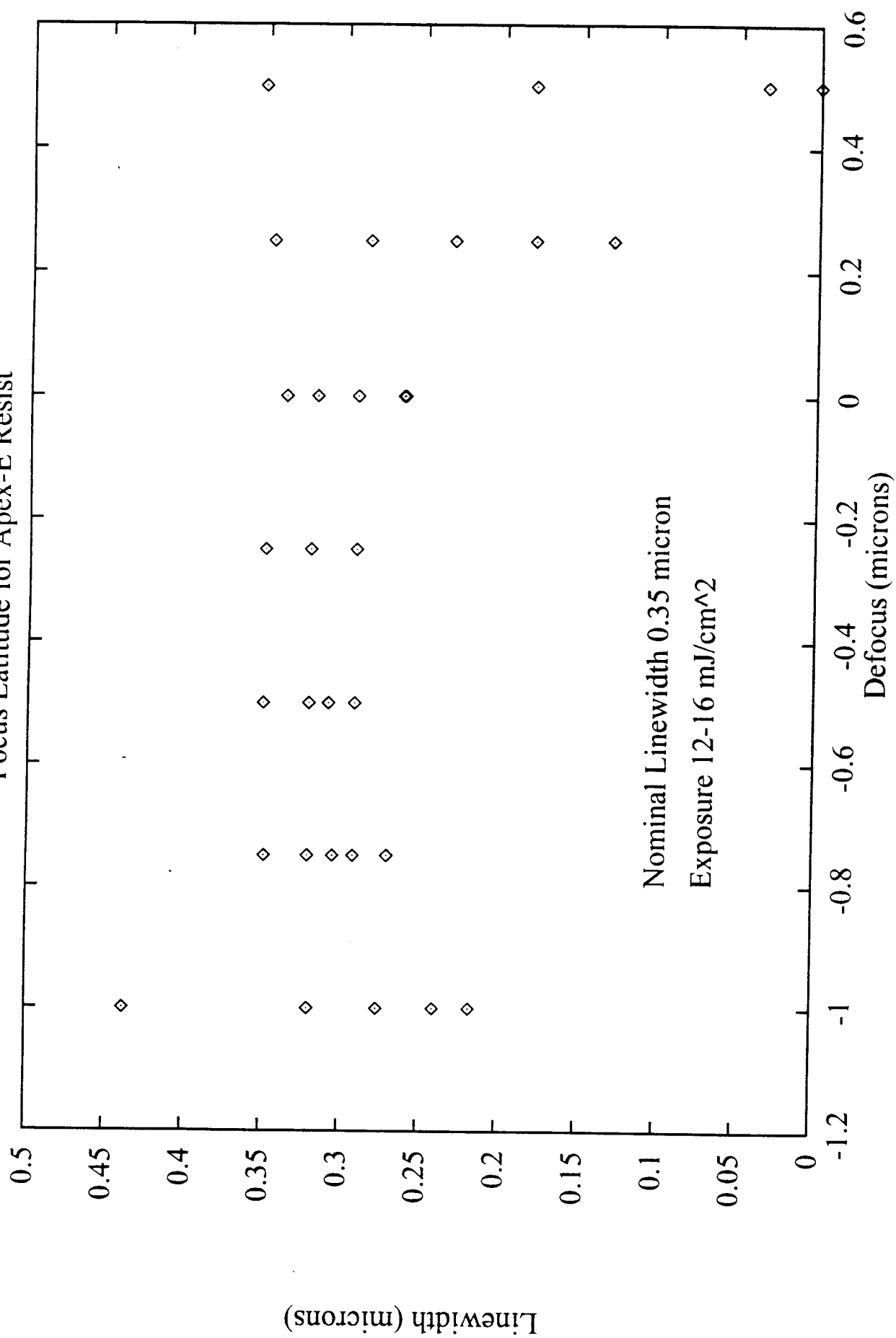
Apex-E Resist over Poly-Silicon: 14-16 mJ/cm^2

Linewidth (microns)

Defocus (microns)
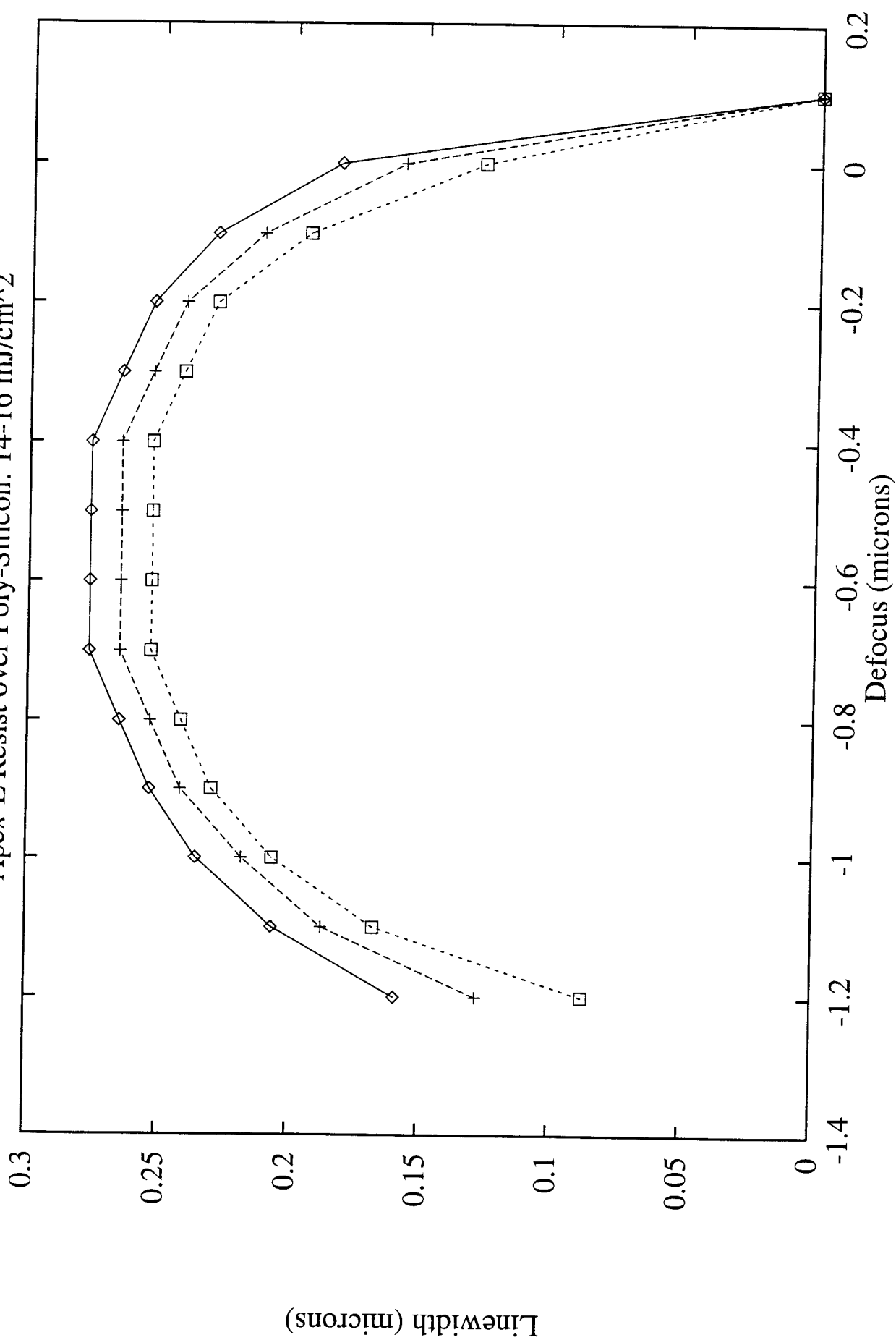
Large area optical design rule checker for Logic PSM application

John L. Nistler, Chris Spence

Advanced Micro Devices, 901 Thompson Place, Sunnyvale, CA, USA.

Eytan Barouch, Uwe Hollebach

Program in Applied and Computational Mathematics, Princeton University, Princeton, NJ, USA.

ABSTRACT

An aerial optical design rule checker (ODRC) that will handle large areas is used to validate the automatic CAD software used for application of alternating Phase Shift Mask technology to logic devices. An automatic alternating aperture layout algorithm (AutoALT) developed internally by Advanced Micro Devices is applied to 0.24 to 0.50 um electrical designs. The layout is then verified for different stepper and defocus values by the ODRC which utilizes the simulated aerial image to compare directly to the electrical design database. Entire databases are handled by fracturing the database into optically isolated areas or by using a sliding window technique. Small areas up to 420 um per side can be done with single processor workstations with at least 512 megabyte of memory. Larger problems require multiprocessor computers with at least 16 gigabyte of memory. Full circuit analysis should be done on systems with at least 64 gigabyte of memory in order to accomplish solving the problem in a reasonable time frame.

INTRODUCTION

The cost of building the new Megafabs has placed a greater emphasis on producing integrated circuits at smaller geometries, lower cost with shorter learning curves and reduced cycle time for introducing new product to market. Phase shift mask technology has been demonstrated, theoretically[1] and experimentally[2] to increase the exposure and focus latitude at small k1 values. This is considered especially useful in reducing operating costs because known production technologies such as I-line can be used. Alternating PSM is seen as especially useful because of the wide range of k_1 applicability, $0.3 < k_1 < 0.7$, in the Rayleigh equation. Alternating PSM is therefore also applicable to larger geometries where the increase in focus and exposure latitude would lead to reduced costs by extending stepper and process life while reducing reworks and scrap rates.

The greatest difficulties in applying PSM technology is in the areas of design and reticle manufacturing[3]. Automatic application of Alternating PSM has been found to be especially difficult for VLSI and ULSI logic gate layouts. Alternative PSM approaches such as attenuated or rim masks and various illumination schemes such as quadropole or annular illumination have been researched because of the perceived reduced design complexity. Application to real integrated circuits has shown various significant problems that have to be addressed with these approaches.

Attenuated PSM requires a coating with uniform transmission and phase across the entire plate. In addition, if the alignment system of the stepper being utilized is at a different wavelength than the exposure wavelength, either the coating matierial's transmisstivity across multiple wavelengths must be relatively flat or other techniques need to be applied. In addition, whereas printability of small features are enhanced, larger features are actually degraded due to the first order diffraction signal having too much intensity. (This is commonly known in the industry as sideloab printing.) Therefore special optical proximity or assist features are required on large contacts, $k_1>1.0$, and on poly resistors or poly and metal contact pads. Preferential biassing based on feature size and other feature proximity is also required for the gate and wiring levels. Rim shifted PSM and normal chrome masks require OPC, optical proximity correction, and feature dependent biasing to improve manufacturing capability. In addition, Rim PSM requires extremely tight C.D. control on small features during the reticle manufacturing. The authors have found that attenuated masks are useful at the contact level where contact dimensions with k1 between $0.5<k_1<0.7$ can be significantly enhanced. But, zero E-field two dimensional gratings had to be used in the scribe line and alignment mark area to reduce background transmission.

Modified illumination is not new. Anyone who has ever used a dark field, polarized, or contrast enhanced microscope has utilized modified illumination. The difference between microscopy and steppers is that while placing an aperture after the uniformer in a microscope does not affect the qualitative results it can affect the light uniformity and lens' distortion significantly on a stepper. Internal evaluations of two commercially available steppers with quadropole illumination verified that center of curvature degradation was the most significant distortion increase seen.[4]

Thus, independent of the type of approach decided on, a significant amount of work is required. The work will be required either in I.C. design, stepper modification, or reticle manufacturing and materials. The authors have chosen the alternating PSM for gate and wiring applications due to its linewidth linearity, general design rule applicability, significant increases in poly gate linewidth control, defect free printability[3] and the extension of the technique to multiple

stepper and linewidth conditions independent of wavelength.

The authors have developed in conjunction with others at Advanced Micro Devices an automatic way of applying alternating PSM to logic devices. An optical design rule checker, ODRC, is used to verify the aerial image performance through focus on critical dimension and contrast control.

TEST RESULTS

Software tests including CPU time and memory usage were done in evaluating the applicability of the AutoALT and ODRC software to full circuit application. AutoALT was able to convert a microprocessor design to an alternating multiphase PSM design in approximately 8 to 12 hours per level converted. The present failure rate of automation is 1 to 5 ppm. The primary areas of difficulty is due to phase conflicts at poly tees and H layouts. AutoALT identifies all incorrect phase assignments, and the ODRC identifies problem areas that would fail when printing on the wafer. The ODRC is first used at zero focus to immediately identify obvious layout problem areas. These areas are then corrected either manually or by using the optimization code. The ODRC is then repeated at zero and plus or minus preset defocus values to verify that the design is corrected to maintain C.D. and aerial image contrast within specifications. The optical boundary conditions associated with C.D. control, contrast and focus should be fully understood prior to the optimization being exercised. Otherwise excessive iterations or divergence of the optimization algorithms can occur due to the physics of the problem.

The longest CPU time required is to compute the aerial image which must be done at a minimum of three focus values for robustness of design. The greatest amount of memory required is for the ODRC since the first partial differentials of the intensity with respect to X and Y have to be calculated to inspect for image contrast. Thus three two-dimensional large matrices are required for the ODRC. Two gigabyte of memory per processor is required to address reasonably sized segments of the design. (The minimum area that is dealt with on full design check is 400 um per side.) A single aerial image calculation for a 60 by 80 um area takes 20.54 minutes on a 50 MHz single pipe microprocessor system and 4.52 minutes on a 66 MHz dual pipe microprocessor system. Aerial image calculations for 2048 um per side take approximately 12 hours on the IBM-PVS parallel processor computer and 3.5 hours on the IBM-SP1 parallel processor computer. Present work on the IBM-SP2 system is on going. Initial analysis indicates that a full microprocessor design takes 16 hours to calculate the aerial image using a 32 processor system. The ODRC requires approximately three hours. It thus takes 57 hours per iteration. The optimization code takes 3 to 4 iterations for $0.5<k1<0.7$, and it is estimated that up to 10 iterations will be necessary for $k1<0.4$. Significant work is still required to bring the 228 hours under the 168 hour

(7 day/24 hr per day) goal.

Figure 1 labeled Bacus shows the polygon layout for a 240 by 240 um section from a 0.35 um logic device. The failures at zero and 0.4 um defocus are shown in figures 2 and 3 for a normal chrome mask using an ASML 5500/60 stepper with a N.A. of 0.54 and a sigma of 0.48. Note that the normal chrome mask starts to immediately fail at zero defocus and it fails strongly at 0.4 um defocus. The alternating PSM failures are not nearly as significant, a smaller area (figure 4 will be used to highlight the type of errors seen in the design. Figure 5 highlights the immediate failures that occur for a normal chrome mask at 0.0 um defocus for the 0.54 N.A. and 0.48 sigma stepper. Figures 6 and 7 illustrate the alternating PSM design failures utilizing the same stepper conditions as figure 5. Note that the predominant failures occur at chrome tees, elbows and at the ends of long lines. This is primarily due to phase transition boundary conditions.

It appears that the 180 degree phase region is the largest contributor to localized linewidth errors. Global linewidth errors were corrected by the chrome pattern. Line shortening is affected predominantly by the chrome , 120 degree phase and 60 degree phase regions. The reason that C.D. error by itself is not sufficient as an ODRC criteria is due to the fact that a single threshold is used to represent the transferable critical dimension to the photoresist. If the contrast is not included in the ODRC analysis the critical dimension criteria could be passed even though the image contrast is terrible.

The ASML 5500/100 allows discrete values of N.A. and sigma to be varied on the stepper. Initial analysis using the highest N.A. and lowest sigma, 0.60 N.A. and 0.32 sigma, indicate that no process at 0.24 um is available for a normal chrome mask. (Figure 8) The application of the alternating PSM would improve the performance significantly. (Figures 9 and 10)

SUMMARY

Software has been developed which automatically assign alternating PSM to logic designs. Design rule validation is verified by an existing polygon check program in existing CAD tools and by verifying the actual aerial image performance on the wafer using an optical design rule check software program. The software has been applied to logic circuit designs allowing significant improvement in the performance of the electrical designs at 0.36 and 0.24 um geometries. Future work will include the refinement of the software with extensive verification on wafer and further computational evaluation of CPU and memory requirements.

ACKNOWLEDGEMENTS

REFERENCES

1) D. Cole, E. Barouch, U. Hollerbach, and S, Orszag. "Derivation and simulation of higher numerical aperture scalar aerial images," Jap. J. Appl. Phys. Vol. 31 p. 4110 (1992).

2) M.D. Levenson, N.S. Viswanathan, R.A. Simpson. "Improving resolution in photolithography with a phase-shifting mask," IEEE Trans. on Electron Devices, Vol. 29, Ed. No. 12, p. 1812, (1982)

3) J. Nistler, G. Hughes, A. Muray and J. Wiley. " Issues associated with the commercilaization of phase shift masks," SPIE Vol. 1604, p. 236 (1991).

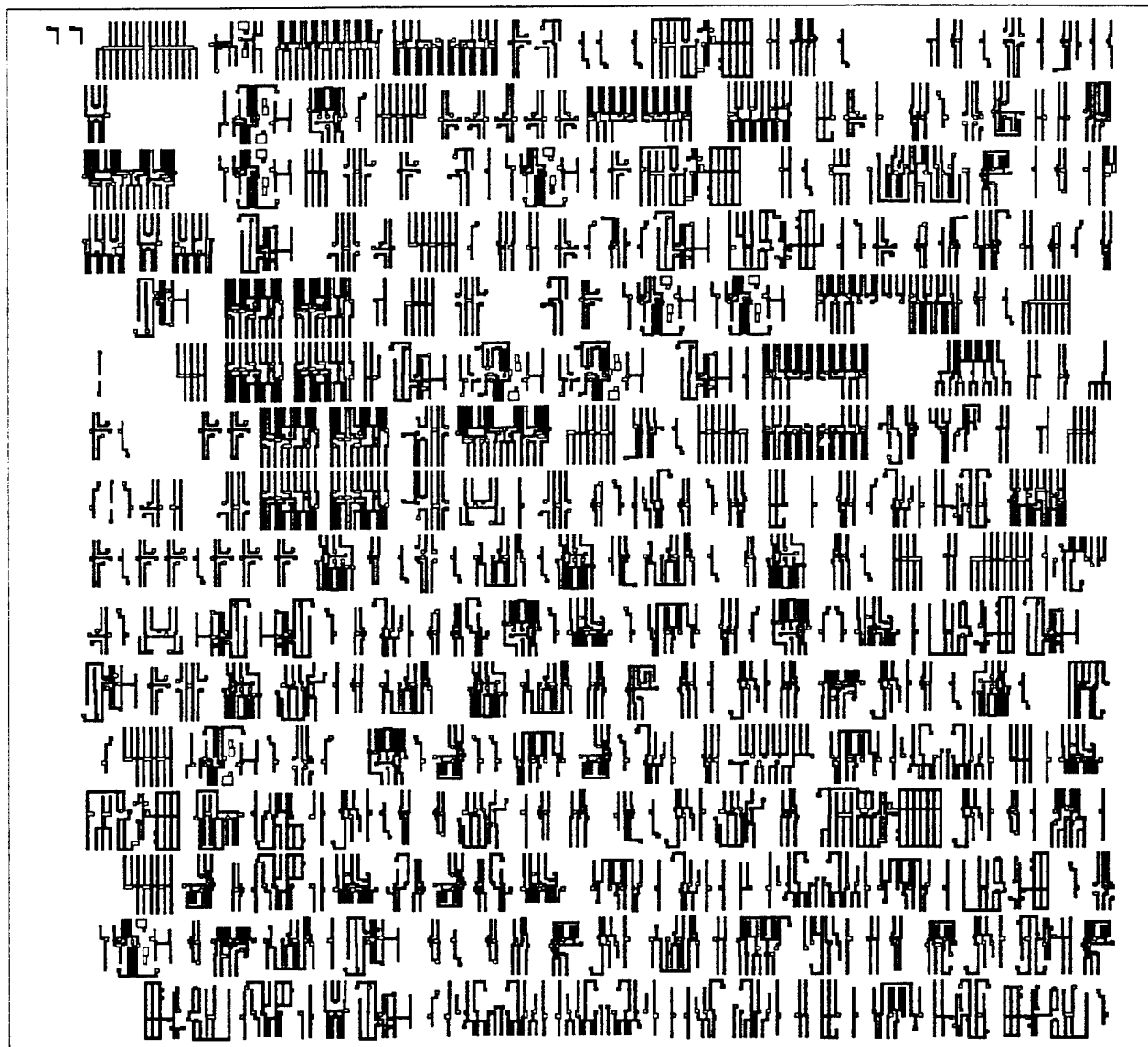4) R. Edwards, P. Ackmann. "Stepper evaluation results," Internal AMD report, (1994).

bacus_cr.faim
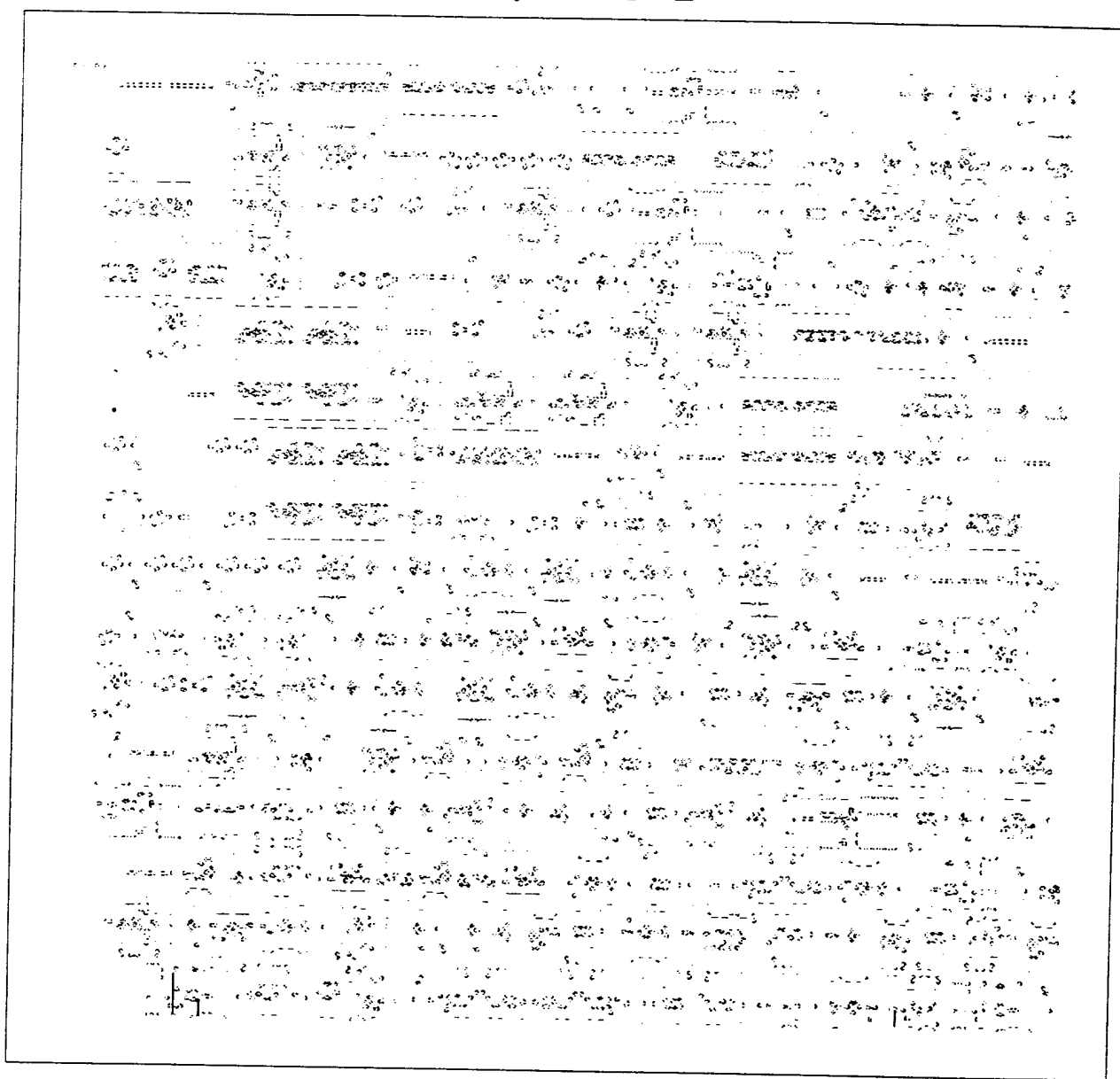

Figure 1- Normal chrome layout.

0.3intensity_0def_2x_refined

Figure 2 - Results of chrome mask at 0.0 um defocus. C.D. control
criteria of +/- 0.04 um. N.A. of 0.54 and sigma of 0.48.

0.3intensity_0.4def_2x_refined

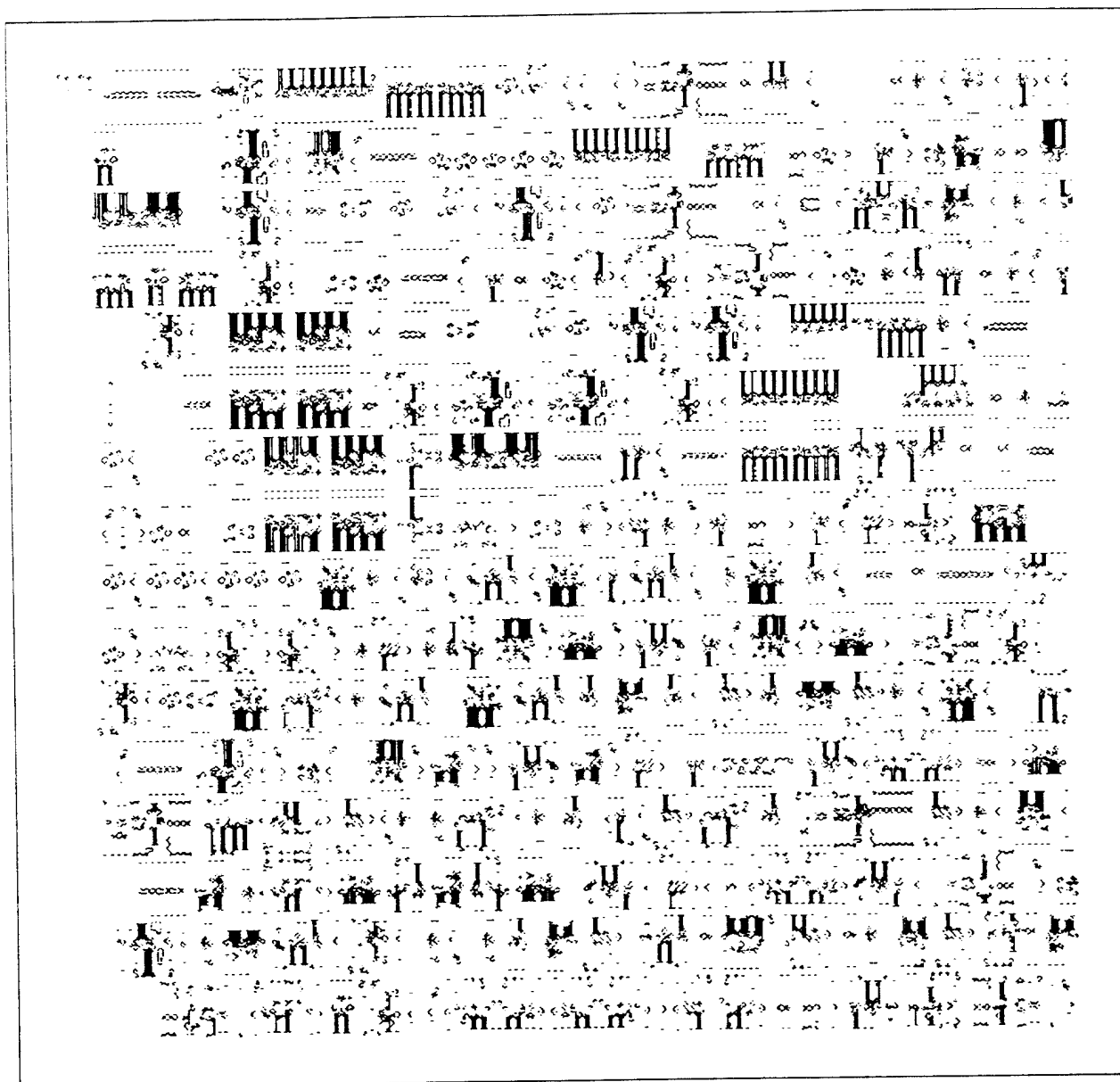Figure 3 - Results of chrome mask at 0.4 um defocus. C.D. control
criteria of +/- 0.04 um. N.A. of 0.54 and sigma of 0.48.
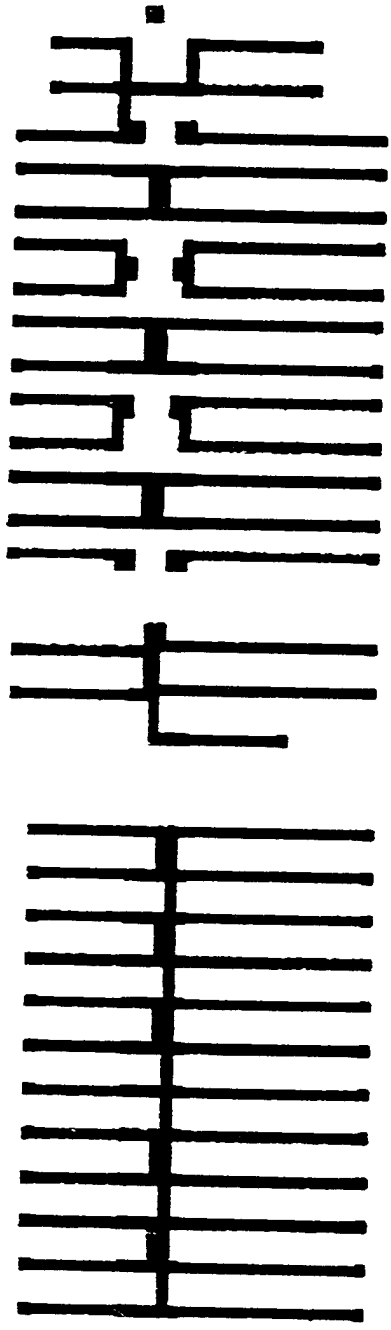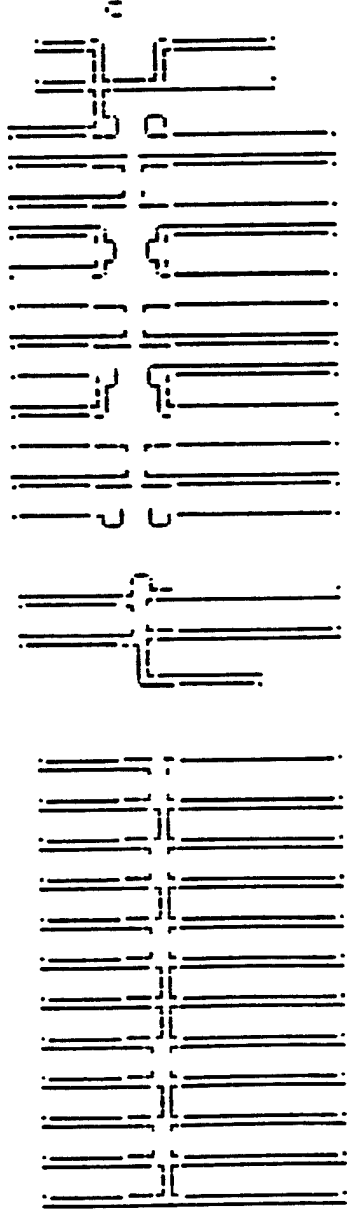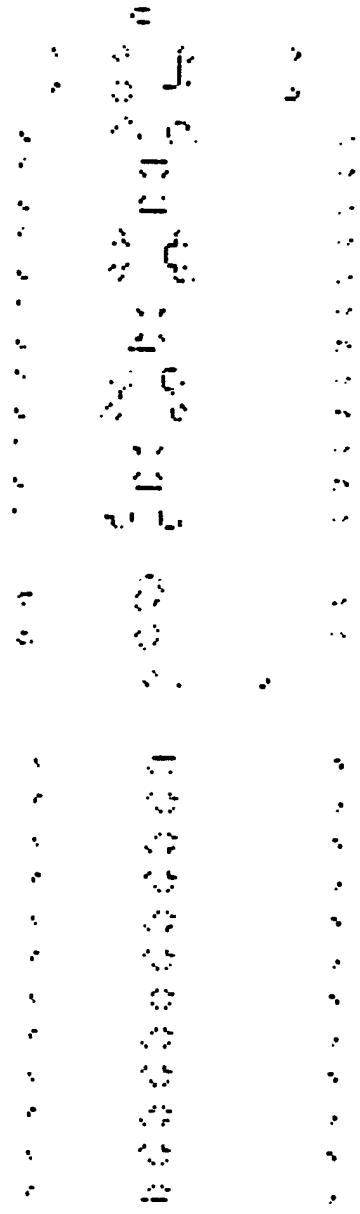
Brewster@0.25um

Figure 4.

Figure 5.

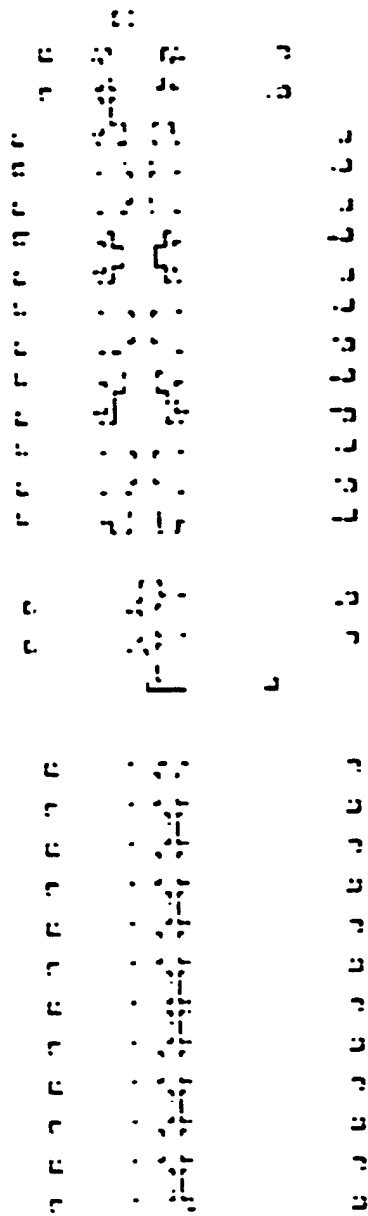Aerial Image Optical DRC failures for a normal chrome mask;

N.A. = 0.54, sigma = 0.48, linewidth = 0.36 um Defocus = 0.0 um

Figure 6.

Aerial Image Optical DRC failures for an alternating PSM mask; N.A. = 0.54, sigma = 0.48, linewidth = 0.36 um, defocus = 0.0 um.
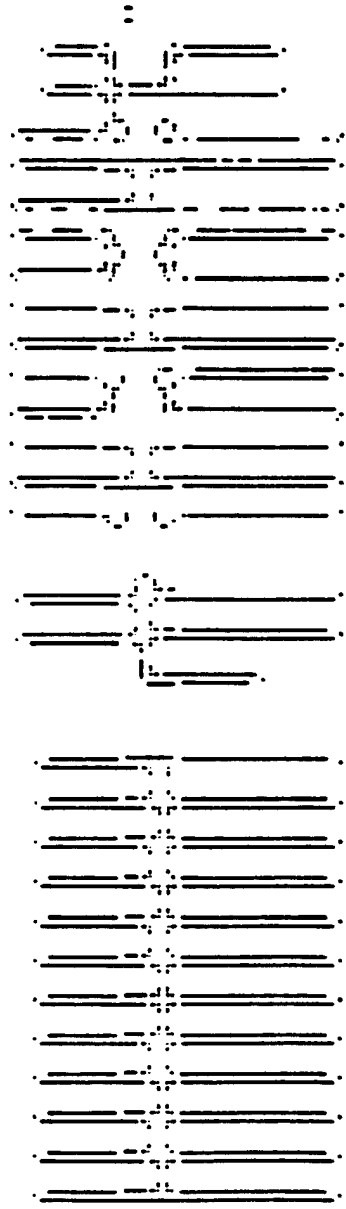
Figure 7.

Aerial Image Optical DRC failures for an alternating PSM mask;

N.A. = 0.54, sigma = 0.48, linewidth = 0.36 um, defocus = 0.4 um.

Figure 8.

Aerial Image Optical DRC failures for a normal chrome mask;

N.A. = 0.60, sigma = 0.32, linewidth = 0.24 um, defocus = 0.0 um.

Figure 9.

Aerial Image Optical DRC failures for an alternating PSM mask;

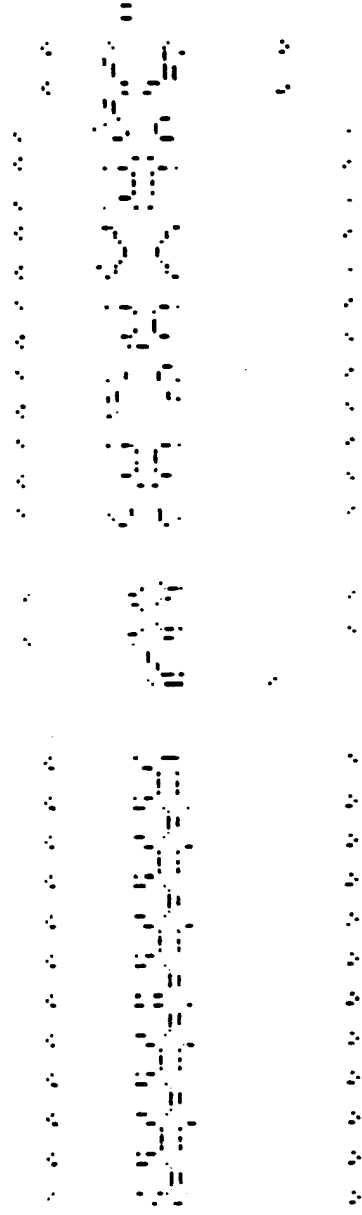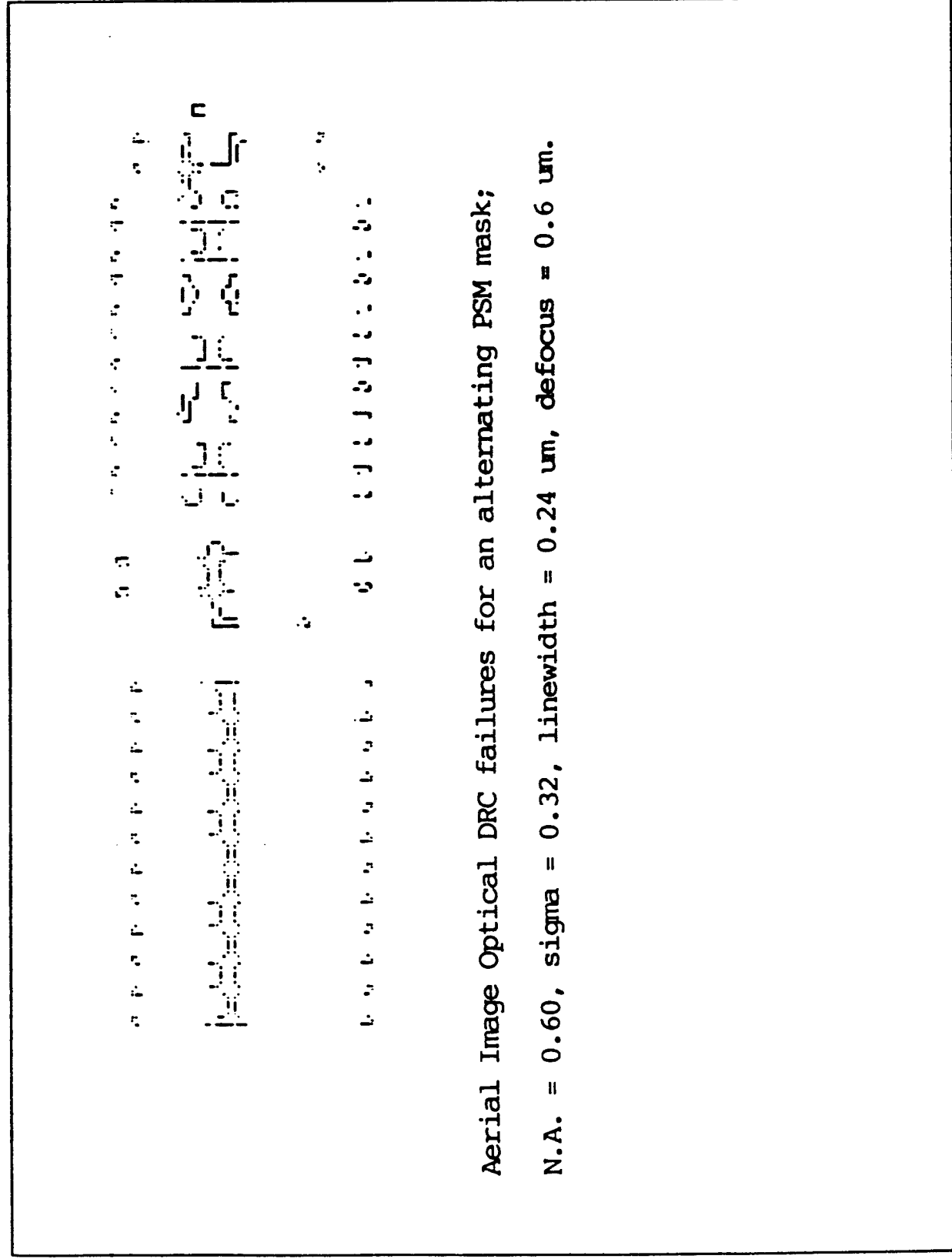N.A. = 0.60, sigma = 0.32, linewidth = 0.24 um, defocus = 0.0 um.

Figure 10.

Aerial Image Optical DRC failures for an alternating PSM mask;

N.A. = 0.60, sigma = 0.32, linewidth = 0.24 um, defocus = 0.6 um.

Evaluation of depth-of-focus in photolithography at 193 and 248 nm for feature sizes of 0.25 μm and below

M. Rothschild and S. P. Doran
Lincoln Laboratory, Massachusetts Institute of Technology, Lexington, Massachusetts 02173-9108

E. Barouch, U. Hollerbach, and S. A. Orszag
Program of Applied and Computational Mathematics, Princeton University, Princeton, New Jersey 08544

The aerial image of alternative exposure systems was calculated in order to determine process latitude in photolithography at 0.25 μm and below. A fast software package was used for both simple and complex mask patterns. The depth-of-focus (DOF) was obtained with the aid of exposure–defocus plots at 193 and 248 nm. The numerical aperture and degree of spatial coherence were varied over a wide range. The effects of annular illumination were also studied. It was shown that for most geometries the DOF at 193 nm exceeds that of 248-nm systems. Only for equal lines and spaces does a 248-nm tool with annular illumination possess a DOF comparable to that of a conventionally illuminated 193-nm system.

I. INTRODUCTION

The continuing reduction in depth-of-focus (DOF) which accompanies the reduction of minimum feature size is arguably the single most important issue in photolithography. The two rules of thumb used to express the minimum linewidth (LW) and DOF in terms of the actinic wavelength λ and the numerical aperture (NA) of the imaging optics have been $LW = k_1\lambda/NA$ and $DOF = \pm k_2\lambda/(NA)^2$. In these expressions, k_1 and k_2 are process parameters, independent of λ and NA. From basic principles, k_1 must be greater than 0.25 (in practice it is ~0.5–0.8), but there are no fundamental limitations on the value of k_2. The expression $DOF = \pm 0.5\lambda/(NA)^2$, referred to as the Rayleigh DOF, is frequently used for quick estimates.

The above expression for LW indicates that the path to higher resolution involves a shift to smaller wavelengths and/or an increase in NA. Both alternatives lead to a reduction in DOF. However, because of the different functional dependences on λ and NA, the penalty of reduced DOF is smaller if the wavelength is reduced than if the NA is increased. These simple considerations have been the driving force behind the shift from g line (436 nm) to i line (365 nm) as the LW shrunk to below ~0.7 μm. A similar trend is widely expected to take place in the future when deep-UV (248 nm) systems will gradually replace i-line steppers at LWs below ~0.4 μm, and 193-nm optics will get their turn below ~0.25 μm. However, recent developments in stepper technology may slow the rate of transition to shorter wavelengths. Phase-shifting masks, off-axis illumination (annular, quadrupole, ...), and pupil apodization are actively being explored as means to retain relatively large DOF while increasing the NA at a fixed λ. The trade-offs between changing the wavelength and changing reticle and illumination technologies involve practical as well as fundamental considerations. The decision making process to choose between the two approaches would first require the assessment of the respective potential benefits, then to be followed by an analysis of the difficulties involved in

implementation. The most important component in the first step is the optimization of the DOF of the aerial image. The rule of thumb mentioned above is insufficient for this purpose, for several reasons. First, it does not take into account the degree of spatial coherence of the illumination optics. Second, it does not provide information on the exposure latitude. Finally, it disregards the effects of feature type and proximity effects in the complex patterns of realistic circuits.

In this article, we present results of modeling the aerial image of alternative exposure tools designed for 0.25- and 0.18-μm geometries. (These dimensions correspond to 256 Mbit and 1 Gbit dynamic random access memory chips, respectively, which are expected to go into production in the years 1998 and 2002, respectively.) In particular, the relative advantages of 248 and 193 nm, with and without off-axis illumination are being explored. We employ a fast computer program which calculates the aerial image of complex patterns from first principles, and evaluate the DOF under a range of imaging alternatives.

II. RESULTS AND DISCUSSION

The software employed in this study was described in detail elsewhere.[1] Briefly, it starts from Maxwell's equations, and with the judicious choice of algorithms it avoids any kind of approximation while calculating the aerial image. It can use either the scalar or vector representation of the electric field. The effect of aberrations can be calculated by introducing Zernike polynomials, although in our study we assumed diffraction-limited performance throughout. Its most remarkable feature, however, is its speed. The aerial image of complex masks as large as a full functional cell can be calculated on a state-of-the-art workstation within less than 15 min. Furthermore, the time required to calculate the aerial image increases only linearly with the area, rather than the quadratic dependence used in other algorithms. Thus, the performance of exposure tools with realistic mask levels can be evaluated within short periods of time. Examples are shown in Fig. 1. Here, the aerial
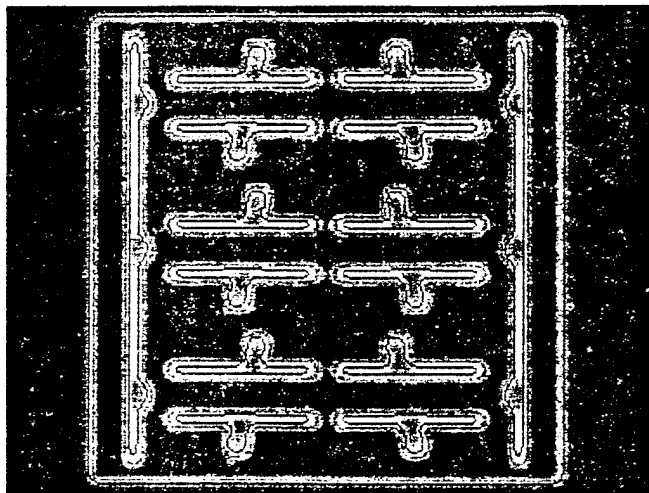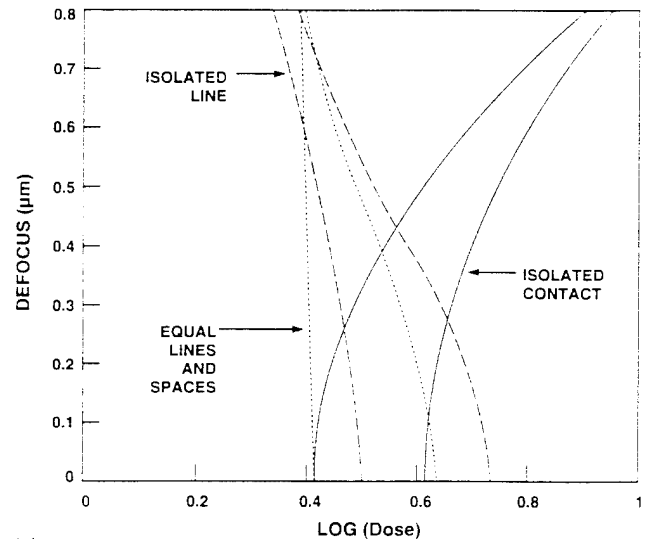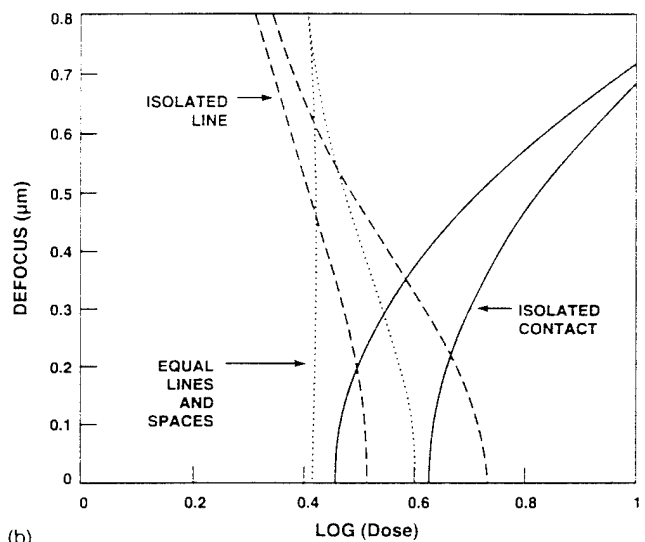
(a)
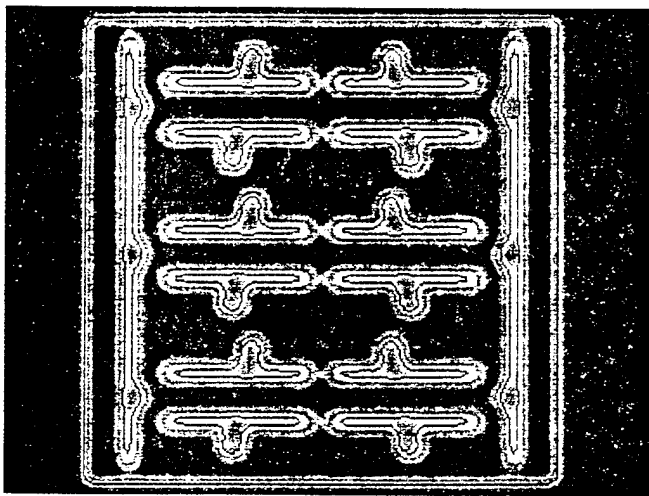
(b)

FIG. 1. Top view of the aerial image of a static random access memory gate cell array. The design is similar to that in Ref. 2. except for the scaling, so that the smallest features are 0.18 μm. A defocus of 0.5 μm was used. (a) Exposure at 193 nm, with 0.5 NA and σ=0.6. (b) Exposure at 248 nm with 0.5 NA and σ=0.6. The contours correspond to a normalized intensity of 0.3 (where the open-field intensity is 1.0). Note that in (b) there is significant pinching-off of the thin long lines, as well as bulging of these lines opposite designed protrusions.

(a)

(b)

FIG. 2. ED plots of the aerial image of equal lines and spaces, an isolated line, and an isolated contact hole, all of nominal 0.25-μm dimension. The usable ED parameter space for each feature type is enclosed between the x axis and the corresponding two lines. A ±10% linewidth control was used throughout. (a) Exposure at 193 nm, with 0.5 NA and σ=0.6. (b) Exposure at 248, with 0.65 NA and σ=0.6.

image of the gate level of three adjacent cells of a static random access memory chip is shown.[2] The smallest nominal dimension is 0.18 μm. Figure 1(a) models the aerial image at 0.5-μm defocus, obtained with the 193-nm step-and-scan system being constructed by SVG Lithography under a subcontract to Lincoln Laboratory (4× reduction, 0.50 NA, spatial coherence factor σ=0.6). Figure 1(b) shows the aerial image obtained with the Micrascan II (same parameters, except λ=248 nm). Close inspection reveals that the image fidelity is retained to a significantly larger degree at 193 than at 248 nm. In particular, the defocus of 0.50 μm is larger than the Rayleigh DOF of the 193 nm system (±0.39 μm), and is equal to that of the 248-nm system. Nevertheless, the larger k_1 value at 193 nm (0.47) than that at 248 nm (0.36) plays a more significant role in controlling the aerial image. Figure 1 goes beyond the rules confirming the significance of k_1, however. It also

shows the extent of the deterioration in image quality, such as shortening of long lines and rounding of corners.

A simpler set of features was used in order to enable more quantifiable results of the simulation. Specifically, we simulated the aerial image of 3-μm-long equal lines and spaces, a 3-μm-long isolated line, and an isolated contact hole. Then the intensity distribution across the center of each feature was calculated. All features were 0.25 μm wide. It should be noted that at these dimensions, which are close to the wavelength, an isolated contact hole behaves quite differently from an isolated space. Using the one-dimensional intensity profile across the center of each type of structure we constructed exposure–defocus (ED) plots.[3] Figure 2 shows examples of ED plots obtained with a ±10% allowed variation on the 0.25-μm feature size and with an exposure threshold of 0.3 relative to open field

exposure. Figure 2(a) represents the 193-nm Micrascan, while in Fig. 2(b) a 248-nm, 0.65-NA hypothetical Micrascan was used. The value of 0.65 in the latter was chosen so as to keep the same k_1 factor as that of the 193-nm tool, and therefore the exposure latitudes at zero defocus are nearly the same for both systems. However, the 248-nm, high-NA Micrascan clearly has a lower DOF, as illustrated in the more rapidly bending and more quickly narrowing ED plots. This result is in qualitative agreement with the Rayleigh expression, but it reveals further information about the exposure latitude, and how it impacts on DOF.

Since maximizing the DOF is our main concern in this study, we further reduced the ED plots, as follows: We imposed an exposure latitude of $\pm 10\%$, without specifying the mean value. The value of the mean dose was selected with reference to the specific ED plot (and therefore could be different for the different feature types), in such a way as to maximize the allowable defocus value. In what follows we refer to twice the defocus value thus obtained as the DOF. (The factor of 2 is introduced in order to account for allowable defocusing in both directions.) It should be noted, however, that this definition of DOF, namely, within the constraints of $\pm 10\%$ linewidth control and $\pm 10\%$ exposure dose, is quite different from the DOF in the Introduction, which does not allow for exposure variation. A tighter exposure latitude (say, $\pm 1\%$) could of course also be used, the result being larger DOFs. In general, the focus latitude and exposure latitude may be traded off with respect to each other. While a tighter exposure latitude increases the DOF, the qualitative trends presented below do not change significantly with different exposure latitudes.

With this definition of DOF in mind, the parameters of the 248 nm exposure system were allowed to vary over a wider range. While the wavelength and the reduction ratio were kept fixed, the NA was varied in the range 0.40–0.75, the coherence factor σ was varied from 0.3 to 0.7, and annular illumination was introduced with a range of inner and outer radii. Some of the results are shown in Figs. 3–5. It is seen that the optimal values of NA and σ depend on the feature type. For instance, under conventional (circular) illumination and $\sigma=0.6$, the optimal NA for equal lines and spaces is 0.45 at 193 nm and 0.50 at 248 nm. However, for isolated contacts the dependence of DOF on NA is much less pronounced, with the optimal NA ~ 0.50 at 193 nm and ~ 0.65 at 248 nm. Equally significant is the variation of the DOF with feature type. A 193-nm, 0.5-NA system yields DOF of 1.1 and 0.80 μm for equal lines and spaces and for an isolated contact, respectively. A 248-nm, 0.65-NA system has 0.8- and 0.6-μm DOF for the same features, respectively. Furthermore, with conventional (circular) illumination the DOF of the unoptimized 193-nm system is always better than that of a 248-nm tool (except for equal lines and spaces at NA higher than 0.55). The introduction of annular illumination to the 0.5-NA 248-nm tool does increase its DOF to that of a conventionally illuminated 193-nm system, but only for the dense pattern of equal lines and spaces. In fact, annular illumi-
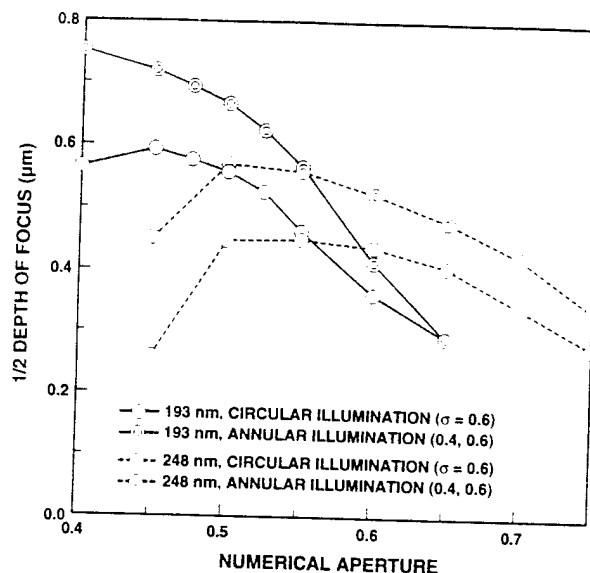

FIG. 3. Calculated DOF of the aerial image of 0.25-μm equal lines and spaces, as a function of the numerical aperture of the exposure tool. Two wavelengths are used in the simulation, 193 and 248 nm, each under two illumination conditions: circular illumination with $\sigma=0.6$, and annular illumination with the (normalized) inner and outer radii of 0.4 and 0.6, respectively.

nation has a significant negative impact on the DOF when isolated lines are to be printed (Fig. 4). This result is qualitatively understood in terms of the Fourier components of the respective patterns. In the case of equal lines and spaces the dominant components have high frequencies, and those are enhanced by the annular illumination. However, in isolated features low-frequency components contribute to the final image as well, and these are repressed by the annular illumination.

Figure 6 reaffirms these result in a visual way. Here isolated contact holes of variable size are imaged with the
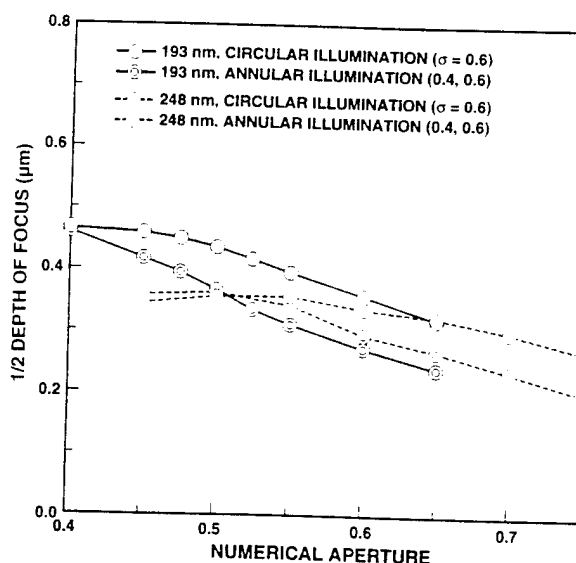

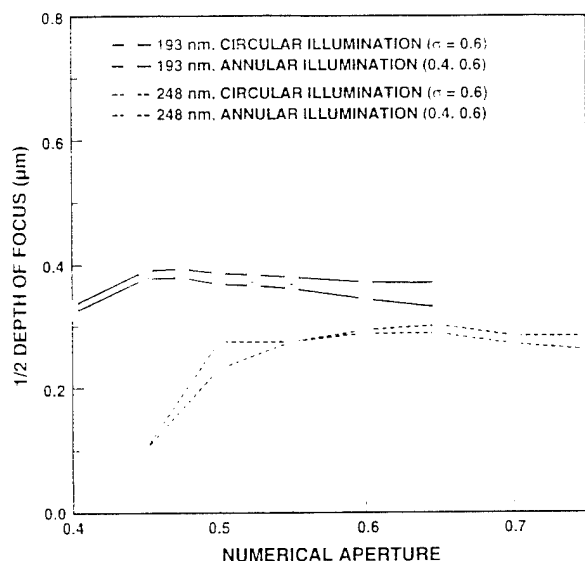FIG. 4. Calculated DOF of the aerial image of a 0.25-μm isolated line. The exposure conditions are as in Fig. 3.

FIG. 5. Calculated DOF of the aerial image of a 0.25-μm isolated contact hole. The exposure conditions are as in Fig. 3.

FIG. 7. Calculated DOF of the aerial image of 0.25-μm lines separated by spaces of varying width. The performance of two exposure systems is modeled: a 193-nm, 0.5-NA, and a 248-nm, 0.65-NA tool. In each instance two illumination geometries were used: circular ($\sigma = 0.6$), and annular with normalized inner and outer radii of 0.4 and 0.6, respectively.

193- and 248-nm systems. At a fixed defocus of 0.5 μm the best aerial image is obtained with circular illumination at 193 nm.

In practice, mask levels include features whose density covers the range from equal lines and spaces, to almost fully isolated. In Fig. 7 the spacing between 0.25-μm-wide lines was allowed to vary from 0.25 to 1.0 μm, and the corresponding DOF calculated for circular and annular illuminations, and two exposure tools: a 193-nm, 0.5-NA
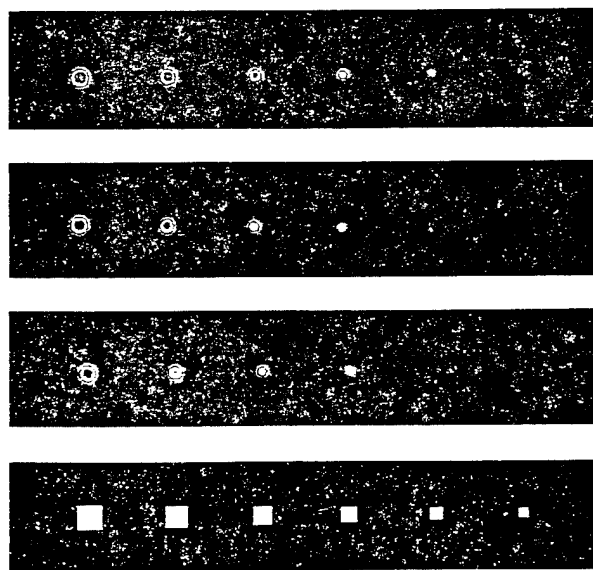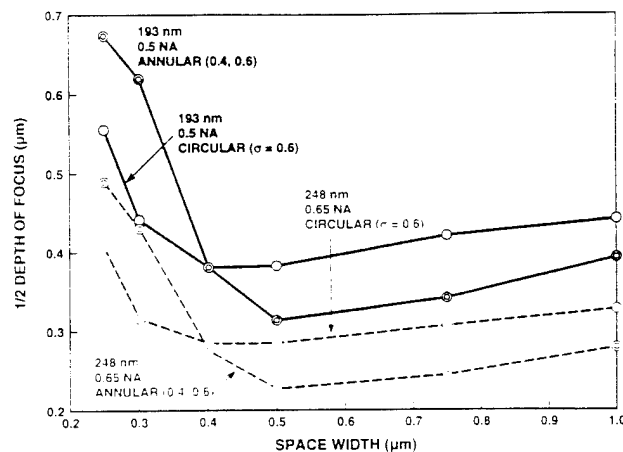

FIG. 6. The aerial image of contact holes of varying sizes, at 0.5-μm defocus, obtained with three exposure systems (from top to bottom): 193 nm, 0.5 NA, $\sigma = 0.6$; 248 nm, 0.5 NA, $\sigma = 0.6$; 248 nm, 0.5 NA, annular illumination with normalized inner and outer radii of 0.4 and 0.6; the ideal image (the reticle pattern, scaled down by 4×). The nominal hole sizes are (from left-to-right): 0.4, 0.35, 0.3, 0.25, 0.2, and 0.15 μm. Note that only the 193-nm system can print 0.25-μm contacts, and that annular illumination has little effect on the aerial image of these features.

and a 248-nm, 0.65-NA system. It is seen that the annular illumination has advantage only for a narrow range of dense geometries. Once the spacing exceeds ~ 0.4 μm, annular illumination has a detrimental effect on the DOF at both wavelengths. It is apparent from Fig. 7 that for dense patterns the DOF of a 193-nm, circular-illumination tool (~ 0.90–1.1 μm) can be achieved also with a 248-nm, annular-illumination system. However, the ~ 0.8-μm DOF of widely spaced lines at 193 nm is reduced to ~ 0.6 μm at 248 nm. In fact, k_1 in Fig. 7 is the same at both wavelengths, and the DOFs of the widely spaced features are in reasonable agreement with the $\pm \lambda / (2NA^2)$ expression discussed in the Introduction.

III. CONCLUSIONS

A fast computer simulation program was used to model the aerial image of 0.25- and 0.18-μm features obtained with exposure tools at 248 and 193 nm. The emphasis of this work has been the evaluation of the effects of defocusing on the aerial image. It was shown that, with the exception of very dense patterns (equal lines and spaces), 248-nm systems have as a rule smaller DOF than 193-nm tools. This result applies even when the 248-nm system includes optimized numerical aperture and annular illumination. In the case of 0.25-μm equal lines and spaces, a 248-nm, annular-illumination system can be optimized for a DOF comparable to that of a circularly illuminated 193-nm system. The highest DOF, 1.5 μm, was obtained for 0.25-μm equal lines and spaces using 193 nm and annular illumination. The exact values for the DOF depend to some extent on its definition; other methods to extract a DOF from the aerial image may lend somewhat different numbers. Nevertheless, the overall trend would be quite similar: in almost all instances (pattern types, illumination types), 0.25- and 0.18-μm features can be printed at 193 nm with a larger DOF than at 248 nm. The gap between the performance of 193- and 248-nm systems may be re-

duced for certain critical levels, such as contact holes, by the addition of phase-shifting masks at 248 nm. This topic is under further study.

ACKNOWLEDGMENTS

[1] D. C. Cole, E. Barouch, U. Hollerbach, and S. A. Orszag, J. Vac. Sci. Technol. B **10**, 3037 (1992); B. Kuyel, E. Barouch, U. Hollerbach, and S. A. Orszag, Proc. SPIE **1674**, 376 (1992).
[2] M. K. Templeton, E. Barouch, U. Hollerbach, and S. Orszag, Proc. SPIE, 1993 (in press).
[3] B. J. Lin, in *Microcircuit Engineering 89*, edited by H. Ahmed, J. R. A. Cleaver, G. A. C. Jones, R. A. M. McMahon, and A. N. Broers (Elsevier, New York, 1990), p. 137.

Suitability of high numerical aperture i-line steppers with oblique illumination for linewidth control in 0.35μm complex circuit patterns.

Michael K. Templeton

Advanced Micro Devices, Inc., Integrated Technology Division
Sunnyvale, CA 94086

Eytan Barouch, Uwe Hollerbach , Steven A. Orszag

Princeton University, Department of Applied and Computational Mathematics
Princeton, NJ 08544

ABSTRACT

A 2-dimensional scalar aerial image model was used to computationally study i-line imaging with oblique illumination. Limited comparisons between developed photoresist images and aerial images were made. The effects on CD control, exposure latitude, and bias, of varying annular and quadrupole geometry were mapped via simulation. Significant improvements in DOF of isolated lines was achieved with oblique illumination. Isolated line to dense line bias could be adjusted by changing the illumination type. Although oblique illumination improved the aerial image contrast at defocus, it caused degradation in the aerial image contrast at best focus. Long and short range proximity effects degraded the simulated CD control of optimized oblique illumination systems. This was observed in simulations of an SRAM gate cell. The imaging performance at .9um defocus, of an i-line system (NA .48) with oblique illumination, was judged to be worse than a KrF system (NA .42) with standard illumination. Quadrupole illumination was not found to measurably affect lens distortion.

1. INTRODUCTION

At the present moment, the semiconductor industry is wavering on the choice of whether to use DUV or i-line for 0.35μm lithography. If 0.35μm structures can be manufactured with i-line technology, there will be significant cost savings. This will be a competitive advantage especially for parts with a low average selling price, such as memory (1). The penalty for choosing incorrectly will be severe, possibly forcing the unwise to exit the commodity memory business.

Most feel that i-line alone will be provide insufficient process latitude for 0.35μm structures, and therefore must be supplemented with phase shifting masks and/or oblique illumination. At present, there are significant uncertainties regarding the use of either of these techniques. Further complicating the issue, most machines with oblique illumination exist only in the prototype stage, and metrology of 0.35μm structures is difficult and time consuming. Hence accurate data for engineering decisions are sparse.

In order to guide decision making we have extended our 2-dimensional scalar aerial image model to incorporate different illumination configurations (2). The model has been implemented with a numerical scheme at close to the theoretical resolution limit. On an IBM RS/6000 workstation, a 64 X 128 grid can be computed in a few minutes. This paper examines oblique illumination from both experimental and computational vantage points. Section 2 discusses experimental and computational details. Section 3, containing results, is divided into four areas. Area 1 compares 3-dimensional developed images and 2-dimensional aerial images. Area 2 presents critical dimension control information for standard, annular, and quadrupole illumination types; much of the information is presented as contour plots obtained by continually varying the two illumination geometry parameters (e.g. in the case of annular illumination, the inner radius and outer radius); "optimum" illuminator configurations are suggested. Area 3 uses simulation to examine the differences in imaging between KrF with standard illumination and i-line with several types of oblique

illumination; an SRAM cell with .35μm gate length is used as the test structure. Area 4 presents results from a lens distortion test with quadrupole illumination. The results are followed by conclusions in Section 4.

2. EXPERIMENTAL AND COMPUTATIONAL

Conventions for the illuminator geometry are shown in Figure 1. A standard illuminator is represented as circle of radius r1 outside of which the light intensity is zero; the scale of the coordinate system has been chosen so that r1 is identically equal to the partial coherence (sigma) of the imaging system. The annular illuminator is represented as a circle with outer radius r1, and inner radius r2; the light intensity is non-zero only between r1 and r2. The scale of the coordinate system for annular illumination was chosen so as to correspond with the coordinate system for standard illumination, e.g. when the inner radius (r2) is zero, the outer radius (r1) is identically equal to the partial coherence (sigma) of an imaging system with standard illumination. The quadrupole illuminator (see Figure 1) is represented as a circle with radius r1 (referred to as the placement radius) on which are placed smaller circles of radius r3 (referred to as the radius of the individual "pole" of the quadrupole). Again the coordinate system scale was chosen to be consistent with the standard illumination configuration.
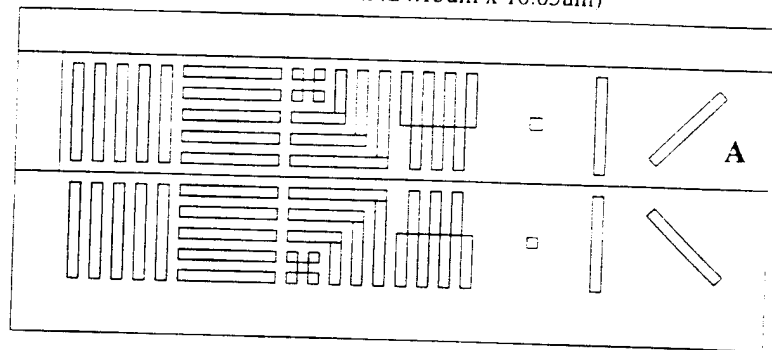
Conventions.
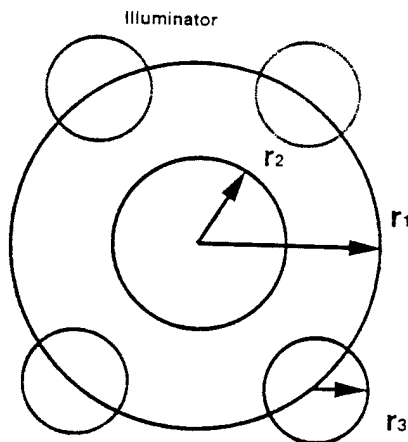
Illuminator

Standard case: r1 = radius of illuminator = sigma

Annular case: r1 = outer radius. r2 = inner radius

Quadrupole case: r1 = placement radius.

r3 = individual quadrupole radius

Figure 1. Conventions for the illuminator geometry.

.35um Test Mask (24.15um x 10.05um)

A

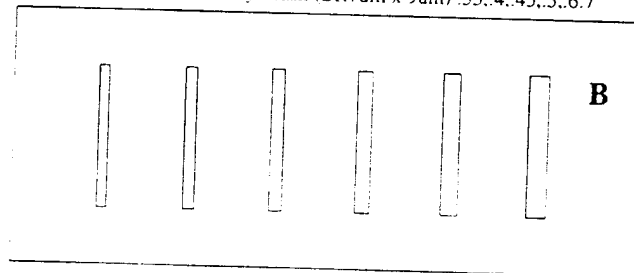Isolated Line Linearity Mask (21.7um x 9um) .35..4..45..5..6.7

B

Figure 2. Masks used for computations: (A) .35μm test mask; and (B) isolated line linearity mask.

Resist images were printed by exposing a 0.79μm thick film of Sumitomo PFI-28 photoresist, and developing for 60 seconds in 0.262 N tetramethylammoniumhydroxide solution.

Two steppers were used, the ASML 5000/50 with NA of .48 and sigma of .62, and the ASML 5500/60 with NA of .54 and sigma of .48.

The fly's eye lens on the 5000/50 has 96 elements transmitting in the standard illumination configuration with a sigma of .62. Before running experiments, an intensity of 305mw/cm2 was measured at the wafer plane. The illumination homogeneity was 2.1%. Experiments were also run on the 5000/50 with a quadrupole illumination filter obscuring all but 27 elements of the fly's eye lens. The four individual quadrupoles of this filter had a radius of .18 and were distributed on a radius of .5. An intensity of 107mw/cm2 was measured at the wafer plane when this "filter" was installed. The illumination homogeneity

was 2.2% without adjustment.

A Silicon Graphics Personal Iris 4D35 workstation was used for computations. Software based on a fast algorithm for computation of scalar 2-dimensional aerial images was used. This platform and software combination took about 2.5 minutes to compute the 2-dimensional aerial image for a 24.1μm x 10.5μm mask with 65 features at NA .48 and sigma .62 . The actual layout of the mask used for this computation is shown in Figure 2A. The mask consists of various .35μm structures in a symmetrical bright field and dark field layout. This mask is referred to as the ".35μm test mask". Figure 2B show an additional mask consisting of chrome islands at a 3μm pitch. The islands range in width from .35μm to .7μm. This mask is referred to as the "isolated line linearity mask", or "linearity mask".

3. RESULTS

3.1 Comparisons between developed images and 2-dimensional aerial images

Figure 3 compares developed photoresist images of .35um features and computed 2-dimensional aerial images for consecutive values of focus, starting at 0. The exposures were done with an ASML 5000/50 i-line stepper, with NA .48 and quadrupole illumination. Corresponding parameters were used in the simulations. A portion of the mask used for actual photoresist exposure closely approximated the ".35μm test mask". Although the simulations were run using the entire 24.1μm x 10.5μm .35μm test mask, only a portion of the simulation is shown for clarity (this is the bright field portion in the lower left hand corner of Figure 2A). All resist images have the same exposure, with approximately equal line/space condition at best focus. All aerial image simulations have the same normalized intensity contour (.36); this intensity contour provides approximately equal line/space condition for the aerial image at 0 focus. The scalar aerial image is symmetric about 0 focus; the developed photoresist images are not, and only those photos representing moving the lens away from the wafer are shown. Note that the developed photoresist images are centered around "best" focus; at "best" focus, the 0 focus aerial image is somewhat below the surface of the photoresist. Consequently, for best focus scale calibration, the developed images should be shifted in the positive direction, between .1μm and .2μm.

At .3μm defocus, there is close correspondence between the developed image and the simulated aerial image (see Figure 3). The proximity effects occurring in the developed image are reproduced closely in the aerial image; these include effects such as (1) the narrowing of ends of the vertical lines, (2) the narrowing of the ends of horizontal lines on the side near the vertical line, (3) the wavy nature of the vertical line nearest the set of horizontal lines, and (4) narrowing and thickening of the nested elbows. Also, the bottom line of the horizontal line group closely matches its neighbors in size.

At .6μm defocus (see Figure 3), the major differences between the developed and the computed image are the bottom line of the horizontal line group and the array of 5 posts. In the developed image, the bottom horizontal line is substantially smaller than the lines above, while in the aerial image, this line still approximates closely in size the other 4 lines of the group. The array of 5 posts show substantial degradation, especially to lower left post, while in the aerial image, the pattern still has good acuity and good four fold symmetry.

The differences observed can be explained by the finite thickness of the photoresist. The aerial image at .6μm defocus is, in reality, the intensity distribution near the top surface of the corresponding photoresist image. Because the photoresist is partially transparent, however, the plane of photoresist at, say .3μm optical depth below the top surface (of the .6μm defocused resist image), sees an intensity distribution that is closer to the aerial image at .9μm defocus. Moreover, since the photoresist has an optical thickness of about 1.32μm, aerial images from as much as 1.92μm (.6μm + 1.32μm) defocus contribute to the exposed image in the photoresist (the exact contribution is difficult to determine since it is a function of the "transparency", which is a dynamic function of exposure). Since the 5 posts and the bottom horizontal line are the most rapidly changing features of the aerial image, it is unsurprising that at .6μm defocus, developed image of these features show poor agreement with the .6μm defocus, aerial image of these same features.
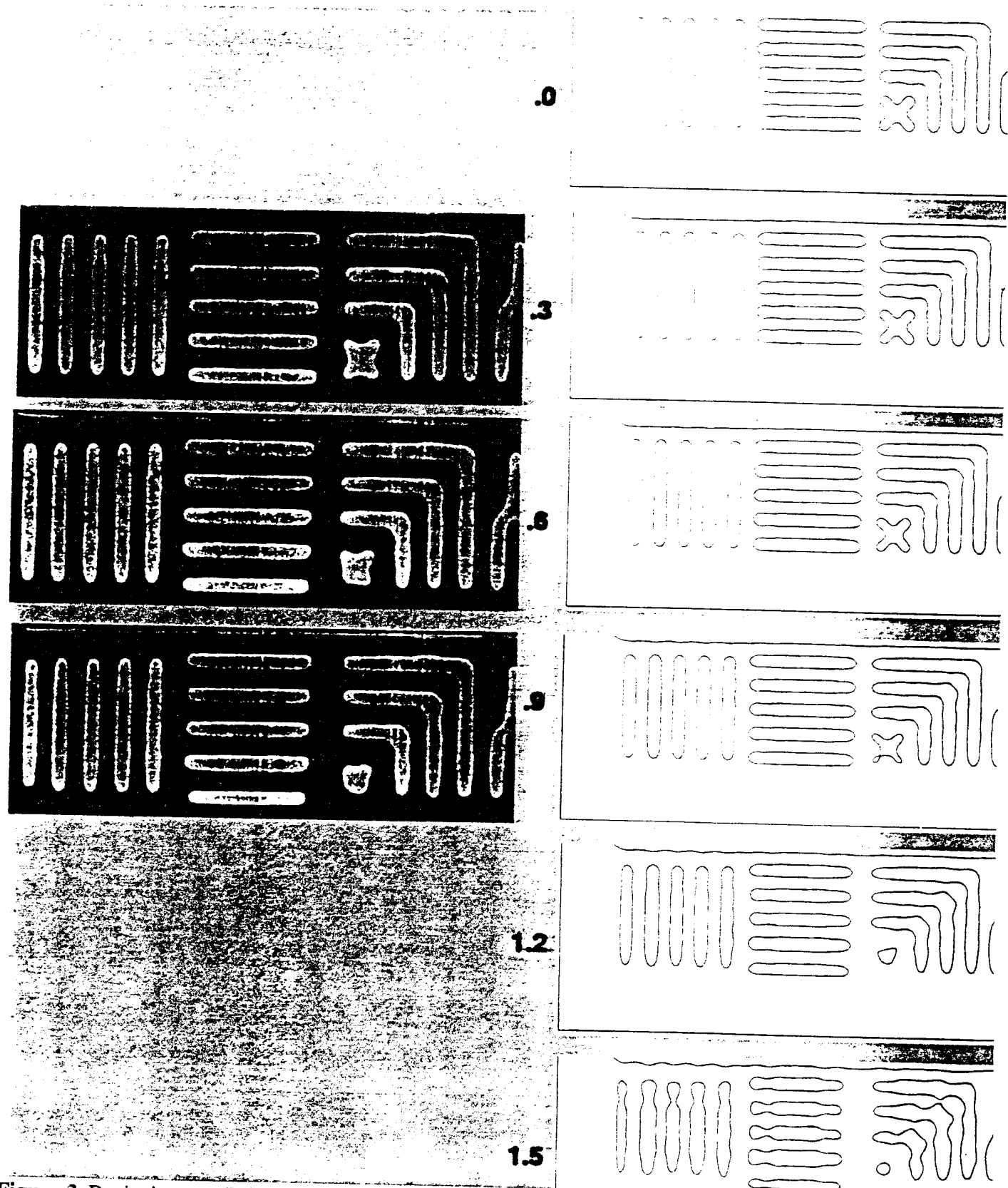
Figure 3. Resist images (left column) and corresponding aerial images (right column) at different defocus. I-line stepper with NA .48 and quadrupole illumination (.5 X.18), with focus as indicated.

Two primary conclusions can be made. First, the computed aerial image agrees with developed image near best focus. Second away from best focus, due to finite resist thickness and substantial changes in the aerial image with defocus, the developed image shows poor agreement with aerial image computed at the top surface of the developed image. Generally, by looking only at the aerial image at the top surface of the photoresist, one would over estimate the depth of focus (DOF) available.

3.2 Optimization of oblique illumination for critical dimension control

A matrix of simulations was done to characterize oblique illumination and determine which illumination parameters would provide the greatest DOF. 1.8μm (±.9μm) focus variation with less than 10% linewidth change was considered a reasonable requirement for aerial image DOF. Consequently, in the first set of simulations the linewidth and exposure latitude for a series of isolated features were calculated at 0 focus and .9μm focus. First, for specified NA and illumination parameters, the aerial image was calculated at 0 focus; the normalized intensity value to make the .35μm isolated line "print" at .35μm was determined and stored; using this intensity value, the linewidths printed by all the other features on the mask were determined; the exposure latitudes of all features were determined by measuring the percentage of intensity variation that would make the "printed" linewidth change by .035μm. Second, the aerial image was calculated at .9μm focus; using the stored value of normalized intensity, the linewidths printed by all features on the mask were determined at this focus; the exposure latitudes of all features at .9μm defocus were determined just as in the 0 focus case.

This sequence of simulations was run for a fixed NA of .48 and a matrix of about 180 different annular illumination geometries; starting at 0 (actually .005), the outer radius (see Figure 1) was stepped by .05 sigma units to a final sigma of .8; at each value of outer radius, the inner radius was stepped by .05 sigma units from 0 until the inner radius was equal to the outer radius (actually, .005 sigma units less than the outer radius). Figure 4A displays, in contour format, the linewidth results for a .35μm isolated line at .9μm defocus. For convenience, the axes of Figure 4A have been modified to make the plot symmetric. This is because for annular illumination, the inner radius must be less than the outer radius; this restricts all physically meaningful values to the space below the line where the inner radius equals the outer radius (when the y axis is the inner radius and the x axis is the outer radius). Figure 4A has been made symmetric by reflecting the data below the line "y equals x" about the line "y equals x" to give the data above the line "y equals x". The axes have been labelled in "sigma" units. When reading a point on the graph, for example, that corresponds to a particular value of sigma along the x-axis (sigma-x) and another value of sigma along the y-axis (sigma-y), the only physically meaningful illuminator configuration that this could correspond to is for the larger value of sigma to represent r1 (the outer radius) and the smaller value of sigma to represent r2 (the inner radius). Figure 4A shows several important trends. First, for standard illumination, increasing sigma always improves the CD control at .9μm defocus, until a plateau is reached at sigma about .65. Second, Figure 4A also indicates starting with a fixed value of the outer radius and increasing the inner radius from zero results in a significant improvement in CD control at .9μm defocus. Figure 4A also indicates that only illumination geometries with outer radius between approximately .6 and .8 and inner radius greater than about .55 will maintain the .35μm isolated CD above .3μm at .9μm defocus. This area corresponds to the area inside the .3μm contour. Figure 4A also indicates the best CD control performance that can be expected is for a .35μm line to change from .35μm at 0 defocus to .30μm at .9μm defocus; this exceeds a typical 10% CD control tolerance, which would limit the CD of the .35μm isolated line to be no less than .315μm.

A similar sequence of simulation was run for a quadrupole geometry for fixed NA of .48; starting at .1, the placement radius of the quadrupoles (r1 of Figure 1) was stepped by .05 sigma units to a final sigma of .8; at each value of the placement radius, the radius of the individual quadrupoles (r3 of Figure 1) was stepped by .05 sigma units from 0 (actually .005) until the next .05 increment would exceed .707 times the current value of the placement radius (when the individual quadrupole radii exceed .707 times the placement radius, the quadrupoles start to overlap). Figure 4B displays, in contour format, the linewidth results for a .35μm isolated line at .9μm defocus. Again, for convenience, the axes of Figure 4B have been modified to make the plot symmetric. Again, several important generalizations can be made. First, until a placement radius (r1) of
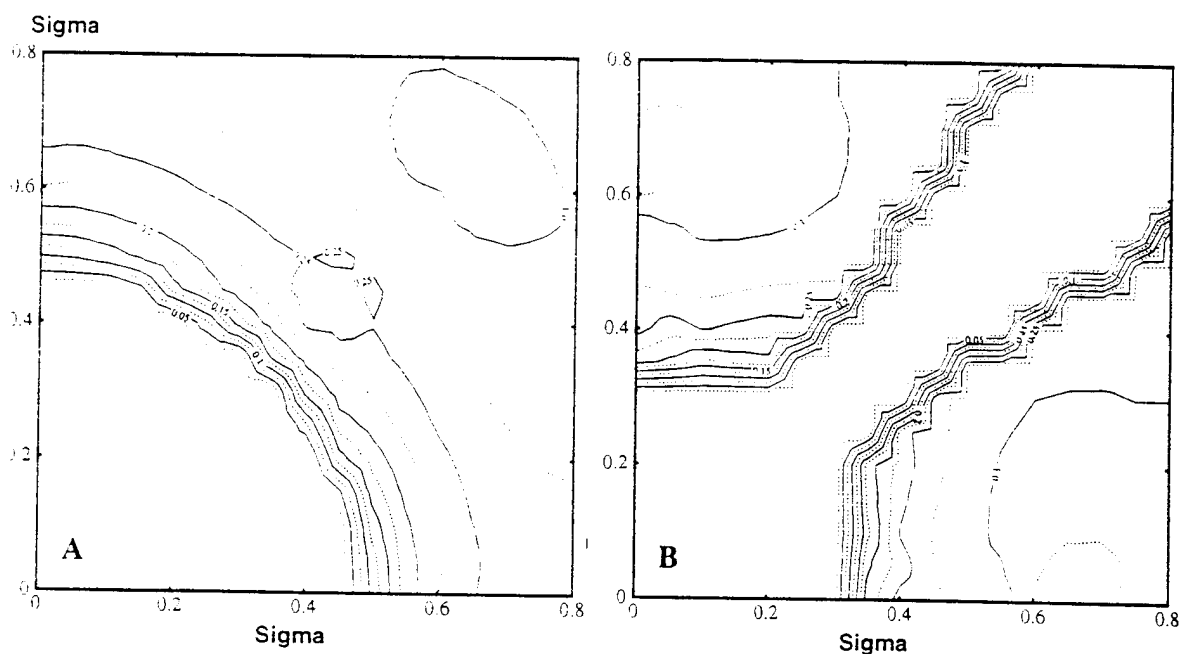
Figure 4. Simulations of .35μm isolated line CD control at 0.9μm defocus for i-line systems with fixed NA of .48 and various illuminator configurations: (A) annular illumination; and (B) quadrupole illumination.

.6 is reached, the CD control performance at .9μm defocus of the quadrupole illuminator is largely independent of the individual quadrupole radius (r3). Consequently, the individual radii can be maximized to increase the light output of the illuminator. Above a placement radius (r1) of .6, there appears to be a CD control penalty for increasing the individual radii. With a placement radius of .7 and an individual quadrupole radius of .1, a .35μm line can be maintained to .325μm; this is within a 10% CD control tolerance. In this regard, quadrupole illumination appears to be superior to annular illumination.

As would be expected, both annular and quadrupole illumination achieve the best CD control when the illumination is directed from similar angles. This can be seen by comparing Figures 4A and 4B, which show that the areas of best CD control for each case occur in similar areas of sigma space. In fact, a quadrupole illuminator could be thought of as an annular illuminator with 4 segments of the annulus blocked.

There are penalties associated with oblique illumination. One of these, namely exposure latitude at best focus, is quantified in Figure 5. Figure 5 compares the exposure latitude for a .35μm isolated line at best focus under various configurations of annular illumination, as explained for Figure 4A. Figure 5A presents the data for NA .48 and Figure 5B, for NA .54. The exposure latitude is defined in terms of % exposure change needed to cause a .35μm line to increase in CD by .035μm, or 10%. Since typical CD control requirements are ±10%, it should be kept in mind that the exposure latitude numbers should be multiplied by a factor of 2 to give the process window. Also, it should be remembered that these measurements are taken only in the aerial image; since real resists do not have infinite contrast, the exposure latitude measured in a real resist would be expected to be less than the numbers reported in Figure 5. Several basic observations can be made. For virtually all configurations, increasing the outer radius (r1) decreases the exposure latitude at 0 focus. This is also true for the case of standard illumination (r2 equals 0). For example, the exposure latitude decreases from about 20% to about 17% as sigma increases from .50 to .65 for NA .48. For a fixed value of the outer radius (r1), as the inner radius increases starting form 0, there is a concomitant loss in exposure latitude. However, since the contours are fairly perpendicular to the x and y axes, the loss in exposure latitude at best focus is not a severe penalty. Similar plots of exposure latitude are shown in Figure 6 for the same isolated line, but at .9μm defocus. Figure 6A presents the data for annular illumination with NA .48, while Figure 6B presents the data for quadrupole illumination with NA .48. For annular illumination at .9μm defocus, exactly the opposite behavior is observed from 0 focus: increasing sigma now increases exposure

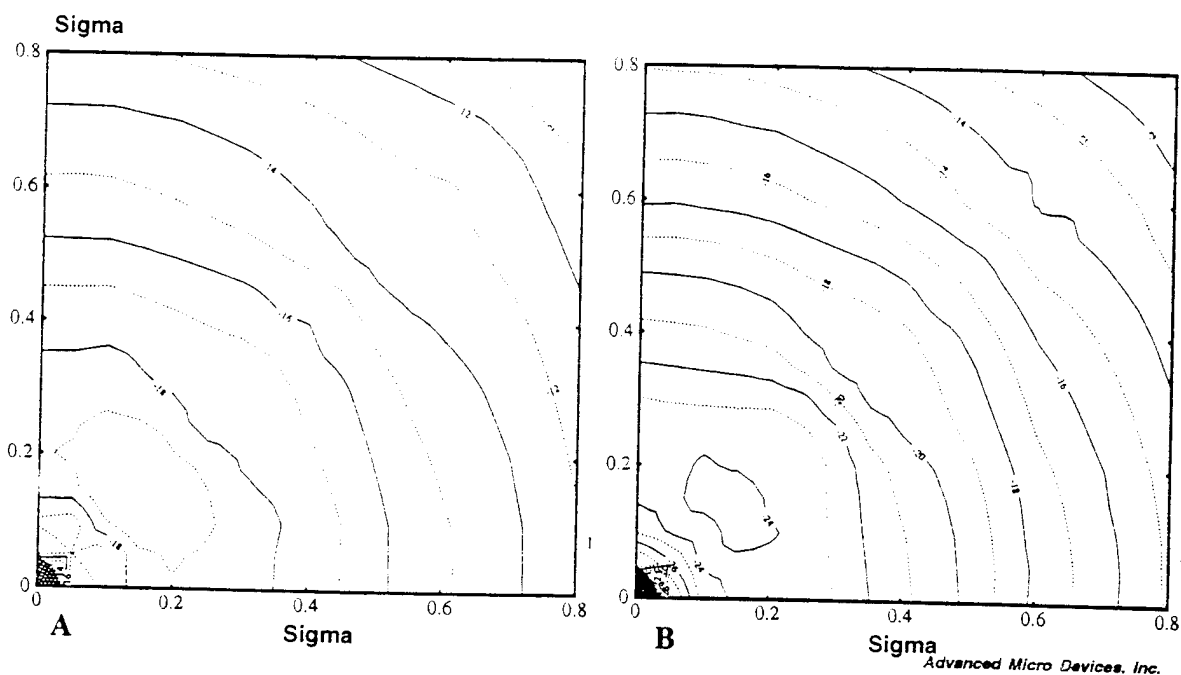**Figure 5.** Simulations of .35μm isolated line exposure latitude at best focus for i-line systems with various annular illumination configurations: (A) NA of .48; and (B) NA of .54.
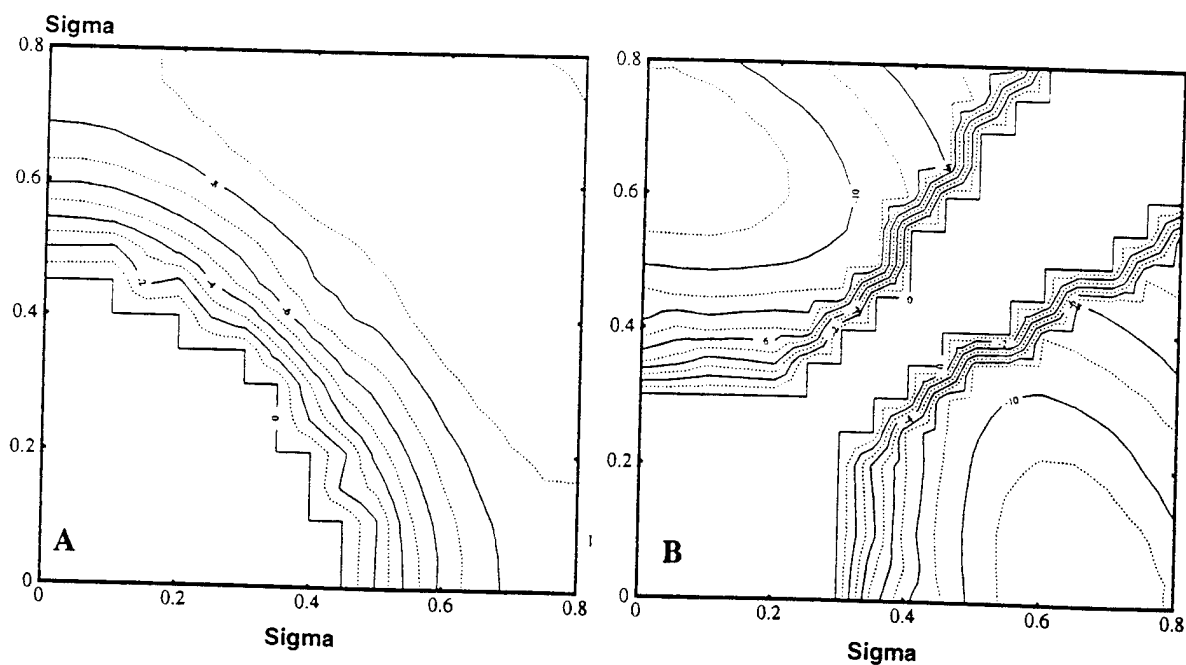

Figure 6. Simulations of .35μm isolated line exposure latitude at .9μm defocus for i-line systems with fixed NA of .48 and various illuminator configurations: (A) annular illumination; and (B) quadrupole illumination.

latitude, although a plateau appears to occur in about the same area as the best CD control occurs (see Figure 6A and Figure 4A).

Table 1 summarizes exposure latitude and CD control numbers at .9μm defocus for several specific illumination configurations and 2 difference numerical apertures. Included are numbers for three different isolated linewidths, i.e. .35μm, .5μm and .7μm. Several configurations in Table 1 can achieve CD control to better that 10% at .9μm defocus, i.e. the printed linewidth will be between .315μm and .35μm. For NA .48, these are the quadrupoles with r1 equal to .65 and r3 equal to .05, and r1 equal to .65 and r3 equal to .10. For NA .54, the quadrupole with r1 equal to .70 and r3 equal to .05. The lower NA (.48) was able to achieve better CD control than the higher (.54), although at a somewhat reduced exposure latitude. None of the annular configurations would achieve 10% CD control for .35μm isolated line.

Wvlen	NA	k1	Sigma	.35um @ .9um Def CD	ExL	.5um @ .9um Def ΔCD	ExI	CD@.0,.9	.7um @ .9um Def ΔCDexI		CD@.0..9
i-line	.48	.46	.62	.236	6.9	.057	11.0	.502-.445	.054	12.0	.702-.648
			.70 x .60	.305	10.5	.062	9.5	.531-.469	.057	9.4	.775-.718
			.65 x .05	.325	11.6	.020	10.4	.486-.466	.086	7.9	.810-.724
			.65 x .10	.323	11.7	.042	10.1	.499-.457	.100	9.0	.802-.702
	.54	.51	.50	.000	.0						
			.70 x .05	.316	12.2	.068	9.7	.518-.450	.091	7.9	.820-.729
			.70 x .10	.305	12.3	.094	10.2	.532-.438	.109	8.0	.816-.707

CD measurements in um.
ExI = % intensity change for .035um shift in CD.

Table 1. Summary of CD control and exposure latitude for various isolated line features with specific illuminator configurations.

3.3 Comparisons between i-line with oblique and KrF with standard illumination

The oblique illumination configurations of Table 1 were next computationally tested for performance on a .35μm minimum feature SRAM gate cell mask. This was done to study how well the isolated line performance would translate into a real circuit situation where some neighboring features were present that would induce proximity effects. In to order more properly duplicate the proximity effects seen in memory cores, the mask used for the simulation consisted of an array of 3 SRAM gate cells (see Figure 7). Each cell has an area of 15.5μm X 4.9μm. A border was added to the array of 3 cells to give a total mask size of 16.9μm X 16.1μm (see Figure 7). Measurements from the simulations were only taken on features in the center cell of the array.

Wvlen	NA	k1	Sigma	Test Mask .35um @ .9um Def CD	ExL	SRAM Gate Cell Mask .35um @ .0um Def CD	ExI	Trhld	.35um @ .9um Def CD	ExI
i-line	.48	.46	.62	.236	6.9					
			.70 x .60	.305	10.5	.35	12.1	34%	.280	10.2
			.65 x .05	.325	11.6	.35	13.4	33%	.297	12.1
			.65 x .10	.323	11.7					
	.54	.51	.50	.000	.0					
			.70 x .05	.316	12.2	.35	13.1	38%	.280	13.1
			.70 x .10	.305	12.3					
KrF	.42	.59	.60			.35	21.7	22%	.280	10.8
	.37	.51	.60			.35	18.6	24%	.300	12.0

CD measurements in um.
ExI = % intensity change for .035um shift in CD.

Table 2. Summary of CD control and exposure latitude for .35μm minimum feature SRAM gate mask cell with specific illuminator configurations and exposure wavelengths.

Table 2 summarizes the simulated CD control of the i-line systems with various illuminations configurations. For comparison, simulations were also done for several KrF imaging systems with standard illumination (see Table 2). The NA and sigma of the KrF systems was chosen to represent a common system available (NA .42 and sigma .60), or to provide a similar k1 factor to the NA .54 i-line system (NA .37 and sigma .60).
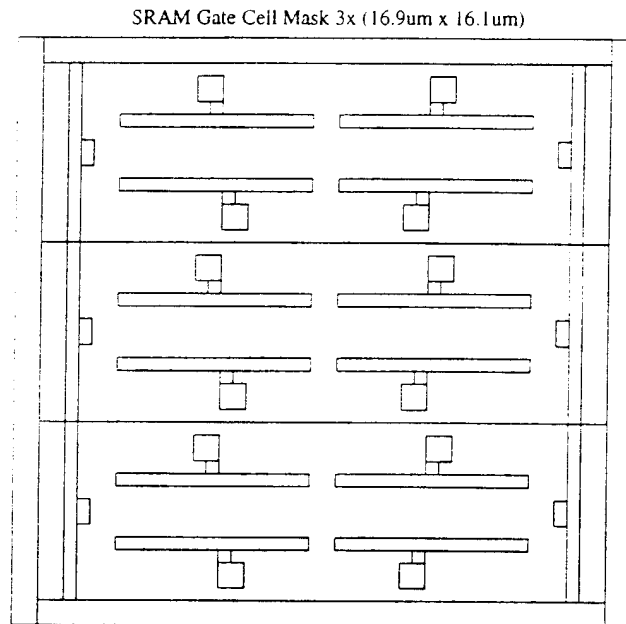
SRAM Gate Cell Mask 3x (16.9um x 16.1um)

Figure 7. SRAM gate cell array mask (16.9μm X 16.1μm) used for simulations.

Several important points are indicated in Table 2. With NA .48, at .9μm defocus, the CD control on the .35μm gate of the SRAM cell is about 8% worse than observed for a more nearly .35μm isolated line (.35μm line on a 3μm pitch) of the previous calculation (see Table 1). The performance of the NA .54 system is 11.5% worse on the SRAM gate than on the more nearly isolated line (compare Tables 1 and 2). The computed aerial images readily show that performance discrepancies result from proximity effects (see Figure 8). Figure 8A, and B show, respectively a portion of the computed aerial image at .9μm defocus of the NA .48 system with annular illumination (.7 X .6) and NA .54 with quadrupole illumination (.7 X .05); the appropriate threshold contour on which the CD measurement is based is indicated by the narrow dark line (recall that the specific threshold was determined by requiring the aerial image linewidth of the gate to be .35μm at 0 focus). In Figure 8A, both the contact pad and the finite length of the line induce proximity effects near the gate region of the invertor transistors; especially apparent is the tapering of the gates towards their ends. More severe proximity effects are exhibited by the NA .54 quadrupole (.7 X .05) system (see Figure 8B); now there is substantial "ringing in the aerial image that extends over several minimum feature lengths. The corresponding computed aerial image for an NA .37 KrF system with standard illumination (sigma .6) is shown in Figure 8C; proximity effects are much less apparent with this system. Thus, although from a numerical point of view linewidth control through focus of the KrF imaging systems is about the same as the i-line systems with oblique illumination (see Table 2), that is only half the story; the KrF systems are free of the large proximity induced variation that is present in the various obliquely illuminated i-line systems.

Table 2 also compares the exposure latitude performance of the i-line systems with oblique illumination and the KrF systems with standard illumination. Although the exposure latitude of the i-line systems with oblique illumination is similar to the KrF systems at .9μm defocus, at best focus the KrF systems have more that 50% better exposure latitude.
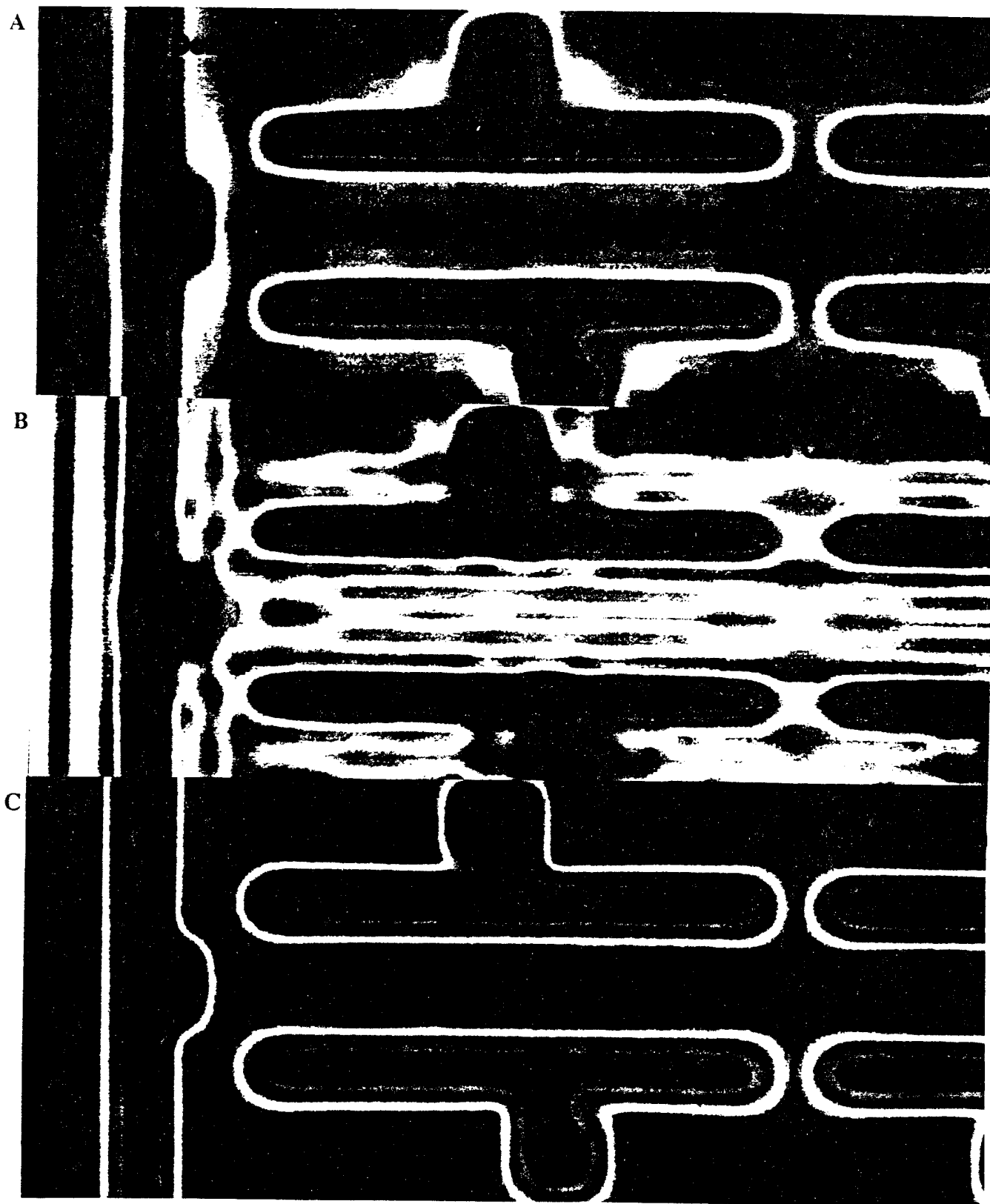
Figure 8. Greyscale image of a portion of the aerial image simulations of SRAM gate cell mask: (A) NA .48 i-line with annular illumination (.7 X .6); (B) NA .54 i-line with quadrupole illumination (.7 X .05); and (C) NA .37 KrF with standard illumination (sigma .60).

3.4 Impact of oblique illumination on field distortion

A change in field distortion may occur if oblique illumination significantly emphasizes or de-emphasizes lens distortion. A large change in field distortion would show up as a change in overlay performance as measured on the same machine (with oblique illumination installed) to itself (with standard illumination). No significant change in overlay performance was observed when this measurement was carried out.

4. CONCLUSIONS

Developed resist patterns and 2-dimensional aerial images compared favorably near best focus. The long and short range proximity effects visible in the photoresist exposed with the quadrupole illuminator were reproduced well in the computed 2-dimensional aerial image, giving confidence in the accuracy. However, because of the finite thickness of the photoresist and the rapid change of the aerial image with defocus, the developed image is poorly represented by one slice of the aerial image at defocus.

The effects on CD control, exposure latitude, and bias, of varying annular and quadrupole geometry were mapped via simulation. Significant improvements in DOF of isolated lines was achieved with oblique illumination. Isolated line to dense line bias could be adjusted by changing the illumination type. Although oblique illumination improved the aerial image contrast at defocus, it caused degradation in the aerial image contrast at best focus.

Long and short range proximity effects degraded the simulated CD control of optimized oblique illumination systems. This was observed in simulations of an SRAM gate cell. The imaging performance at .9um defocus, of an i-line system (NA .48) with oblique illumination, was judged to be worse than a KrF system (NA .42) with standard illumination.

Quadrupole illumination was not found to measurably affect lens distortion.

5. ACKNOWLEDGEMENTS

6. REFERENCES

1. B. Arnold, Lithography Rump Session, VLSI Technology Symposium, 1992.

2. D. Cole, E. Barouch, U. Hollerbach, S. A. Orszag, "Derivation of Higher Numerical Aperture Scalar Aerial Images", Japanese J. Appl. Phys. (to appear).